Unterschrift Betreuer

TECHNISCHE
UNIVERSITÄT
WIEN
Vienna | Austria

DISSERTATION

Influence of ion sputtering on the surfaces of Mercury and the Moon

ausgeführt am Institut für Angewandte Physik
der Technischen Universität Wien

unter der Anleitung von
Univ.-Prof. Dr. Friedrich Aumayr

durch

Dipl.-Ing. Herbert Alexander Biber
[redacted]

[redacted]

February 14, 2023

Unterschrift Student

Contents

Abstract

The space between planets and bodies in our solar system is almost empty – but nevertheless a very harsh environment. A wide range of effects continuously impacts on the surfaces of rocky celestial bodies, leading to modifications and liberation of material. Due to the emission of energetic particles from the sun – the solar wind – surfaces are constantly eroded by ion sputtering. The sputtered material leads to the formation of a tenuous layer around planets and moons with increased density, the exosphere. It is therefore crucial to understand the interaction of solar wind ions with the surfaces of rocky bodies in order to be able to comprehend the exosphere formation. This also includes constraining the effects of often hidden properties, like crystal structure and surface roughness on the sputtering process for minerals, as typically flat, amorphous samples are discussed with regard to their sputter yield. Experiments with different ion species and sample materials were carried out, investigating the interaction of the solar wind ions with rocky body surfaces in detail.

Therefore the magnesium and iron rich pyroxene augite $((\mathrm{Ca,Mg,Fe})_2[\mathrm{Si_2O_6}])$ was irradiated with $\mathrm{He^+}$ ions at a kinetic energy of 4 keV and $\mathrm{H_2}^+$ ions at 2 keV in the form of thin films. Thereby, the sputter yields in dependence of the incidence angle could be measured for both projectiles. Furthermore, the implantation of He upon impact was studied extensively. Different regimes with respect to the net implantation flux could be seen as well as a concentration of 10 at.% of implanted He in the saturated sample. Subsequent thermal desorption spectroscopy measurements in combination with a microbalance technique have shown, that all implanted He is removed from the samples when heating them to 530 K. This is in the range of Mercury's temperature variations, which can reach from 100 K up to 700 K.

By means of a novel experimental setup including two microbalances, also a comparison of the sputtering of amorphous and crystalline phases for planetary analogs was possible – additionally allowing to probe the angular distributions of the sputtered material. For this purpose, wollastonite $(\mathrm{CaSiO_3})$ and enstatite $(\mathrm{MgSiO_3})$ samples were prepared as amorphous thin films and as poly-crystalline pressed mineral pellets. Measurements were performed with 4 keV $\mathrm{He^+}$ and 2 keV $\mathrm{Ar^+}$ ions, impinging under varying angles of incidence. In the case of the wollastonite samples, almost identical sputter yields for the two types of samples were obtained, whereas significantly smaller yields were measured for the enstatite pellet compared to the respective thin films. Accompanying simulations of sputtering of rough surfaces using atomic force microscope images of the pellet surfaces as inputs agree well with this experimentally observed behavior. It is therefore concluded, that no effects of crystal structure are present in the investigated fluence regime.

This also implies that data obtained with amorphous samples can be used for the estimation of sputtering on celestial bodies. Furthermore, the necessity of taking surface roughness into account when calculating sputtering on realistic planetary surfaces has been shown.

Expanding on the results with analog materials, real lunar samples returned to Earth by the NASA Apollo 16 mission have been investigated regarding the according sputter yields upon ion irradiation. Molecular hydrogen (${H_2}^+$) at a kinetic energy of 2 keV as well as 4 keV He^+ ions were used for the experiments. Again, pressed mineral pellets with poly-crystalline structure and certain surface roughness were compared to flat amorphous thin films. Also in this less idealized scenario, simulations are able to reproduce experimental results under the assumption, that surface roughness is the only relevant difference for sputtering. This means, that it might be sufficient to consider actual surface topology (roughness) and surface composition for an accurate description of the sputtering behavior of rocky celestial bodies.

Kurzfassung

Unser Sonnensystem ist trotz seiner Leere eine raue Umgebung. Auf die Oberflächen gesteinsförmiger Himmelskörper wirkt ständig eine Vielzahl von Einflüssen ein und führt zum einen zu einer Veränderung dieser und zum anderen zum Freisetzen von Material. Dies ist darauf zurückzuführen, dass Planetenoberflächen kontinuierlich durch von der Sonne emittierte, energetische Teilchen – dem Sonnenwind – getroffen und aufgrund der verursachte Ionenzerstäubung abgetragen werden. In weiterer Folge führt dieses zerstäubte Material zur Bildung einer dünnen Schicht erhöhter Dichte um Planeten und Monde, der Exosphäre. Um die Bildung der Exosphäre nachvollziehen zu können, ist es daher von entscheidender Bedeutung, die Wechselwirkung der Ionen des Sonnenwindes mit den Oberflächen von gesteinsförmigen Himmelskörpern zu verstehen. Dazu gehört auch, die Auswirkungen von oft nicht berücksichtigten Eigenschaften wie Kristallstruktur und Oberflächenrauigkeit auf den Zerstäubungsprozess bei Mineralien einzugrenzen, da typischerweise flache, amorphe Proben im Hinblick auf ihre Zerstäubungsausbeute diskutiert werden. Hierzu wurden Experimente mit verschiedenen Ionenspezies und Probenmaterialien durchgeführt, wodurch die Wechselwirkung der Sonnenwind-Ionen mit Planetenoberflächen im Detail untersucht werden konnte.

Das magnesium- und eisenreiche Pyroxen Augit ($(\mathrm{(Ca,Mg,Fe)_2[Si_2O_6]})$) wurde in Form dünner Schichten mit 4 keV He^+ und mit 2 keV H_2^+ Ionen bestrahlt und die Zerstäubungsausbeuten in Abhängigkeit vom Einfallswinkel für beide Projektile gemessen. Darüber hinaus wurde auch die Implantation von He während den Bestrahlungsphasen eingehend untersucht. Es konnten zum einen verschiedene Regime in Bezug auf die netto Implantation sowie zum anderen eine lokale Konzentration von 10 at.% an implantiertem He in der gesättigten Probe festgestellt werden. Anschließende Thermodesorptionsspektroskopie haben in Kombination mit einer Mikrowaagen-Technik gezeigt, dass ein erhitzen der Proben auf 530 K dazu führt, dass das gesamte implantierte He wieder aus den Proben entfernt wird. Dies liegt im Bereich der Temperaturschwankungen auf der Oberfläche des Planeten Merkur, die von 100 K bis zu 700 K reichen können.

Mit Hilfe eines neuartigen Versuchsaufbaus mit zwei Mikrowaagen war auch ein Vergleich des Zerstäubens von amorphen und kristallinen Phasen für planetare Analogmaterialien möglich – wobei zusätzlich auch die Winkelverteilungen des emittierten Materials untersucht werden konnte. Zu diesem Zweck wurden Proben aus Wollastonit ($CaSiO_3$) und Enstatit ($MgSiO_3$) als amorphe, dünne Filme und als polykristalline, gepresste Mineralpellets hergestellt und Bestrahlungen mit 4 keV He^+ und 2 keV Ar^+ Ionen unter verschiedenen Einfallswinkeln durchgeführt. Im Falle der Wollastonit-Proben wurden nahezu identische Zerstäubungsausbeuten für die beiden Probentypen gefunden, während sich bei dem Enstatit-Pellet eine deutlich geringere Ausbeuten im Vergleich zu den entsprechenden Dünnschichten zeigten. Begleitende Simulationen zur Zerstäubung von rauen Oberflächen unter Verwendung von Aufnahmen der Pelletoberflächen – erstellt mittels Rasterkraftmikroskopie – stimmen gut mit diesem experimentell beobachteten Verhalten überein. Daraus kann gefolgert werden, dass es im untersuchten Fluenzbereich keine Auswirkungen der Kristallstruktur auf den Zerstäubungsprozess gibt. Dies bedeutet auch, dass die mit amorphen Proben gewonnenen Daten für die Abschätzung des Zerstäubens für Himmelskörper angewendet werden können, für die Berechnung jedoch die Oberflächenrauigkeit berücksichtigt werden muss.

Erweiternd zu den Ergebnissen mit Analogmaterialien wurden auch reale Mondproben – aus dem Bestand des von der Apollo 16 Mission der NASA zur Erde gebrachten Materials – hinsichtlich der entsprechenden Zerstäubungsausbeute bei Ionenbestrahlung untersucht. Für die Experimente wurden sowohl molekularer Wasserstoff (H_2^+) mit einer kinetischen Energie von 2 keV als auch 4 keV He^+ Ionen verwendet, um das Zerstäuben von gepresste Mineralpellets mit polykristalliner Struktur und einer gewissen Oberflächenrauigkeit mit dem von flachen, amorphen Dünnschichten zu verglichen. Auch in diesem weniger idealisierten Szenario sind die Simulationen – unter der Annahme, dass die Oberflächenrauigkeit der einzige relevante Unterschied für den Zerstäubungsprozess ist – in der Lage, die experimentellen Ergebnisse zu reproduzieren. Dies bedeutet, dass die Berücksichtigung der tatsächlichen Oberflächentopologie (Rauheit) und der Oberflächenzusammensetzung für eine genaue Beschreibung der Zerstäubung von gesteinsförmigen Himmelskörpern ausreichen könnte.

Publications as First Author

H. Biber, J. Brötzner, N. Jäggi, P.S. Szabo, J. Pichler, C. Cupak, C. Voith, B. Cserveny, A. Mutzke, M.V. Moro, D. Primetzhofer, K. Mezger, A. Galli, P. Wurz and F. Aumayr
Sputtering Behavior of Rough, Polycrystalline Mercury Analogs
The Planetary Science Journal **3** (2022) 271
`https://dx.doi.org/10.3847/PSJ/aca402`

H. Biber, P.S. Szabo, N. Jäggi, M. Wallner, R. Stadlmayr, M.V. Moro, A. Nenning, A. Mutzke, K. Mezger, H. Lammer, D. Primetzhofer, J. Fleig, A. Galli, P. Wurz and F. Aumayr
Solar wind Helium ion interaction with Mg and Fe rich pyroxene as Mercury surface analogue
Nuclear Instruments and Methods in Physics Research Section B: Beam Interactions with Materials and Atoms **480** (2020) 10
`https://doi.org/10.1016/j.nimb.2020.07.021`

Publications as Co-Author:

P.S. Szabo, C. Cupak, **H. Biber**, N. Jäggi, A. Galli, P. Wurz and F. Aumayr
Analytical model for the sputtering of rough surfaces
Surfaces and Interfaces **30** (2022) 101924
`https://doi.org/10.1016/j.surfin.2022.101924`

P.S. Szabo, D. Weichselbaum, **H. Biber**, C. Cupak, A. Mutzke, R.A. Wilhelm and F. Aumayr
Graphical user interface for SDTrimSP to simulate sputtering, ion implantation and the dynamic effects of ion irradiation
Nuclear Instruments and Methods in Physics Research Section B: Beam Interactions with Materials and Atoms **522** (2022) 47
`https://doi.org/10.1016/j.nimb.2022.04.008`

P.S. Szabo, A.R. Poppe, **H. Biber**, A. Mutzke, J. Pichler, N. Jäggi, A. Galli, P. Wurz and F. Aumayr
Deducing lunar regolith porosity from energetic neutral atom emission
Geophysical Research Letters **49** (2022) e2022GL101232
`https://doi.org/10.1029/2022GL101232`

C. Cupak, P.S. Szabo, **H. Biber**, R. Stadlmayr, C. Grave, M. Fellinger, J. Brötzner, R.A. Wilhelm, W. Möller, A. Mutzke A., M.V. Moro and F. Aumayr
Sputter yields of rough surfaces: Importance of the mean surface inclination angle from nano- to microscopic rough regimes
Applied Surface Science **570** (2021) 151204
`https://doi.org/10.1016/j.apsusc.2021.151204`

N. Jäggi, A. Galli, P. Wurz, **H. Biber**, P.S. Szabo, J. Brötzner, F. Aumayr, P.M.E. Tollan and K. Mezger
Creation of Lunar and Hermean analogue mineral powder samples for solar wind irradiation experiments and mid-infrared spectra analysis
Icarus **365** (2021) 114492
`https://doi.org/10.1016/j.icarus.2021.114492`

P.S. Szabo, **H. Biber**, N. Jäggi, M. Brenner, D. Weichselbaum, A. Niggas, R. Stadlmayr, D. Primetzhofer, A. Nenning, A. Mutzke, M. Sauer, J. Fleig, A. Foelske-Schmitz, K. Mezger, H. Lammer, A. Galli, P. Wurz and F. Aumayr
Dynamic Potential Sputtering of Lunar Analog Material by Solar Wind Ions
The Astrophysical Journal **891** (2020) 100.
`https://doi.org/10.3847/1538-4357/ab7008`

P.S. Szabo, **H. Biber**, N. Jäggi, M. Wappl, R. Stadlmayr, D. Primetzhofer, A. Nenning, A. Mutzke, J. Fleig, K. Mezger, H. Lammer, A. Galli, P. Wurz and F. Aumayr
Experimental Insights into Space Weathering of Phobos: Laboratory Investigation of Sputtering by Atomic and Molecular Planetary Ions
Journal of Geophysical Research: Planets **125** (2020) e2020JE006583.
`https://doi.org/10.1029/2020JE006583`

R. Stadlmayr, P.S. Szabo, **H. Biber**, H.R. Koslowski, E. Kadletz, C. Cupak, R.A. Wilhelm, M. Schmid, C. Linsmeier, and F. Aumayr
A high temperature dual-mode quartz crystal microbalance technique for erosion and thermal desorption spectroscopy measurements
Review of Scientific Instruments **91** (2020) 125104
`https://doi.org/10.1063/5.0012028`

Conference Contributions

H. Biber
Modeling the sputtering processes on the surface of Mercury in the laboratory
34. Symposium on Surface Science (3S*22), St. Christoph am Arlberg 15.03.2022

H. Biber
Studying the ejection of particles for realistic Mercury analog samples upon He impact
European Geosciences Union (EGU) General Assembly 2022, Wien, 26.05.2022

H. Biber
A novel setup to examine sputtering characteristics of mineral samples
European Geosciences Union (EGU) General Assembly 2021, online, 29.04.2021

H. Biber
Sputtering of Mercury and Moon Analogue Material by Solar Wind Ions
Seminar Institut für Allgemeine Physik (IAP), TU Wien, Wien, 16.11.2021

H. Biber
Comparing sputtering effects of amorphous films and mineral pellets
European Planetary Science Congress 2021 (EPSC 2021), online, 20.09.2021

H. Biber
Investigation of solar wind Helium implantation in Mercury analogues
1st Symposium on Ion-Solid and Atomic Collisions (ISAAC 2020), TU Wien, Wien, 23.09.2020

H. Biber
A quartz crystal microbalance for investigating the angular distribution of particles sputtered from realistic mineral samples
Europlanet Science Congress 2020 (EPSC 2020), online, 21.09.2020

H. Biber
A detailed look on the interaction of solar wind helium with Mercury's surface in

the laboratory
European Geosciences Union (EGU) General Assembly 2020, online, 08.05.2020

H. Biber
Sputtering investigations of Mercury analogue materials using solar wind ions
EPSC-DPS Joint Meeting 2019 (EPSC-DPS 2019), Genf; 16.09.2019

Supervised Students

Martin Wallner
Sputtering investigations of augite using solar wind ions
Project Work (2021)

Daniel Gesell
Erprobung eines Setups zur automatisierten Messung von Sputtering
Project Work (2021)

Caroline Voith
Investigating the Angular Distribution of Sputtered Enstatite Atoms using a Catcher QCM Setup
Project Work (2021)

Johannes Brötzner
A Catcher-QCM Setup for Measuring Sputtering Yields of Wollastonite as Hermean Surface Regolith Analogue
Project Work (2021)

Development of a Graphical User Interface to remotely control Ion Beam Experiments
Project Work (2022)

An Optimised Catcher-QCM Setup to Study the Sputtering of Lunar and Hermean Surface Regolith Analogues
Master Thesis (2022)

Manuel Jahn
Entwerfen, Bauen und Testen einer Sektorblende zur Ionenstrahlanalyse
Bachelor Thesis (2022)

Julian Pichler
Sputtering simulations on rough surfaces and lunar regolith structures
Bachelor Thesis (2022)

Raphael Gurschl
Design and implementation of compact ion optics for a sputter gun setup
Bachelor Thesis (2022)

Fabian Titz
Bachelor Thesis (Ongoing)

1 Introduction

In the harsh space environment, rocky bodies are exposed to a variety of external influences. On our Moon or the planet Mercury due to the lack of a protective atmosphere these processes directly affect the surfaces. Impingement by micrometeorites and energetic ions as well as the irradiation by electromagnetic radiation in various wavelengths continuously erode and alter the surfaces of these celestial bodies. The term space weathering is usually used to sum up the influence of these impacts [1]. Thereby, surfaces of rocky bodies are covered with an altered zone, consisting of a highly modified structure, called the regolith. It is a layer of very loosely packed grains on the bodies' surface as, e.g., on the Moon [2]. When investigating individual grains, however, amorphous rims and vesicles can often be seen on top of crystalline structures. All space weathering effects need to be taken into account when trying to understand the interaction of rocky bodies with the space environment and the resulting modifications of their surfaces [3].

The Sun is directly responsible for a significant fraction of the modifications due to its emission of both, light and a constant flux of energetic ions – the solar wind [4]. The irradiation of rocky bodies with light has a significant impact due to temporal variations in surface temperatures. Without any protective and insulating measures, this irradiation causes drastic changes in surface temperatures during night and day cycles. On Mercury for example temperature variations between less than 100 K and up to 700 K are present [5] at the equator. Furthermore, UV photons and electrons are also able to modify the surface due to photon stimulated desorption and electron stimulated desorption [6, 7]. In contrast to the interaction with light emitted by the sun, the impact of solar wind ions (97 % protons, 3 % ^{4}He^{2+} at about 1 keV per amu [8, 9]) also leads to an influx of material onto the surfaces. Therefore, this stream of ions not only interacts via modifications and erosion by deposition of the ions' energy, but the ions can also become implanted and even interact chemically, e.g., via the formation of hydroxyls from silicates [10]. Depending on how volatile the ions from the solar wind are in the soil determines their respective density in the bodies' near-surface region.

In general, solar wind ions interfere with celestial bodies, affecting them in various ways. The Earth is shielded from the solar wind by its magnetic field, forcing most of the incoming ions on trajectories passing our planet. A fraction of the ions and electrons is however still accelerated towards the cusps, entering Earth's atmosphere [11]. Without the protection of the magnetic field, ions would cause a continuous loss of atmosphere, as is observed for Mars [12]. Interestingly, those atmospheric particles can escape as ions, as they are ionized by the plasma environment and accelerated away from Mars [13], possibly transforming a once wet, water rich atmosphere into the dry one it is now [14]. On their path, they can than even hit Martian moons again, as was for example investigated for Phobos [15,16]. Such an atmosphere, however, also shields the surfaces of rocky bodies from the impinging ion flux. Planets, moons or other bodies without a protective atmosphere are directly exposed to the impingement of the solar wind. The ions can therefore interact with the surface, giving rise to several effects. First of all, material within the ion range suffers from structural changes caused by the collisions of ions with the atoms on the surface and the subsequent energy transfer from the ion towards the solid. This can be seen as formation of amorphous rims on crystal grains on samples returned from the Moon [17]. The protons of the solar wind have a range of a few 10 nm [18] in typical silicate minerals as found on the Moon. In combination with the oxygen in the Lunar soil, the impact of solar wind protons might even be an important source for the water found on the Moon [10,19,20]. Another aspect is the ejection of material due to the impacting ions. The underlying process is called ion sputtering and also has a wide range of technological applications [21]. Just as for an atmosphere, the release of material from the bodies' surface can lead to an ongoing loss of material, even without ionization and in such a scenario depending on the gravitational potential and the emitted particles' velocities [7]. In addition, those particles can populate the space around the irradiated body, leading to an elevated density. A so called exosphere is formed. Other processes leading to particle emission from the surface like the impacts of micro-meteorites, thermal desorption and photon stimulated desorption are also expected to contribute to the exosphere formation [22].

The particles released due to sputtering processes are known to originate from the first few atomic monolayers [23], which makes the exosphere composition very surface sensitive. This fact is of particular interest for the solar systems innermost planet – Mercury. Due to the gravitational pull of the Sun, spacecraft missions towards Mercury are especially challenging, and remote sensing is often preferred instead of performing landing maneuvers. Therefore, the surface sensitivity of the exosphere composition can be utilized to conclude on surface minerals present using measured exosphere data and modelling. Precise input data for those models can enable to retrieve surface information indirectly via exosphere measurements. Probing of the exosphere can for example be performed with telescopes from Earth, which is often done for the sodium component of the exosphere [24]. Furthermore, the BepiColombo mission launched in 2018 by the European Space Agency flying to Mercury is equipped with a mass spectrometer, allowing it to precisely determine the exosphere composition [25].

Providing reliable inputs in order to deliver robust results in exosphere modeling, however, is a challenging task. With the wide range of materials expected to be present on Mercury [26], experimental studies for all of them are not feasible. Instead, sputtering simulations have to be carried out for the major contributors. Oftentimes, the TRIM code from the SRIM package [27] is used for this purpose. The main reason for this is the easy and free access to SRIM via download of an executable from the internet. In addition, the SRIM package comes with a Graphical User Interface (GUI), which allows setting up simulations even for inexperienced users. Several studies with analog materials for planetary research have shown however, that TRIM fails to reproduce experimental data for relevant ion species [28–30]. This highlights the importance of actual laboratory studies, helping to find such discrepancies between simulation results and real physical properties.

Thesis outline

The discussed interaction with the solar wind ions with rock celestial bodies was investigated experimentally and the results compared to calculations for ion sputtering. For this purpose, analog materials as well as lunar material with different crystal structures were irradiated with different species of ions. By the use of specialized microbalance techniques, total sputter yields as well as angular distributions of the ejected material could be measured, improving the understanding of sputtering of rocky bodies in outer space. In chapter 2, basics of the sputter process are discussed. This includes a summary about different effects causing sputtering as well as parameters that influence number and properties of thereby ejected particles. Detailed descriptions about the experimental methods and the simulation efforts used for calculating sputtering of flat (SDTrimSP) and rough samples (SPRAY, SDTrimSP-3D) are given in chapter 3.
The volatility of He at solar wind energy implanted into Mercury analog material was investigated (chapter 4), which can also be of importance for exosphere modeling, since He densities around celestial bodies are coupled to its presence on the surface and its release from it. The next chapters are focused on studying the sputtering of analog materials for rocky bodies (chapter 5) and of sample material from the Apollo 16 mission (chapter 6). In both chapters, computer simulations for evaluating effects of surface structures are used to untangle the influences of surface roughness and crystal structure for different types of samples, allowing a detailed evaluation of experimentally obtained data on sputtering. Finally, the presented results are summarized and discussed in chapter 7.

2 Particle release due to ion impact: Sputtering

When particles like atoms or ions with a kinetic energy above several eV impact onto the surface of a solid, a wide range of effects is triggered, e.g. collisions between the particles and the atoms of the solid take place, allowing the particles to penetrate through the surface. On its path through the solid, a particle continuously transfers energy into the material until it is at rest, gets transmitted or reflected. Therefore, the particle will equilibrate within the solid at some point. Depending on its mobility within the sample, an implanted impactor can then start to diffuse, eventually leaving the solid after desorption at the surface or even stay implanted. This implantation is for example made use of in semiconductor industry, where doping of silicon is achieved this way [31]. Furthermore, it is an important topic in nuclear fusion research, where the energetic hydrogen isotopes used as fuel become implanted in the reactor walls, i.e., fluel ("retention") [32]. Due to the deposition of energy in the solid, excitations are triggered which often lead to the emission of particles or photons. Depending on the exact irradiation conditions and material properties, different emission processes are more likely than others. Those range from electrons to energetic photons and atoms from the solid. For the latter (either as neutrals or as ions) and the accompanying surface modifications, the term *sputtering* is used. The efficiency of the sputter process depends on a wide range of parameters, like for example the sample composition, ion species and energy as well as the angle of impact.

Typically, the efficiency of a sputtering process is quantified by the sputter yield Y_{atoms}, the mean number of particles released per impinging ion:

$$Y_{atoms} = \frac{N_{emit}}{N_{ions}} \tag{2.1}$$

consisting of the numbers of emitted particles N_{emit} and impinging ions N_{ions}. Y_{atoms} describes how fast material is eroded during ion bombardment. The definition of equation 2.1 is however only practical for mono-elemental targets. Otherwise, a more universal definition which is based on the mass change per impinging ion can be used, calculated from the total mass change Δm caused by sputtering:

$$Y = \frac{\Delta m}{N_{ions}}. \tag{2.2}$$

Besides its advantage for compound targets, this definition also allows straight forward evaluation from weighing measurements, where Δm – or a related quantity – is obtained. Such weighting techniques are the most precise tool for investigating sputter yields of materials. They are quantitative without the dependency on additional parameters like the sample density in volumetric measurements. The mass increase due to implanted ions, however, can distort those measurements, as discussed in section 3.1.1.

2.1 Influences on the sputter yield

The term sputtering describes the emission of particles caused by impact of energetic ions (or even neutrals) onto material surfaces. However, the underlying mechanisms can vary, depending on a wide range of ion and sample properties. For many applications and use-cases, singly charged ions with energies in the keV range are relevant. The interaction then takes place in the *linear cascade regime* [33] and the ions' kinetic energy is causal for the sputtering of material. This mechanism is therefore referred to as *kinetic sputtering*. Here, atoms are not removed directly by the impinging ions, but due to recoils in a so-called collision cascade. Many atoms in the solid are set into motion via subsequent collisions. A multitude of collisions is necessary for efficient sputtering, as the normal component (with respect to the surface) of the ion momentum has to be reversed. This becomes more and more likely, as the information about the initial momentum direction is lost for later generations of recoils. The volume below the point of impact is then in an excited state, which can be treated as an enhanced energy density. For particles at the surface, this can lead to removal of material - (kinetic) sputtering occurs [34].
The depth of energy deposition has an influence on the sputter yield. A higher number of excited particles in the surface region leads to a more efficient emission. The arrangement of atoms in the material is a parameter that influences the range of the ions and therefore also energy deposition and sputtering. Oftentimes, amorphous solids with an unordered arrangement of atoms are assumed when sputtering is discussed. In a realistic scenario, however, samples oftentimes possess a crystal structure. This is for example the case for metals – here typically at least polycrystalline structures are found [35] – or for planetary bodies in space, where natural minerals are grown during the bodies' evolution. In the most extreme case of a singe crystal, strong modifications of the sputter yield can be observed, when the ions can enter along low index directions. Here, energy is indeed deposited deeper in the bulk, suppressing the sputter process [36]. This phenomenon is called *channeling*. Polycrystalline samples are often assumed to be similar to an amorphous system, as channeling only occurs for specific orientations between sample and ion beam. However, a recent study by Schlueter *et. al* showed, that still differences in the sputter yield between amorphous and polycrystalline tungsten can be found [37]. In addition to these changes in the sputter yield, also the angular distribution of ejecta can be different when crystalline samples are

irradiated. Here, the emission can be increased in certain directions – so called *Wehner spots* [38].

Another parameter that changes the depth of the collision cascade is the angle between the ion beam and the sample. Under normal incidence, it extends symmetrically down into the bulk, whereas it gets tilted upwards towards the surface for more grazing angles of incidence. This leads to a dependence of the sputter yield on the ion impact angle α (typically measured with respect to the surface normal). The sputter yield first increases monotonically, until the reflection of ions at the topmost surface layer becomes the dominant factor under very grazing angles of incidence and leads to a reduction of the sputter yield again [21].

Indirectly, this dependency also leads to another noticeable effect: Materials with a certain surface roughness can have a significantly altered sputter yield. Considering a flat surface and slightly increasing its roughness, the local angles α_loc between the ions and the surface start to deviate from the global irradiation angle α. Therefore, $Y_{rough}\left(\alpha\right)$ can be approximated by mapping the distribution of local angles α_{loc} on the angular dependence of the sputter yield $Y_{flat}\left(\alpha\right)$ [39, 40]. The contribution to the roughness induced changes in sputter yield become less pronounced when the roughness increases. In general, a variety of effects causes the differences between flat and rough surfaces. The most important of those are illustrated in figure 2.1.

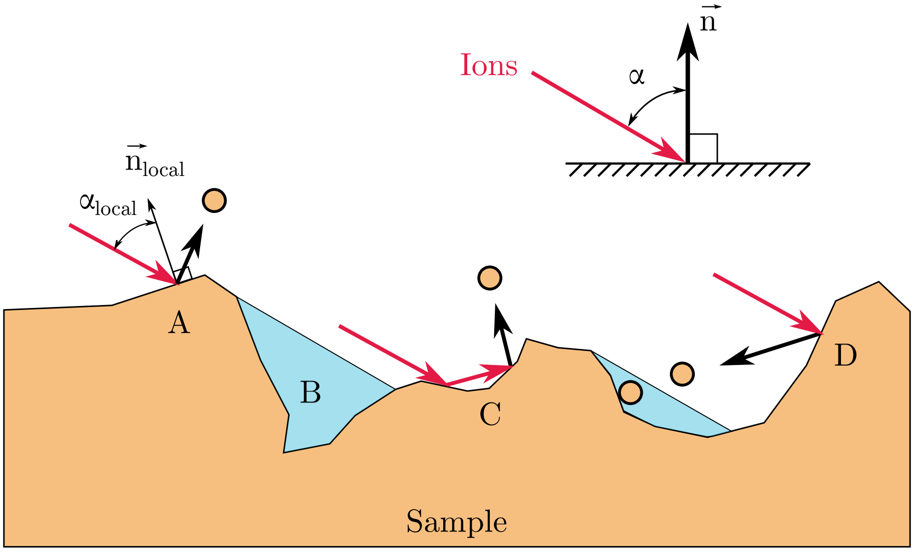

Figure 2.1: Influence of surface roughness on the sputter process. Local impact angles α_{loc} differ from the global angle α (A), some areas are shadowed by neighboring hills (light blue, B), reflected ions can still lead do sputtering (C) and sputtered particles can be deposited again (D). Figure adapted from [41].

For surfaces with a more pronounced surface topography, effects like redeposition of sputtered material, shadowing of certain regions and the sputtering by reflected ions become more important [41,42]. When atoms are sputtered in deep grooves or holes, they are not able to escape and get deposited again. This effectively reduces the sputter yield for most angles of incidence. In general, a less pronounced angular dependence of Y is found for conventionally rough surfaces, with an increased sputter yield for normal incidence and decreased values towards the maximum of $Y(\alpha)$.

Extreme cases where the whole surface is made up of foam-like structures can for example be found in nuclear fusion research where so-called *tungsten fuzz* is forming under high flux/high fluence conditions [43]. Here, the sputter yield is indeed drastically reduced [44]. In space science, another distinct type of structure can be found. Surfaces of rocky bodies in the solar system like the Moon are covered with a layer of very loose material. This powder has grains with a size ranging up to the mm range [2]. Due to the loose packing and the resulting high porosity, a similar situation as found for tungsten fuzz in fusion science is expected. Ions can reach deep into the sample, while emitted particles cannot escape anymore from those sites. Oftentimes roughness is characterized by looking at elevations of the surfaces features. For this purpose, the average height is taken as base line and the root mean square average from the deviations of this center line is calculated, called RMS *roughness* (often simply referred to as RMS value or RMS). However, Cupak *et. al* [41] has performed a simulation study on roughness effects, artificially varying the RMS via a scaling of height values for different given surfaces. A correlation between the changes in sputter yield and RMS could not be seen. However, a different universal parameter was found within the distribution of local surface slopes. The first moment of this distribution, called δ_m, can be used to estimate the roughness effects for different surface textures and for a wide range of RMS values. A theoretical investigation by Szabo *et. al* validated the universality of δ_m for roughness characterization [42].

Besides influences on kinetic sputtering discussed so far, another parameter causing variations in particle emission upon ion impact can be found in the charge state of the ions. Due to the removal of electrons from the neutral atoms, ions carry a certain amount of potential energy, namely their ionization energy. For each electron that has to be removed for ionization, an increasing amount of energy has to be supplied. By that, potential energies in the keV range can be stored in the ions, even exceeding the ions' kinetic energy [45]. Just as kinetic energy, the ions' potential energy is also transferred to the target upon impact. The mechanisms of excitation in the sample, however, are vastly different and potential energy is thereby transferred to the electronic system. The potential energy of ions is generally transferred into the first material layers [46, 47]. Depending on the ions' charge state and the irradiated sample, this effect alone can also lead to sputtering. This contribution to the sputter process is termed potential sputtering. It is observed for insulating materials and could so far not be seen on metal samples, as the electronic excitations can there be dissipated fast enough [48].

In literature, sputter yields are oftentimes just given as static values. Those are typically steady state values, which are reached after some fluence or an average over an extended irradiation phase. Due to the multitude of influences on the sputter yield, however, dynamic changes during prolonged irradiations are very common. Especially the beginning of an irradiation, the sputtering characteristics can vary significantly:
First of all, samples brought from air into vacuum are obviously contaminated in general. Therefore, sample surfaces have to be prepared in vacuum after installation in experimental chambers. Sputter cleaning with Ar^+ with a kinetic energy of some keV is a very commonly used method (see e.g. [49]). When measuring sputter yields *in-situ* during such a cleaning procedure, a significant dynamic can be observed due to the removal of the much weaker bound adsorbates (this can be seen in figure 3.8 in section 3.3.1).

Dynamic sputtering behavior can, however, also occur on ideally prepared (cleaned) samples. Those are caused by a change in sample stoichiometry or structure. Especially composed targets are effected by different sputter yields of their constituents Y_i [50]. Here, sputter rates change dynamically, until the sputtered stoichiometry equals the bulk stoichiometry($^{Y_i}/_{Y_j} = {}^{c_i}/_{c_j}$) and an equilibrium is reached. In-between, even oscillations in partial sputter yields due to the implantation of ions can occur as was studied for light carbon ions impinging on tungsten [51].

An extreme example of such a fluence dependence in sputtering due to different Y_i can be found in the case of potential sputtering. For the enhanced emission of particles due to the potential energy of the ions, a metallization of the sample surface is observed. This is caused by preferential emission of specific particles from compounds, like, e.g., O for oxide insulators or F for LiF. That process induces a strong dependence of the total sputter yield Y on the irradiation fluence [30, 52]. With the superposition of kinetic and potential sputtering, a complex interplay of metallization by the potential energy and the re-supply of, e.g., oxygen from below the surface due to the kinetic sputtering takes place. Nevertheless, sputter equilibrium will be reached after a certain time. Depending on the strength of potential sputtering – not affecting all values of Y_i – and compared to the kinetic contribution, surface compositions can be drastically different from the respective bulk composition [30, 52].

Also the discussed drastic differences in sputtering between crystalline and amorphous samples of same stoichiometry can lead to dynamics in the sputter yield, induced by changes of material phases. Due to the production of damages in the sample, crystals are amorphized within the ions' range [53]. Therefore, a transition in the sputtering behavior from that of a crystal to that of an amorphous solid can occur.

When changes in structure are discussed, variations in sputter yield caused by a dynamic change of surface roughness of the sample need to be considered as well. Since sputtering leads to the emission of particles from a surface, ion impact also leads to modifications of the latter. Due to the significant influence of surface roughness on Y, dynamic variations of the roughness also lead to a dynamic sputtering behavior. Depending on the exact investigated system, the erosion of surfaces can lead to both a smoothening of rough surfaces as well as to the formation of structures like for example periodic ripples [54–56]. These effects can even take place as combined with changes of sample composition due to preferential sputtering, as was observed for example for oxidized iron samples [57].

2.2 State of the art: Calculations of sputtering

With the complex interplay between various effects on the sputter process, calculations of the latter are crucial for understanding the underlying mechanisms for various investigated cases. Although analytic models for calculating sputter yields exist, calculations are mainly done via computer simulations. Various different tools exist, allowing to focus on specific parameters like, e.g., ion species, sample composition or surface structures. However, there are two main approaches, both based on Monte Carlo (MC) methods [58]:

An alternative approach can be found in *Binary Collision Approximation* (BCA) codes. Instead of dealing with a solid made up of single atoms interacting with each other, an amorphous solid is assumed (except a small number of variants which include the crystal structure, like for example MARLOWE [59]). The main difference to the MD simulations is the range of interaction considered. Each collision partner – impactor or recoil – is treated independently, giving this approach its name. Collision sites are connected to the target density ρ and typically happen after $\rho^{1/3}$. However, this might as well be dressed with a random prefactor [60]. Impact parameter and azimuth-scattering angle are then also chosen randomly, giving the code its MC nature. The dynamics of the impact are subsequently calculated according to the randomly chosen impact parameter. Energy is therefore spread through the cascade of recoils and particles below a certain cutoff-energy E_{cutoff} are considered as stopped and no longer followed. The suitable value of E_{cutoff} for BCA calculations with focus on sputtering depends strongly on the choice of underlying model for particle emission. Usually, a so-called Surface Binding Model (SBM) is considered: In similarity to the work function for electrons [61], atoms thereby need to overcome a certain threshold in order to leave the solid.

This threshold is called surface binding energy E_{SB}. It is a planar barrier at the surface, therefore the energy normal to the surface of a particle has to be bigger than this surface binding energy: $E_\perp = \frac{p_\perp^2}{2m} > E_{SB}$. When the simulations are only carried out for sputtering, E_{cutoff} can be equal to the smallest value of E_{SB} in the target for a SBM, as particles with smaller energies cannot overcome E_{SB} anyways. At the time writing, the SBM model is under discussion, as E_{SB} is more or less a fitting parameter for simulations, although often approximated by the material's heat of sublimation [62]. This approach fails at the latest when working with complex compounds, where no heat of sublimation of the constituents can be defined meaningfully.

Another model used for calculations of kinetic sputtering is the so-called Bulk Binding Model (BBM). Here, E_{SB} is omitted and replaced by an energy subtraction for every target particle set in motion. This energy is calculated from the sublimation enthalpy of the material. Recent work in this field by Hofsäss and Stegmaier [23] showed very good agreement with experimental data without any fitting parameter and can also be used for compound targets. In the case of a BBM, Hofsäss and Stegmaier recommend a value of $E_{cutoff} = {}^1\!/_3 E_S$ with the sublimation energy E_S of the material [23].

The main advantage of BCA codes is their short computation time. Sputter yields with sufficient statistics can be calculated within a few minutes on a regular desktop computer. The results however depend on several input parameters, which have to be either chosen correctly (e.g. the interaction potential) or even fitted to experimental data (like E_{SB}). Recent developments toward the use of BBM based implementations are a promising candidate to overcome this uncertainty due to parameter fitting.

The most prominent code based on BCA is TRIM (**TR**ansport of **I**ons in **M**atter), which comes together with the SRIM (**S**topping and **R**ange of **I**ons in **M**atter) package [63]. The reasons for this are easy accessibility – it can simply be downloaded from the internet[1] – and the fact that simulations are straight-forward to set up as it comes with a graphical user interface. The source code, however, is proprietary and it is limited in adjustable parameters. Furthermore several publications have shown, that sputter yields obtained with SRIM/TRIM are not reproducing experimental results well [28–30, 64]. Its use for sputter yield calculations is therefore not recommended. More accurate and continuously maintained programs with available source code - like SDTrimSP [65], see section 3.4.1 should be used instead.

Due to the typical approach of BCA codes of having an amorphous solid with impacts happening at random locations, infinitely expanding, plane surfaces are

---

[1] `http://www.srim.org/`

assumed. In that case, a code is referred to as being a one-dimentional (*1D*) code. There are, however, also extensions available, allowing calculations of the interactions between ions and textured surfaces. A first step toward realistic surfaces can be achieved with *2D* codes like the SDTrimSP-based code SDTrimSP-2D [66]. Here, structures expanding infinitely in one surface direction can be generated. This allows for textures in one cut and grooves perpendicular to that. The last step is made with 3D-codes, where full surface information is computed. Two different codes which are capable of such are TRI3DYN [67] and SDtrimSP-3D [68], with the latter being discussed in more detail in section 3.4.2. In the 3D BCA codes in general, the solid is made up from volume pieces, so-called *voxels*. Those than also become computationally demanding, as a high number of pseudo-particles is needed for sufficient probing of the surface.

3 Methods

In this chapter, the tools needed for the execution of this thesis' studies are presented. They range from experimental methods required for sputtering and implantation data of various sample types to computer simulations needed to understand the underlying physical processes.

3.1 Experimental Methods

The experiments performed during this thesis were mainly carried out at TU Wien. There, various experimental setups are available, allowing the investigations of sputtering during ion bombardment of various samples with high precision based on *in-situ* microbalance techniques. The exact methodologies needed are explained in detail in this section.

3.1.1 Quartz Crystal Microbalance Techniques

So called Quartz Crystal Microbalance (QCM) based techniques have a wide range of applications. They are oftentimes used during thin film deposition for calibration, as they can be used to detect small mass changes in-situ and therefore do not require extraction of a sample for evaluation, but are also used a lot in biophysics to monitor the binding and growing of molecules on a substrate [69]. Small variations in sample mass can thereby be monitored by utilizing the dependence of the natural frequency f of resonators on their mass m. The principle was described by Sauerbrey [70] who derived the linear relation between small changes of resonator mass and natural frequency:

$$\Delta m = -m_Q \frac{\Delta f}{f_Q} \tag{3.1}$$

Here, m_Q and f_Q are the resonator's initial mass and frequency, whereas Δm and Δf are the according deviations from those. The relation is not only true for the resonator itself, but also holds for other materials deposited on the quartz, participating in the oscillating motion. This can then be used to investigate mass increase or depletion of this layer, caused by physical or chemical processes. At TU Wien, there is a long tradition of measurements using such a QCM for investigating ion solid interactions [71,72]. The special electronics used allow to measure changes in resonance frequency in the $^{\mathrm{mHz}}/_{\mathrm{min}}$ range at a noise level in the mHz regime. With a resonator base frequency of 6 MHz, mass changes per area and time in the order of 10 pg cm^{-2} s^{-1} can be resolved. This is below 1 ‰ of a monolayer per second for silicate minerals like wollastonite ($CaSiO_3$) [71–73]. This high resolution, allows not only to investigate steady state sputtering with the QCM, where a constant rate of mass change is observable, (as linear change in resonance frequency over time) but also to observe dynamic processes, e.g., changes in sputter yield due to ion induced modifications of the surface structure [74]. The resonators used during this thesis were solely *KVG Quartz Crystal Technology GmbH XA-3641* plano-convex SC-cut quartz crystal resonator discs with a diameter of 14 mm. A major drawback of the QCM technique is the requirement of a suitable thin film deposition technique. Depending on the desired material and structure, different methods have to be used. Furthermore, parameters like crystal structure or surface morphology are often either challenging to control or not reproducible at all. Nevertheless, the wide range of materials that can be deposited onto such resonators and the ability to observe mass changes with high resolution *in-situ* makes them an ideal tool to study sputtering during ion irradiation, as has been shown in numerous publications, e.g., references [29, 72, 75, 76].

When the ion current j is homogeneous across the whole quartz (or at least its sensitive area [70], steady state sputter yields are directly proportional to the slope of the frequency change, $Y \propto {}^{\Delta f}/_{\Delta t}$. Starting with the definition of the sputter yield (equation 2.2), Sauerbrey's equation (3.1) and the relation between the number of ions N_{ions} hitting the sample in a time span Δt and the ion current I, their charge state q and the elemental charge e

$$N_{ions} = \frac{I\Delta t}{qe}, \tag{3.2}$$

an expression of the sputter yield Y from the quartz signals can be derived:

$$Y = \frac{\Delta m}{N_{ions}} = \frac{m_Q}{f_Q}\frac{\Delta f}{N_{ions}} = \frac{\rho_Q d_Q A_Q}{f_Q}\frac{qe\Delta f}{I\Delta t} = \frac{\rho_Q d_Q}{f_Q}\frac{qe\Delta f}{j\Delta t} = C\frac{q}{j}\frac{\Delta f}{\Delta t}. \tag{3.3}$$

The quartz constants indicated by index Q are combined with e in a factor C and listed in table 3.1.

Table 3.1: Definition of variables corresponding to physical properties of the quartz resonators

m_Q	mass
f_Q	resonance frequency
ρ_Q	density
d_Q	thickness
A_Q	area

Therefore, ion charge state, current density and slope of the frequency are the only measurement quantities needed for the calculation of Y in a steady state condition. In such a case, a linear fit can be made to the frequency data, outputting the slope ${}^{\Delta f}/_{\Delta t}$. Information about the ion beam must be provided from separate measurements, characterizing it before and/or after an irradiation. For dynamically changing sputter yields, equation 3.3 can also be evaluated locally from the $f(t)$ data. In order to do so, ${}^{\Delta f}/_{\Delta t}$ must be calculated between actual points of measurements discretized in time. Due to noise in the experimental data, the resulting values of Y from calculated raw data scatter significantly. This can be improved by applying a filter to the raw data set. The so-called Savitzky–Golay (SG) filter [77] was used during this thesis for that purpose. Most recent investigations on that topic at the time of writing however show, that different filtering approaches like sinc function based ones are more suitable, especially when the derivative of the measurement quantity is needed [78]. The used SG Filter has the number of data points that are used for smoothing and the number of iterations as parameter. The combination of 30 data points and three iterations delivered good results most of the time. Data based on local slopes were only used for qualitative interpretation of measurements, while steady state slopes and total mass changes were used for quantitative analysis. The time resolution available when performing local evaluation of ${}^{\Delta f}/_{\Delta t}$ depends on the exact setup used. Both, an analog circuit, where values are obtained with an universal counter after one second integration time described in [75] and a more flexible computer based setup were used. For the latter, a combination of an Analog-Digital-Converter (ADC), a function generator and a regulating script on the computer are needed. This allows to excite overtone modes of the resonators, which can be used for temperature compensation [73]. It comes at the cost of more complexity and a reduced acquisition rate of 0.1 - 0.2 frequency points per second.

Please note, that the ansatz presented in equation 3.3 is only valid, if sputtering is the only reason for mass changes. The ions impinging on sample surfaces however are not only causing sputtering, but are also penetrating into the sample. Depending on the ions' range and their mobility in the sample, projectiles can stay in the sample and become implanted permanently. In this case, equation 3.3 no longer holds. It then calculates the net mass change per impinging ion Δm_{ion} rather than the sputter yield.

Without mobility of the projectiles in the sample after their stopping, the release of those particles starts when the surface – continuously eroded by sputtering – reaches the zone of implanted material: At first, the implanted ions are localized around the range of the ions, while with ongoing implantation, a layer with constant concentration in depth is formed. When the receding surface enters this plateau, a steady state of implantation and release of projectiles is reached. For

mobile projectiles, similar arguments hold, but different fluences are needed to reach this steady state value. Determining the necessary fluence is, however, challenging, as there is a non-trivial dependence on diffusion properties. An example for the frequency dependence during a measurement with implantation is illustrated in figure 3.1. At first, an initial drop in frequency due to a heating of the quartz by the impacting ion beam can be seen, which will be discussed in detail below . Then, an extensive implantation phase follows, which often consists of various phases (cf. the kink marked in the insert after about 3200 s).
If a constant rate of sputtering (for this Y and j need to be constant) can be assumed during the whole irradiation, the amount of implanted material $m_{impl}(t)$ as a function of time can be calculated from a known sputter yield Y and the measured total mass change $\Delta m(t)$ as:

$$\Delta m(t) = \int_{t_0}^{t} (m_{\dot{impl}}(t') - Y)dt' = \int_{t_0}^{t} m_{\dot{impl}}(t')dt' - Y \cdot (t - t_0) \tag{3.4}$$

$$\Rightarrow m_{impl}(t) = \int_{t_0}^{t} m_{\dot{impl}}(t')dt' = \Delta m(t) + Y \cdot (t - t_0) \tag{3.5}$$

The value of Y can be obtained from the steady state slope of the frequency over time curve. Whether the sputter yield is altered during the measurement due to the concentration of implants at the surface needs to be verified either with computer simulations or with a different approach for sputter yield measurements, like for example the catcher QCM presented in section 3.1.2.

So far, only the dependency of the QCM resonance frequency on mass changes was discussed. However, in addition to implantation and sputtering effects, energy gets deposited into the sample by the impinging ion beam. With energies of some keV and currents of up to a few μA, a total power in the mW range is heating the quartz resonators. They are therefore not in thermal equilibrium with their environment anymore, as soon as an irradiation starts and therefore heat up. The resonance frequency can have a very pronounced dependency on the temperature, with the exact shape depending on the crystals cut angles [79]. The resonators used during this thesis had a saddle point in the T over f curve at about $25°C$, reducing thermal effects when operated in this temperature regime, where all irradiations performed during this thesis besides one series in section 4, where it is stated otherwise. Nevertheless, temperature changes are observable during most of the measurements. The resonance frequency is then a function of both, mass and temperature. The according changes can be treated separately:

$$\Delta f = \Delta f(\Delta m) + \Delta f(\Delta T). \tag{3.6}$$

A precise evaluation of the mass change according to Sauerbrey's equation (3.1) becomes valid again, when $\Delta T = 0$ in the time span Δt. Therefore, the first few 100 s of an irradiation phase typically have to be disregarded. The relative influence on the signals is depending very much on the ion species. This is not due to the thermal effect – the total power dissipated $P = U_{accel}\, I_{ions}$ is only influenced by minor differences in the ions reflection coefficient – but due to differences in sputter yield. Figure 3.1 illustrates the massive influence on the signals caused by temperature changes at the QCM for irradiations with $\mathrm{H_2}^+$ ions. The initial drop in frequency of about 50 Hz (seen in detail in the insert) is reversed after the ion beam is turned off after 66000 s. In combination with the small sputter yield, the temperature effect is equivalent to some 1000 s of sputtering in the steady state condition, which is reached after about 20000 s due to an implantation phase. Note that this effect is more drastic for lighter ions (e.g. He^+) compared to Ar^+: As the achievable currents from the ion source increase for lighter projectiles, also the temperature effect rises. At the same time ${}^{\Delta f}/_{\Delta t}$ values are similar because of the smaller sputter yield at the used silicate samples. This changes the ratio between steady state slope and Δt at the beginning and end of irradiation phases.

For representative materials of space weathering studies, minerals are used as source material. These are then transferred onto the quartz resonators via Pulsed Laser Deposition (PLD). In order to preserve the original stoichiometry, this process has to be carried out under an oxygen background pressure. However, oftentimes, this technique has the drawback that the films end up being amorphous [30,80]. Annealing of the films for crystal formation or deposition at temperatures near the melting point of the minerals cannot be done, due to a destructive phase transition of the used quartz crystals at 847 K [73, 81]. Therefore, another method has to be used to investigate sputtering for those samples, where sputter yield measurements cannot be performed with a classical QCM setup.

3.1.2 Catcher QCM

This extension of the classical QCM technique removes the limitations of the QCM method to thin films. It utilizes the high sensitivity to mass changes of the resonator based microbalance setups but moves away from directly irradiating the QCMs. It consists of a second balance, which is used in a catching configuration, called catcher QCM (catcher, C-QCM). Instead of the mass depletion due to sputtering, deposition rates caused by particles released from another sample are measured. That way, a much more liberal choice of irradiated samples becomes possible, allowing the studying of sample parameters not accessible with a classical QCM. For example, metal platelets with a specific surface finish can be used as irradiated sample, where the effects of specific structures and features on the surface on the sputtering process can be investigated [41, 44]. The use-cases relevant for this thesis can be found in crystalline phases not reproduced by the

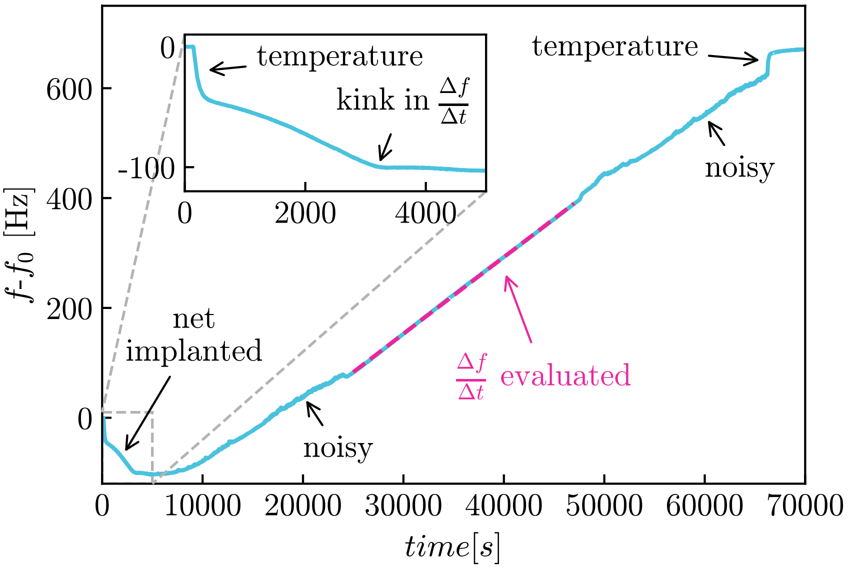

Figure 3.1: Frequency change of a QCM with a pyroxene coating under H_2^+ irradiations. Thermal effects when turning on/off the ion beam can be seen in the inset and at t = 66000 s. The insert also highlights the dynamic of the implantation phase, where $^{\Delta f}/_{\Delta t}$ is even negativ, which means net implantation. In between there are phases with stable but noisy signals and a very stable area from about 25000 s to 45000 s, where a sputter yield can be extracted.

deposition process or in samples that shall be investigated unmodified due to their exceptional origin like samples from the Moon. Here, mineral pieces as whole or pellets pressed from powdered material can be used [82, 83].

The use of a C-QCM further enables an analysis of the angular distribution of sputtered particles, when the geometry between catcher and irradiation center can be varied. Figure 3.2 shows the geometry of such an ideal measurement scenario. The catcher is orientated towards the irradiation center and movable around it at a fixed distance r_C. The angle between the two samples β can be varied almost independently from the irradiation angle α.

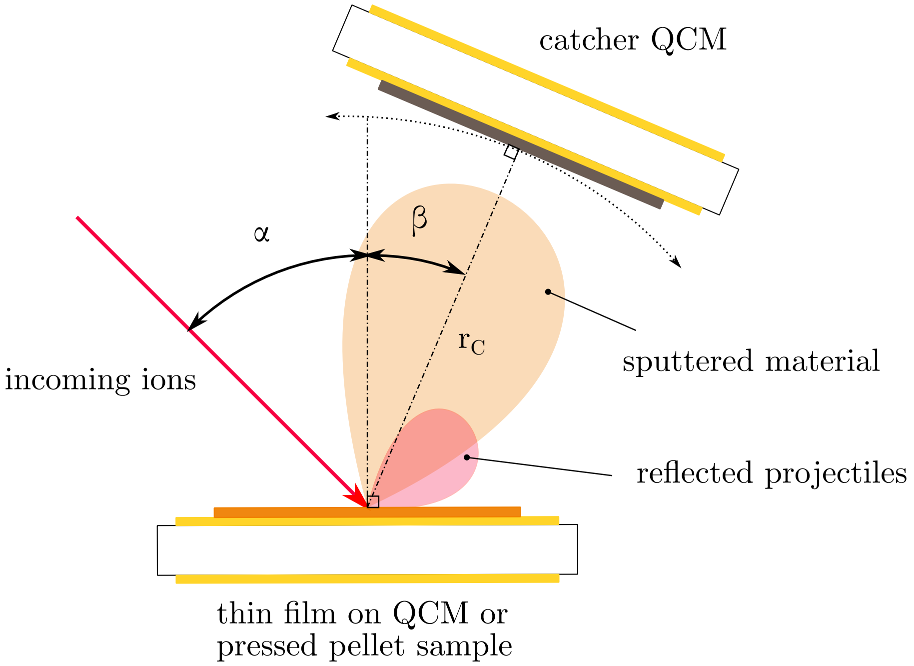

Figure 3.2: Experiment geometry for both, irradiations of QCM for direct sputter yield measurements (only lower half) and including the catcher QCM sketched above. The angles α and β can be varied independently from each other. There are however constraints on β due to a blocking of the ion beam. The primary QCM was exchanged with pressed pellets *in-situ* via movement of the sample holder. The distance between the two samples was $r_C = 17\,\text{mm}$ for all measurements presented in this thesis. Figure adapted from [83]

In the experiment, possible positions of the catcher are limited in backward direction by the finite size of the C-QCM and the resulting blocking of the ion beam. Considering the geometry shown in figure 3.2, the sum of α and β must therefore not be smaller than 35°. This limits also the range of the ion impact angle α, as the catcher cannot be moved into the emission cone – located close to the surface normal of the irradiated sample – for $\alpha < 45°$.

Despite the ideal geometry the C-QCM comes in various flavors. It was originally pioneered by Berger *et al.* with a C-QCM mounted on a linear manipulator, placed orthogonal to the ion beam and the axis of rotation of the irradiated samples [84]. This setup has the advantage of simple installation into an existing experimental system, but is limited in geometry and interpretation of the experimental results. The catcher is here not facing the sample and no sweep of β at constant distance r_C is possible. Berger *et al.* therefore varied the position of the irradiated sample in ion beam direction – and therefore with respect to the C-QCM – in order to get some spacial information about the sputtered particles. C. Cupak built a much more complex setup, based on a 5-axis manipulator and still mounted laterally [85]. With a tilting mechanism, circular arcs around the center of irradiation can be measured, while the C-QCM is always facing inwards. In contrast to the simple setup on a linear manipulator, measurements at different β values can be performed at the same distance r_C, which is a major improvement compared to the original design. Just as in the setup introduced by Berger *et al.*, the manipulator is placed orthogonal to both ion beam and target sample holder, namely on the side of the vacuum chamber. Here, the reachable angles β are restricted by the size and the travel of the used manipulator. Another disadvantage is the need of 3 manipulators and a complex tilting mechanism for changes of the catcher position while keeping the distance r_C constant. This is a possible source of errors on the one hand and brings additional uncertainty in r_C on the other hand. However, such a setup is still quite compact due to the lateral mounting and can work in a tabletop experiment.

In the course of this thesis, a different approach was developed, making use of the symmetry of the problem that is to be investigated. Instead of mounting the C-QCM on a manipulator perpendicular to the primary axis of rotation, another rotary manipulator is placed at the same axis, but from the opposite side. Thereby the ideal experiment geometry shown in figure 3.2 can be achieved without limitations in β by manipulator travel. By using a $xyz\phi$- manipulator, an alignment of the axis is possible, which can be necessary after closing the vacuum chamber due to wobble of the manipulator rods. With the coaxial mounting of both irradiated sample and C-QCM, only the rotary manipulator needs to be moved during measurements. Automation of the angular distributions of ejecta could therefore easily be implemented by means of a single servo motor.
As the intensity $I_{detector}$ of sputtered particles impinging on a detector area $A_{detector}$

follows an inverse square law with the distance r, $I_{detector} \propto \frac{1}{r^2}$, it is important to minimize variations in the distance when moving the C-QCM around the irradiated samples. A small wobble of the manipulator rod can cause such variations, even when initially aligned coaxially. In order to address this circumstance, the manipulator of the C-QCM is equipped with a centered rod, which can glide in a sleeve mounted on the primary holder. The play between the two pieces is in the sub-millimeter regime. At a distance of $r_C = 17$mm, which was used for all measurements performed with this setup and presented in this thesis, movement in r_C can therefore be neglected as uncertainty factor. A 3D-CAD drawing of the newly developed sample holder system can be seen in figure 3.3.

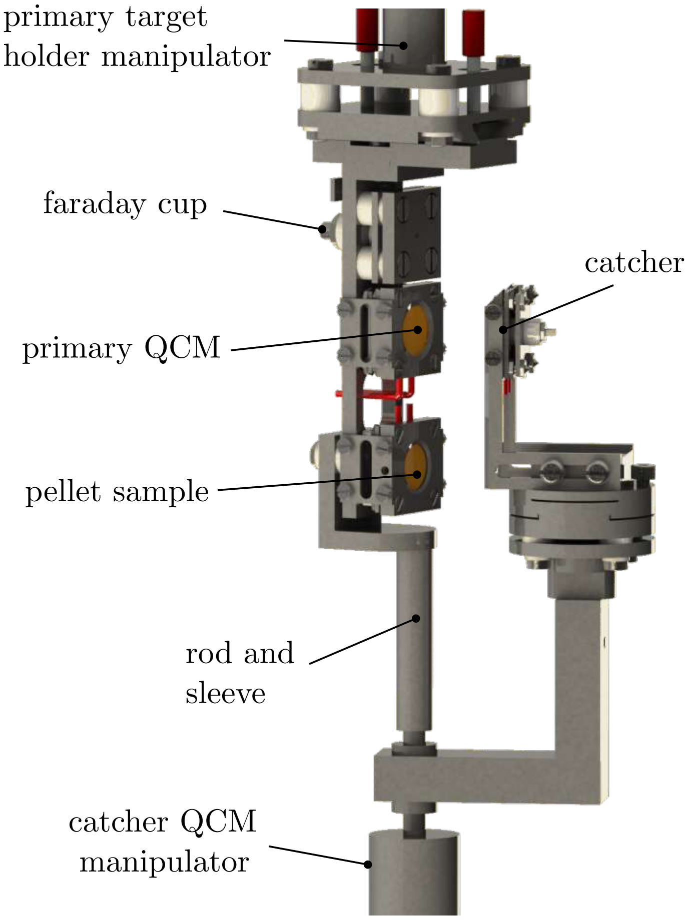

Figure 3.3: Rendering of a 3D-CAD drawing of both the primary sample holder and the Catcher QCM on its sample holder.

The $xyz\phi$- manipulator used for the catcher allows not only for an alignment of the sample holder axis, but also to move the C-QCM into and out of the locking position. For irradiations, it can be moved into the plane spanned by rotating the ion beam vector around the irradiated sample holder axis. When no measurements with the C-QCM are ongoing, it can be withdrawn from the locking position and moved further away in a parking position. This is important, as the primary sample holder needs to be movable in several directions in order to determine the ion current impinging on the irradiated sample.

A problem that arises with the use of a catcher quartz – which is not irradiated with the ions – is the meaningful and quantitative evaluation of the obtained signals. A direct calculation of a sputter yield as for the classical QCM (equation 3.3) is not possible anymore. In the classical case, the whole sensitive Quartz area is irradiated with a homogeneous ion beam and can therefore be reduced in equation 3.3, making the current density j the scaling factor between frequency change and sputter yield. This cannot be done for the C-QCM, as the signals there are independent from the size of the irradiation spot - apart from geometric effects. A first method proposed by Berger *et al.* [84] and used by Stadlmayr *et al.* [44] and Cupak *et al.* [41] defines a catcher yield Y_C in analogy to the sputter yield Y as mass change on the C-QCM per impinging ion. Based on the definition of the sputter yield (equation 2.2) and Sauerbrey's equation (3.1), the catcher yield was also defined as

$$Y_C = \frac{\Delta m}{N_{ions}^{total}} \tag{3.7}$$

with the total number of ions impinging on the sample surface N_{ions}^{total} and the total mass change of the sample Δm. When this is extended in the same manner as equation 3.3, one ends up with

$$Y_C = \frac{\rho_Q d_Q A_Q}{f_Q} \cdot \frac{qe}{I} \cdot \frac{\Delta f}{\Delta t} = \frac{\rho_Q d_Q A_Q}{f_Q} \cdot \frac{qe}{j A_{beam}} \cdot \frac{\Delta f}{\Delta t}, \tag{3.8}$$

where the total current I is expressed via its density j and area A_{beam}. In equation 3.8, the actual size of the resonator needs to be known. The previous convention was to use the so called *active area* A_{active} of the quartz resonators. P.S. Szabo performed test measurements and found a vanishing sensitivity of the resonance frequency to mass changes outside an area with a radius of 3.5 mm for the used microbalances [86]. Stadlmayr *et al.* and Cupak *et al.* consequently followed that convention. Figure 3.4 shows the result of P.S. Szabo's evaluation. Due to the Gaussian profile, other radii could be used as well, just including different fractions of the sensitive area, which is a major drawback of this ansatz. Furthermore, the measurement geometry is not taken into account. Placing the C-QCM at a different distance r_C to the target will lead to drastically different results due to the $1/r_C^2$ dependence of the sputtered particle flux.

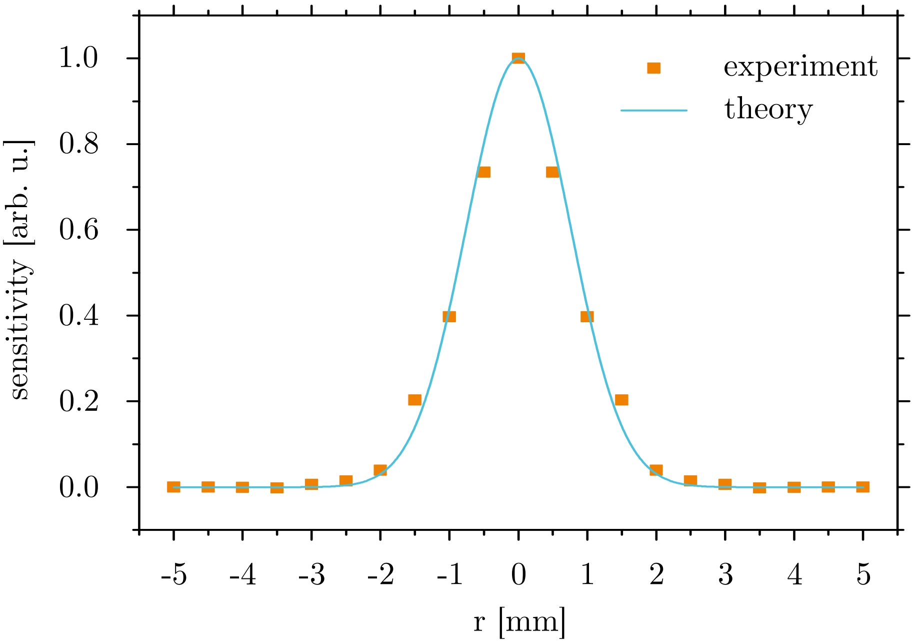

Figure 3.4: Radial sensitivity of the resonance frequency to mass changes of a QCM. Measurements were performed on the type of resonator used during this thesis. Figure adapted from [86].

For this thesis, adaptations to this quantity were made, which overcome both of those limitations. By normalizing the value of Y_C from equation 3.8 with the solid angle of the quartz, a quantity independent of the measurement geometry and without the choice of A_{active} can be calculated:

$$\begin{aligned} Y_{C,\Omega} &= \frac{\Delta m}{N_{ion}} \frac{1}{\Omega_C} = -\frac{qe_0}{I} \frac{m_Q}{f_Q} \frac{\Delta f}{\Delta t} \frac{1}{\Omega_C} \\ &\approx -\frac{qe_0}{I} \frac{\rho_Q \; d_Q \; A_Q \; r_C^2}{A_Q \; f_Q} \frac{\Delta f}{\Delta t} \\ &\approx -\frac{qe_0}{I} \frac{\rho_Q \; d_Q \; r_C^2}{f_Q} \frac{\Delta f}{\Delta t} \end{aligned} \tag{3.9}$$

This equation is valid, when the spherical surface at distance r_C can be approximated by the plane, sensitive quartz surface $A_Q/r_C^2 \approx 1/\Omega_C$. The quantity $Y_{C,\Omega}$ is then the mass change per ion and solid angle at the C-QCM, under the constraints of the Gaussian sensitivity function.

Due to the use of a QCM with same stoichiometry, a calibration of the obtained signals to sputter yields is possible. Thereby, conventional sputter yield measurements are performed under identical conditions. With the signal ratio r at the catcher at measurement cycles with both samples, a calculation of the pellet sputter yield Y_{pellet} from the sputter yield obtained at the QCM Y_{QCM} is possible:

$$Y_{pellet} = r \times Y_{QCM} \tag{3.10}$$

This ratio r can be calculated directly from the single data points $Y_{C,i}$ via a weighted sum, which is equal to the ratio of the integration over the data points considering equal spacing:

$$r = \frac{1}{\sum Y_{c,QCM,i}} \sum Y_{c,QCM,i} \frac{Y_{c,Pellet,i}}{Y_{c,QCM,i}} = \frac{\sum Y_{c,Pellet,i}}{\sum Y_{c,QCM,i}} \tag{3.11}$$

Another option used is via integration of adequate fitting functions and taking the ratio thereof. A modified cosine law can be applied, modifying its shape by an exponent and allowing for a tilt, induced by the non-normal incidence angles (see e.g. [87]):

$$Y_{C,\Omega} \propto A \cos^n (\beta - \zeta) \tag{3.12}$$

3.1.3 Thermal Desorption Spectroscopy

Often used in surface science and nuclear fusion research, Thermal Desorption Spectroscopy (TDS) – also called Temperature Programmed Desorption (TPD)

– allows to investigate the thermal activation of release mechanisms from adsorbents [88] and from implanted ions [89]. The latter is of interest for ion-solid interaction, as the impinging ions can be retained in the irradiated samples, even at room temperature – a fact that is also used for doping of semiconductors [31]. With the combination of heatable samples and a mass spectrometer, TDS can be performed by linearly ramping up the sample temperature while simultaneously measuring the partial pressure of the gas of interest in the experimental chamber with a mass spectrometer. Depending on the activation energy of the release process and its order, increases in the mass spectrometer signal can be seen at different temperatures. There can also be several peaks at different temperatures, when the implants are trapped at sites with different binding energy [90].

When irradiating thin films on QCMs, the information of both techniques can be combined, allowing also to determine the amount of material released during the TPD process. Due to the strong temperature dependence of the quartz resonance frequency, the signal from mass loss due to outgassing material is superimposed to the temperature related changes of the quartz frequency. There also exists a method using the third overtone to compensate this temperature effect for quartz resonators, but this requires quasi-simultaneous excitation and recording of ground mode and third overtone [73]. Furthermore, the exact evaluation is delicate due to the dominant temperature effect on the frequencies. However, comparing the fundamental quartz frequency f_Q before and after a TDS – each time at the same temperature – mass loss per unit area due to the heating process can be calculated directly from Sauerbrey's equation (equation 3.1). This can then be compared with the total implanted mass per unit area from equation 3.4.

Just as the thin film deposition methods however, the combined TDS and QCM technique is limited by the destructive phase transition of quartz at 847 K mentioned above. Higher desorption temperatures are therefore not reachable without loosing the Δm information from the resonators.

3.1.4 Experimental chambers

All experiments were carried out under Ultra High Vacuum conditions ($p < 1 \times 10^{-9}$ mbar). Two separate vacuum systems were used, both build up around a QCM sample holder as their central piece. It is placed on a $xyz\phi$-manipulator together with a Faraday Cup (FC), both mounted in separated compartments along the z-axis. This setup allows for a switching of the irradiated compartment, measuring current densities over an extended area (typically as a cross around the zero position) and irradiations under different angles of incidence α. Furthermore, QCM sample holders are equipped with ohmic heaters, allowing to perform experiments at elevated temperatures. Thermocouple sensors are placed on the sample holders as well, allowing to log the temperature during such heated temperature dependent. The chamber based around the SOPHIE ion source (see section 3.1.5) additionally hosts four several other components:

- A third compartment for holding pressed mineral samples – also equipped with an ohmic heater
- A *Pfeiffer Vacuum QME 220 Quadrupole Mass Analyzer* (QMA) used to determine residual gas pressures in the experimental chamber
- A *PREVAC Flood Source FS 40A1* electron source necessary for charge compensation on insulating bulk materials
- A C-QCM mounted coaxially for measuring sputter yields of bulk samples

With theses extensions, a broader spectrum of measurements is possible, including TDS, measuring angular distributions of sputtered particles and sputter yields of insulating mineral pellets.

3.1.5 Ion beam setups

The two vacuum systems used during this thesis rely on different ion sources. The first one was based on the in-house build Electron Cyclotron Resonance (ECR) ion source nicknamed *SOPHIE* [91], the second one on a commercially available electron impact ionization ion source *SPECS IQE 12/38* . Key differences are the production mechanism of the ions, according achievable ion charge states and the paths from the extraction to the experimental chamber.

SOPHIE

In the ECR ion source SOPHIE at TU Wien, working gas is ionized via microwave radiation, while ions are trapped in a magnetic bottle. For those purposes, several magnets are arranged, allowing the excitation of cyclotron motion of the electrons and storage of the produced ions. This way, the setup is capable of producing ions with different charge states, as the ions time in the source is increased, making multiple ionization processes more likely. After the ions extraction, the beam is shaped via a set of quadrupole magnets. Afterwards, the ions enter a sector magnet, steering ions with desired mass over charge ratio towards the direction of the experimental chamber. This selection is an important asset, since the ion source itself is able to generate various charge states. Additionally, impurities in the working gas are removed from the resulting ion beam. In the last section of the ion path, electrostatic lenses and deflection plates are used for guiding of the beam through sets of apertures. A separate pair of plates is also used to switch off the ion beam without moving parts which is useful for measurements sensitive

to vibrations like those with a QCM.
With the apertures and pumps in the beam path, significant pressure gradients from the ion source ($p \approx 1 \times 10^{-5}$ mbar) to the experimental chamber ($p \approx 1 \times 10^{-9}$ mbar), even for the light He working gas can be achieved. The reachable ion current densities for sputtering experiments, including a scanning of the beam over a sample area of some 10 mm^2 depend on the ion species. For 2 keV Ar^+, in the order of $10^{15}\ {}^{\mathrm{ions}}/_{\mathrm{m}^2\times\mathrm{s}}$ can be utilized. For 4 keV He^+, this number increased by an order of magnitude to $10^{16}\ {}^{\mathrm{ions}}/_{\mathrm{m}^2\times\mathrm{s}}$. This number again increased to up to $10^{17}\ {}^{\mathrm{H}_2}/_{\mathrm{m}^2\times\mathrm{s}}$ for 2 keV $\mathrm{H_2}^+$.

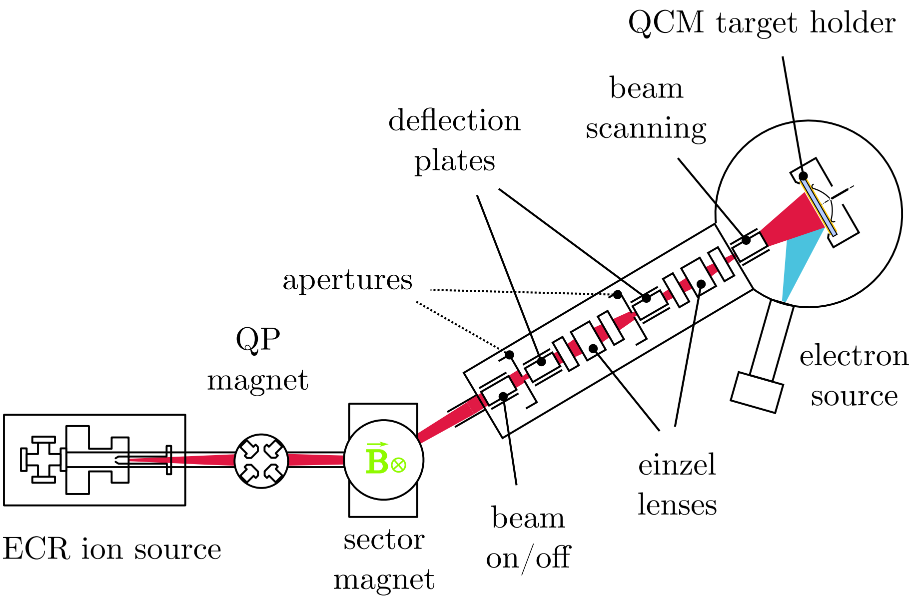

Figure 3.5: Path of the ion beam in the SOPHIE [91] based setup. A combination of magnetic and electrostatic deflection options allows for precise measurements with high fluxes and minimal pressure increase at the experiment while running the ion source. Additionally, clean ion beams due to ${}^{m}/_{q}$ separation in the sector magnet. The electron source is lifted $45^{c}irc$ and used to prevent a charging of insulating samples. Figure taken with adaptations form [92] and [93].

SPECS IQE 12/38

The setup based on the ion source *SPECS IQE 12/38* not only has a different mechanism of ion production – working gas is ionized via impacts of electrons accelerated in an electric field – but also a vastly different path of the ions in the vacuum system. Selection of the ion species and the charge state respectively, is achieved via a Wien velocity filter. Apart from that, beam shaping and guiding towards the samples is solely done via electrostatic lenses and deflection plates. This leads to a very compact setup (shown in figure 3.6), which comes at the cost of an about an order of magnitude higher working gas pressure in the experimental chamber compared to the SOPHIE based system. When allowing these increased pressures, similar fluxes can be reached for singly charged ions.

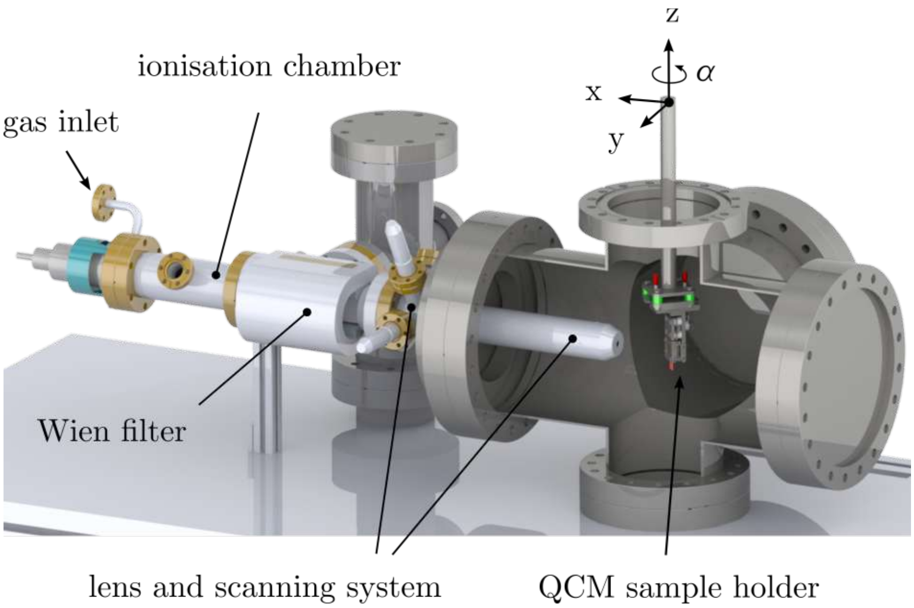

Figure 3.6: 3D-CAD drawing of the SPECS 12/38 based sputtering setup used for parts of this thesis. The compact setup comes at the downside of elevated background pressures in the experimental chamber when high ion currents are used. Image adapted from [94].

3.2 Samples

The studies conducted during this thesis were concentrated on the interaction of ions originating from the sun with the surfaces of bodies in outer space. It was therefore necessary to have samples which resemble such systems as closely as possible. For the Moon, several missions from NASA were landing between 1969 and 1972 during the Apollo program [95]. Those were manned missions, where astronauts took samples of the lunar surface with them on their way back to Earth. This allows for studies with actual lunar material. The *Appollo-16* mission returned to Earth with 95.7 kg of samples on April 27, 1972 [96]. During this thesis, it was possible to work with one of those samples, namely the sample with the number *68501*[1].

For the planet Mercury, however, no landing of a spacecraft has been performed so far. Therefore, no on-site crystallography measurements or even returned samples are available. In order to still investigate space weathering on Mercury, analog material has to be used instead. During this thesis, three such analog minerals – all of them pyroxen(oid)e silicates – have been used, giving a broader overview on the interaction of solar wind ions with Mercury:

- Wollastonite ($CaSiO_3$) was used due to its negligible Fe content and the available literature regarding sputter yields.
- Enstatite ($MgSiO_3$) serves as analog for Mercury, where up to 16 wt% Mg are present in Magnesium rich terrains [26].
- Augite $(Ca,Mg,Fe)_2[Si_2O_6]$ was used to gain information about the interaction of solar wind with less idealized silicate systems.

The materials used for the studies had to be prepared in order to perform actual measurements. As highlighted in section 3.1, the sample material had to be deposited onto quartz resonators to make use of the classical QCM technique. In addition, powdered minerals in the form of pressed pellets were needed for studies of possible influences of crystal structure and surface roughness on the sputtering behavior using the new C-QCM method.

3.2.1 Sample fabrication

In general, two different types of samples were investigated during this thesis. Amorphous thin films deposited onto QCMs allow direct measurements of sample mass changes during ion beam experiments, making them an ideal tool for studies on total sputtering and implantation during ion irradiations. This however comes at the cost of often challenging preparation of those samples. Due to the before mentioned phase transition of quartz at 847 K [73, 81], deposition techniques are limited and parameters like crystal structure or surface roughness can only be controlled in a limited manner. The QCM technique is therefore mostly used with flat, amorphous thin films, when planetary analogs are investigated [29, 30, 76, 80]. To study the influence of the parameters hardly accessible with QCMs, bulk samples had to be irradiated as well. Those also had to fulfill certain criteria, like the stability to withstand the installation in a vacuum system, a defined shape and fitting in the sample holder compartment at the correct position.

---

[1] `https://curator.jsc.nasa.gov/lunar/lsc/68501.pdf`

Thin films on microbalances

Layers from the mineral samples have been deposited onto the quartz resonators via Pulsed Laser Deposition (PLD) by Andreas Nenning from the Institute of Chemical Technologies and Analytics at the TU Wien. For this purpose, donor pieces were installed into a vacuum chamber and irradiated with a *Lambda Koherent Pro* pulsed 248 nm KrF excimer laser. Depositions were performed under an O_2 background pressure of 0.04 mbar for times of 30 - 60 minutes at pulse frequencies of 5 - 10 Hz. The elevated background pressure was necessary to reproduce the original stoichiometry. The resonators were heated to 300 °C during the deposition phase. This method allows the production of flat thin films of several 10 to 100 nm on the QCMs, based on the mineral samples.

Pressed mineral pellets

The naturally grown minerals mostly consisted of single crystals, which can have a known impact on the sputter yield for certain orientations of the ion beam due to channeling and also lead to particular emission of sputtered material (see chapter 2). This effect was not of interest, as it is not a realistic scenario for planetary bodies. Here, material is randomly distributed across the surface, resembling a polycrystalline sample at best. This more realistic scenario for a planetary body was to be investigated. In order to achieve this, pressed powdered mineral pellets were used.
Production of the mineral pellets used for experiments in this thesis were performed by our project partner N. Jäggi from the University of Bern. A short overview is given in the following, detailed information can be found in [82]. Mineral pieces selected by their composition and therefore level of contamination were chosen according to literature about Mercury's expected mineralogy. This way, samples with a high relevance for the planet Mercury could be selected. For achieving polycrystalline pellets, the available single crystals first had to be powdered in an agate disk mill. This resulted in material with grain sizes mainly below 100 μm. The resulting polycrystalline powder was subsequently pressed into stainless steel holders with 80 MPa at a diameter of 10 mm. Depending on the level of adhesion between the powder and the stainless-steel holder, an inter-layer (wollastonite $CaSiO_3$ or KBr) had to be used. This layer was completely covered by at least several tens of micrometers of powder and did therefore not influence the sputtering investigations, with penetration depths of the used ions far below the micrometer range.

3.2.2 Sample characterization

To guarantee samples with well defined properties, analysis had to be carried out in addition to the actual measurements. This was especially important, as thin films were produced for the irradiations, making their analysis with respect to stoichiometry crucial. Furthermore, the extrinsic property of surface roughness was expected to alter the sputter measurements and therefore also had to be characterized in detail.

Sample composition

One of the key properties of a sample for sputtering investigations is their composition. Sputter yields very much depend on the material and can span orders of magnitude for the same impinging ion species. For example, literature values for irradiations with 2 keV Ar^+ ions under normal incidence are about 25 $^{amu}/_{ion}$ for Si, while the value for Au is about 400 $^{amu}/_{ion}$. It is therefore important to have a well quantified sample stoichiometry. This also allows to understand, how sensitive the sputtering data is to variations in composition. With the variety of minerals that were used for measurements during this thesis, a suitable technique for this characterization was needed. Due to the deposition process, bringing material from the minerals onto microbalances as thin films, this was even more important. Especially for multi-component targets, stoichiometries completely different from the donor minerals can arise, depending on the precise deposition parameters like the O_2 background pressure in PLD [97]. Ion Beam Analysis (IBA) techniques like Rutherford Backscattering Spectrometry (RBS) [98, 99] and Time-of-Flight-Energy Elastic Recoil Detection Analysis (ToF-E ERDA) [100] are ideal tools for this purpose.

In RBS, light ions like He with energies in the MeV range are impinging on the sample. A detector is placed close to the incidence direction of the ion beam, detecting ions reflected backwards from the sampe. Due to the known geometry, a unique relation between the mass of the collision partner and the ions' energy after scattering is given. Due to the energy loss from the ions penetrating in the sample, this leads to an energy with a width proportional to the sample thickness. With known interaction cross-sections, sample thickness in $^{atoms}/_{cm^2}$ and composition can be evaluated quantitatively.

ToF-E ERDA also works with MeV ion energies. In contrast to RBS, heavy ions like $^{127}I^{8+}$ are used and recoils from collision events are detected in forward direction. Its strength lies in the detection of light elements in heavy matrices, where RBS does not perform well due to an overlap of the signals in the energy spectrum.

A combination of both measurements was performed by M. Moro at Uppsala University. RBS results with 2 MeV He^+ ions were used for estimating the thickness of the thin films, while ToF-E ERDA data obtained with 6 MeV $^{127}I^{8+}$ ions were interpreted for the corresponding composition as described in [101].

In addition to the uncertainty of the thin film composition, only limited information about the Apollo 16 sample composition was available in the first place.

Only chemical analysis of parts of the sample were available in [102–104] and the representativeness for this study was questionable. Therefore, an IBA study was performed for the pressed mineral pellets of the Apollo 16 mission as well.

Surface topography

The sputtering process is very much dependent on surface topography of the investigated sample (see section 2.1). It is therefore crucial to characterize them with regard to surface roughness. In similarity to the Coastline paradox [105], quantification of roughness is not only depending on the actual surface, but can drastically vary when investigated at different scales. It is therefore important to perform the characterization at a range adequate for the physical process influenced by roughness. Sputtering takes place at the atomic scale, therefore also the probing of the surface has to be performed at that level. Cupak *et al.* showed, that AFM samples the surface topography at the correct level to estimate the changes to the sputter yield caused by roughness effects.

The topography data was taken with an *Asylum research Cypher AFM*, operating in *non-contact AC* mode. Thereby, an AFM tip (actually the cantilever) is excited close to it's resonance frequency while scanning in short distance above the surface. Changes in resonance frequency due to the interaction of the tip with the surface can be observed via deflection of a laser shining on the cantilever. This way, both types of samples - thin films on quartz resonators and pressed mineral pellets - were characterized. Due to the wide range of roughness, scanning parameters (mainly the speed of the tip) had to be changed drastically between the samples in order to actually acquire topography data. With the high elevations of several 100 nm and local surface angles steeper than 60°, tip velocity was a key parameter. Typical numbers were 2.42 - 5.0 $^{\mu m}/_{s}$ for the rougher mineral pellets. For high resolution images of 4096 scanning lines and 4096 points per line at an area of 20 µm × 20 µm, taking one image required about 23.5 hours for the slow scanning. The limits of resolution and scanning area regarding usable scanning times were fully utilized in order to get detailed information about the local surface angles as well as a representative excerpt of surface information.
A possible problem when probing surfaces with an AFM are measurement artifacts caused by the shape of the tip. Due to its physical dimensions, the interaction with the sample can take place locally at different points on the tip. One of the consequences of this fact is, that the obtained elevation data is the convolution of the surface and the tip [106, 107]. Therefore, local slopes steeper than the angle of the tip side itself cannot be measured. This particular fact can be seen when looking at the distributions of local surface inclination angles, which are used for estimating the impact of surface roughness on sputtering. Here, all slopes with

angles above the tip limiting angle are integrated into a peak at that position. Figure 3.7 gives an example of such a feature, observed at an enstatite pellet used for the study discussed in chapter 5. Due to the significant surface roughness of this sample, such an artifact can be seen in the gray shaded area from about 52 to 74°.

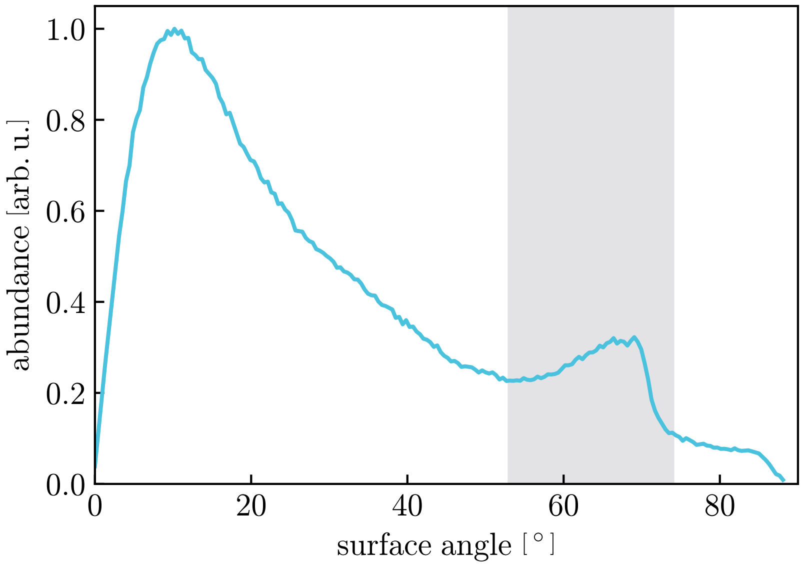

Figure 3.7: Distribution of the local surface inclination angle of an enstatite pellet as measured with the AFM and a *OPUSTIPS 240AC-NA* tip. An additional peak between 52° and 74° can be seen (highlighted in grey), which is probably caused by the convolution of steeper edges and the tip geometry.

In that particular study, *OPUSTIPS 240AC-NA*[2] tips were used, with tip angles of 0° at the front, 35° at the back and $< 9°$ at the side and a tip radius below 7 nm according to the manufacturer. Therefore, the limiting angle for surface slopes depends on the orientation of the sample in the AFM. For the measurements of the surface topography of the pellets pressed from the lunar sample, a tip with different geometry was used instead. The *SSS-FM*[3] tips from *NANOSENSORS* feature a half cone angle of $< 7°$ and a guaranteed tip radius of less than 5 nm. Flattening of the particularly steep surface features was therefore less of a concern with those tips, with AFM images showing no tip artifact.

---

[2] `https://www.opustips.com/en/AFM-Tip-240AC-NA.html`

[3] `https://www.nanosensors.com/supersharpsilicon-force-modulation-mode-afm-tip-SSS-FM`

3.3 Measurement procedures

The following section describes the methodology for the experiments performed at TU Wien during this thesis. The following recipes were developed in order to obtain reliable and reproducible results.

3.3.1 Preparation

After being installed into the vacuum system, all surfaces are initially covered with contaminations. Due to the use of suitable ion sources in the experiments, sputter cleaning of the samples - typically with 2 keV Ar^+ ions - is readily available. Primary samples were mostly cleaned under an angle of incidence of $\alpha = 60°$, where the ion energy is deposited closer to the surface as for normal incidence. For the C-QCM however, cleaning under grazing angles was not possible due to the positioning of the catcher on its sample holder. With the of distance of $r_C = 17\,\mathrm{mm}$ from the axis of rotation, the sample is moved out of the ion beam too far for a safe relocation towards the irradiation center when rotated to $\alpha_C = 60°$. However, as its rotation is not limited in the chamber, it can be set behind the primary sample holder with respect to the ion beam direction. It then faces the ion beam, which can be used for cleaning under normal incidence ($\alpha_C = 0°$). The primary sample holder itself has to be rotated to $\alpha = 90°$ and moved out of the beam by 9 mm in y-direction (perpendicular to both the ion beam and the sample holder axes). This is necessary for the ions to pass the primary holder and for the guiding rod to pass next to the sleeve. Due to the differences in sputter yield of the samples and surface adsorbates, the cleaning process of the QCMs can directly be monitored in real time. Therefore, clean samples can be guaranteed in that case, simply by observing the sputter yield until a steady condition is reached. Figure 3.8 shows the signal of a QCM during cleaning with 2 keV Ar^+ ions at $\alpha = 60°$. The transition from dynamic changes due to the cleaning to a steady state in sputtering with a constant slope can seen after about 3000 s. This is however not possible for the pressed mineral pellets, which were used as well. Here, no direct information of the sputter process is accessible. Therefore, the QCM was cleaned first and the fluence needed for their cleaning was taken as reference value for the pellet. A similar fluence was then used for the pellet cleaning as well, with the addition of some fluence to account for uncertainties.

The cleaning with Ar ions not only removes adsorbates from the surface, but also leads to modification of the first material layers due to the displacement of atoms in the ions range. This effect has to be considered, when discussing the effects of material phases on sputtering. To circumvent the need for sputter cleaning with 2 keV Ar ions, irradiations with smaller kinetic energies of 400 eV were tested as well, but here ion currents were insufficient for cleaning in reasonable time spans.

Instead, a completely different method was implemented, circumventing the need for sputter cleaning with Ar ions at all. It makes use of the *PREVAC Flood Source FS 40A1* electron source and the sample heater. In this scenario, samples are heated to about 300 °C for several hours while simultaneously irradiating the samples with electrons with a kinetic energy of 20 eV.

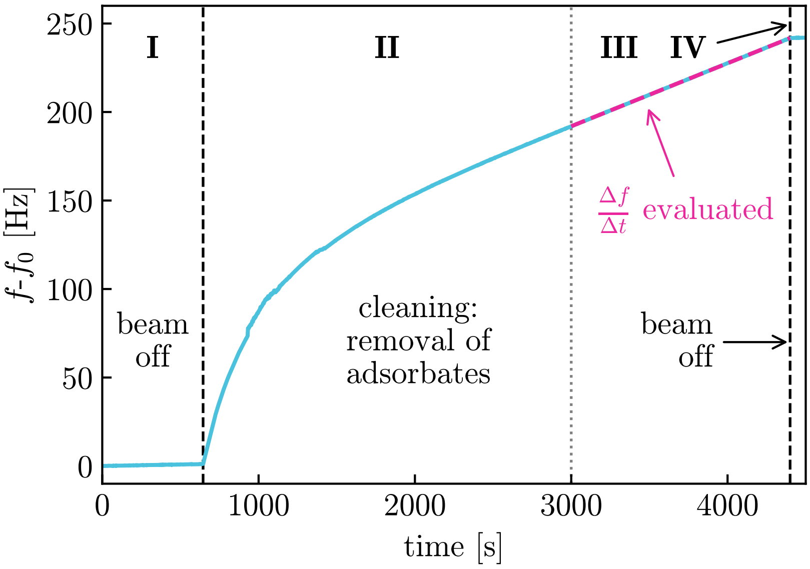

Figure 3.8: Example of the QCM signal during the cleaning of an augite ($(\mathrm{Ca,Mg,Fe})_2[\mathrm{Si}_2\mathrm{O}_6]$) film with 2 keV Ar^+ ions at $\alpha = 60°$. Phases without ion beam (**I**,**IV**), increased frequency changes due to sputtering of adsorbates (**II**) and a steady state conditioning (**III**) can be seen.

3.3.2 Direct measurements of mass changes

A typical measurement of sputter yields using a QCM can be separated into two phases. At first, dynamic effects can be observed, which are at least to some extent present in every measurement. The origins for those are plentiful. Dynamic behavior in the sputter yield - and consequently in the rate of frequency change - discussed in section 2.1 can be one explanation. In addition, implantation of the impinging ions oftentimes leads to a variation in mass change per impinging ion as well, which eventually reaches a steady state when implantation and release of the impactors are balanced. As discussed in the beginning of this chapter however, actual mass changes caused by the ion beam are not the only cause for the observed variation in ${}^{\Delta f}/_{\Delta t}$. The QCM exhibits a very pronounced temperature dependence of the resonance frequency. Therefore, heating due to the additional power dissipation of the ion beam also causes an observable change in resonance frequency. All those effects combined can lead to complex variations of f_Q over the period of an irradiation as was shown in figure 3.1. Simply applying equation 3.3 to the obtained frequency data is therefore not valid. Instead, each section has to be treated separately when the irradiation dynamics are of interest. When sputter yields are discussed in this thesis, steady state values of ${}^{\Delta f}/_{\Delta t}$ are used for evaluation, if not stated otherwise.

Another crucial dependency of ${}^{\Delta f}/_{\Delta t}$ is its radial sensitivity to mass changes. The quartz resonators used for sputter yield measurements have a radially decreasing, Gaussian sensitivity profile, discussed in detail in section 3.1.1. This means, that the response of the resonance frequency deviates locally from Sauerbrey's equation (equation 3.1) [70]. The linear relation between Δm and Δf becomes valid only for homogeneous changes of the mass over the whole active area of the resonator. The resulting slope results from an integration of the sensitivity function over the irradiated area. For non-homogeneous conditions, the product of mass change and sensitivity would have to be integrated for an evaluation. It is therefore crucial for accurate measurements to irradiate a sufficient area around the quartz center. This is achieved by applying sufficient voltages to the scanning plates (see section 3.1.5), leading to a homogeneous current density when integrated over time. The sensitivity of the resonator was already shown in figure 3.4, where no significant sensitivity for points further away from the center than 3.5 mm can be seen anymore. The scanning of the ion beam was therefore typically adjusted to have a full width of about 7 mm for sputter yield measurements with QCMs. It has to be noted, that an increase would not lead to a different result in sputter yield measurements, but to a smaller ion current density j, resulting in longer irradiation times to reach certain fluences and possibly larger uncertainties.

3.3.3 Measurements with the Quartz Crystal Microbalance as catcher

Two different approaches were used for calculation of pellet sputter yields from C-QCM data measurements. Both cases were started with cleaning procedures as described above. Due to the finite pressure in the experimental chamber, all surfaces become contaminated with residual gas as soon as the cleaning stops. In fact, this is also true during the cleaning itself, so sputter rates need to be significantly higher than deposition rates by residual gas. To minimize possible effects of a contamination layer formed after the cleaning on the catcher signals, the C-QCM was always cleaned at last, while the primary QCM was typically the first sample, in order to quantify the fluence needed for the pellet as it is described above. The two methods for C-QCM measurements differ from that point on.

Sequence with virgin catcher surface

In the first scenario, the ion beam was adjusted with the scanning plates to the size used for irradiation conditions directly after all the surfaces were cleaned. Then, the C-QCM was moved up to the ion beam, including an insertion of the rod. From that point on, only rotations of both sample holders and a change between the pellet and the QCM as irradiated sample was possible. Data recording of the data started immediately afterwards. Due to variations in electron current in the first hour, the electron flood source was turned on, but irradiations started just after waiting for about one hour. This was also necessary due to a variation in C-QCM temperature correlated to the instabilities in the electron emission. In the following irradiations, both the catcher angle β (see figure 3.2) and the type of sample were varied, while keeping the incidence angle of the ions α constant. When the irradiations with the ion beam started, the total signals $Y_{C,\Omega}$, were unreliable, oftentimes increasing by 50% at the same position when other β values or the other sample were measured in-between. This method however still delivered constant ratios of ${}^{Y_{C(Pellet)}}/{}_{Y_{C(QCM)}}$ when comparing irradiations of the pellet and the primary QCM samples (see section 5) performed directly after each other. To guarantee that no change in signal occurred in-between, always three measurements were used for evaluation. The samples were exchanged back and forth at the same angle β and only those measurements were taken, where the first and the last measurement (i.e. with the same sample) gave equal signals.

While changes of the measurement geometry caused by movement of the manipulators could be ruled out as reason for the unstable signals, variations of the sticking probability were found to be the cause. Therefore, another preparation step was introduced after the cleaning process. The C-QCM was coated with material from the pellet already before the acquisition of the actual ${}^{\Delta f}/{}_{\Delta t}$ data for $Y_{C,\Omega}$ evaluation started. Just irradiating the pellet without obtaining deposition rates at the Q-QCM however has the disadvantage, that the samples already accumulate ion fluence, leading to damages and loss of crystal structure. Possible changes in the sputter behavior during such a process are then not observable.

Sequence with precoating-procedure

A solution to overcome this problem is by irradiating a different spot for this so-called *precoating-procedure*, than for the actual measurements. With the pellet diameter of 10 mm and the square beam profile (see section 3.1.5), only parts of the pellet are actually irradiated with the ion beam. Additionally, the beam profile size of 7.0 mm × 7.0 mm as it is used for the primary QCM measurements cannot be applied for pellet irradiations. Under angles of incidence $\neq 0°$, the projected area of the ion beam on the sample is increased. This is not a big concern for classical

QCM measurements, as hitting parts outside the sensitive area do not contribute to signals. Therefore the only effect is a signal $^{Deltaf}/_{\Delta t}$ smaller than possible due to the not contributing ions. For catcher measurements however, ions hitting outside the desired area can significantly alter measurement results. Not only is the ion current impinging on the sample different from the measured current, but also in addition sputtering of sample holder occurs. As all sputtered material deposited on the C-QCM contributes to the signal, this must be avoided. Scanning is therefore reduced to an area about 4 mm × 4 mm (under normal incidence), hitting 8 mm × 4 mm under an angle of incidence of $\alpha = 60°$. This means, that there is some area left above and below (along the axis of rotation) which is not used during the sputter yield measurements. An irradiation limited to this area can be used for this precoating procedure - therefore called *Pellet Edge Pre-Coating* (PEPC). For PEPC, the ion beam was not scanned, and had a diameter of about 1 mm. The angle of incidence was $\alpha = 45°$ to minimize the risk of hitting the sample holder. To achieve a coating of the C-QCM, it was placed at a position with high deposition rate, $\beta = 25°$. Ion beam parameters like energy and species were the same as for the according measurement. Just as the sputter cleaning process, PEPC was stopped, when $^{\Delta f}/_{\Delta t}$ was constant. After PEPC, measurements were started just as in the first scenario. However, no more changes in $Y_{C,\Omega}$ after movement of the sample holders were present, resulting in robust results.

Before and after each series of measurements, the ion beam was characterized. In contrast to the classical QCM technique, the total ion current I rather than the ion current density j determines the signal at the C-QCM (see section 3.1.2). Still, j is an important quantity as changes of the sample are caused by a certain fluence (accumulated number of ions per area), which is directly proportional to $j \times t$. The latter can be determined from the current in the FC (see section 3.1.5), when the current is constant for an area larger than the FC size. For determination of I, this density has to be scaled with the actual size of the ion beam A_{beam}. Due to the size of the FC aperture of 0.6 mm^2 and a resulting diameter of about 0.9 mm, a significant uncertainty of A_{beam} arises. This is especially of concern for the reduced beam size used for C-QCM measurements. For quantitative determination of $Y_{C,\Omega}$, this problem needed to be addressed. Therefore, two measurements of the ion beam profile were carried out, both with the same ion beam entering the chamber, but scanned with different amplitude. This keeps the total ion current I, constant, but changes the ratio of A_{beam} and j. First, the ion beam was scanned over a wider area of about 9 mm × 9 mm, which allowed a much preciser determination of A_{beam}, while still having sufficient ion current in the FC to determine j_{wide} precisely. The scanning was then reduced to irradiation conditions, where j was determined for the calculation of the fluence.

The measurements were also constrained with respect to measurement geometry.

Since the positioning of the C-QCM is limited in backward direction by the blocking of the ion beam for positions closer than $\alpha + \beta = 35°$ to the ion beam as discussed in section 3.1.2 (see fig 3.2 there), the meaningful range for the angle of incidence α was also limited. The angles $\alpha = 45°$ and $\alpha = 60°$ are often used in sputtering experiments. At 45°, already an increase in sputter yield compared to the normal incidence value is observed for flat samples on silicate minerals [29,30]. It is also a favorable angle to investigate rough surfaces, as here the sputter yield is not effected much by surface roughness [39–42]. In addition, some signal in backward direction can already be obtained with a possible value of $\beta = -10°$ in this case (considering the minimum angle of 35° between C-QCM and the ion beam). An angle of $\alpha = 60°$ however is often close to the limit allowed by sample holder designs and edges of sample apertures are also exposed to ions for more grazing incidence angles. Furthermore, it is an angle close to the maximum of the sputter yield dependency on α and one where the sputter yield is strongly influenced by surface roughness. Therefore, those angles were used for all measurements with the catcher system.

Irradiation times varied for ion species, sample type and previously applied fluence. In general, they were kept as short as possible to achieve stable results. This was especially crucial for the primary QCM. Here, wear of the thin film is of big concern, with thin film thicknesses of some tens to at max a few hundreds of nanometers. An exception from that rule were however measurements with pellet samples, which were already in the regime of saturation of ion induced damages. Here, longer fluences could be applied, observing long term trends and reducing the risk of overseeing long-term changes in the measurement signals. One issue observed for measurements with 4 keV He^+ ions were transient effects in the first few 100 s of measurement time, only observed when irradiating the primary QCM sample and with the C-QCM positioned in forward direction. Longer measurement times were therefore needed to reach a stable signal for data acquisition (e.g., without any temperature influence, a few hundred seconds would already be enough to achieve reliable results). This effect also leads to increased scatter in the obtained signals, as irradiation times were still kept low because the fluence applied to the primary QCM had to be kept as small as possible. The transient effects are attributed to a heating of the C-QCM by impingement of ions reflected at the irradiated sample. This is the same temperature related frequency change as discussed above for the directly irradiated QCM samples (Figure 3.1). Figure 3.9 shows this transient effects in the beginning and after the end of the irradiations at a C-QCM under 4 keV He^+ bombardment at $\alpha = \beta = 60°$.

Due to the motorization of the primary sample holder and the rotary manipulator of the C-QCM, fully automated irradiation sequences were possible. The first allowed a variation of sample type (QCM or pellet) and angle of incidence α

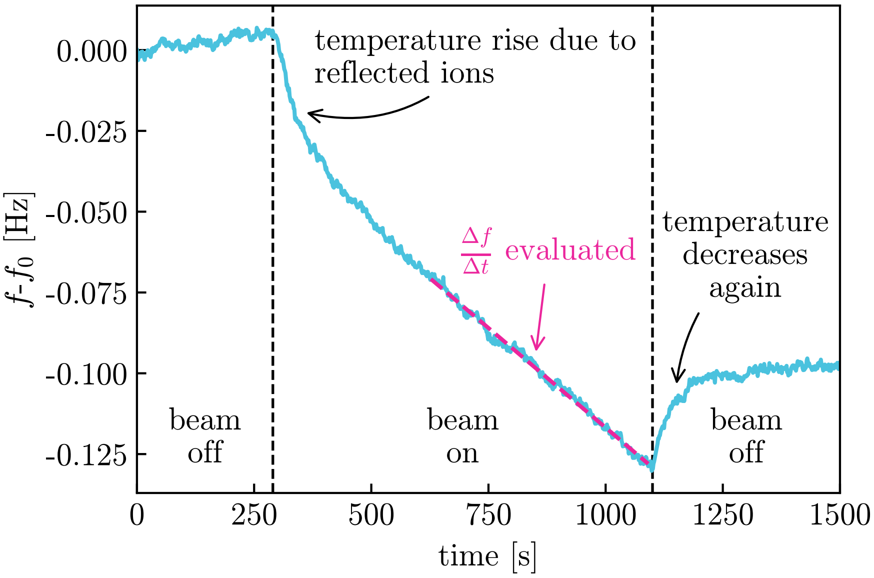

Figure 3.9: Signal of the catcher during irradiation of a QCM sample with 4 keV He^+ at $\alpha = \beta = 60°$. Just as for the primary sample, changes of the resonance frequency due to heating of the QCM can be seen after turning on/off the ion beam, caused by reflected ions hitting the catcher.

(either 45° or 60°), while the second varied β between $-25°$ and 90°. Changes of ion beam shape or measurements of ion currents were however not possible between measurement sequences. Several variants of sequences could be tested by simple modification of computer scripts. This was necessary to find optimal sequences, check for consistency between measurement cycles and to get robust results with both methods used for catcher preparation.

3.4 Simulation Efforts

At the time writing of this thesis, theoretical calculations of sputter yields are commonly done by means of simulations rather than by analytical formulas. The calculation power of modern computer systems is sufficient to simulate the interaction of ions with solids and extract sputter yields within a few minutes on conventional desktop or mobile computers. This happens with Monte Carlo (MC) codes based on the so called Binary Collision Approximation (BCA). Hereby, ions are treated as neutral particles, impinging on an amorphous target. When a constituent of the target is hit, a collision cascade is set in place, where each partner is tracked and treated independently. Collisions are therefore only calculated between two partners, hence the name BCA. Typically, BCA codes are Monte Carlo (MC) codes, where parameters of the underlying process are chosen randomly, for instance the impact parameter or the azimuth angle of the particles after collision. Another way of simulating ion-solid interaction is with programs based on Molecular Dynamics (MD), which can also be used to calculate sputtering [108]. In short, Newtons equations of motion are thereby solved for particles in the target and the impinging ion. Time is discretized and the state of every particle is evaluated at steps in time. With correctly defined interaction potentials, MD is a very powerful tool but due to the complexity of the system it requires cluster infrastructure for calculations [109]. The consequences are a small number of particles in the sample (*simulation cell*) and long computation times for good statistics. Together with the often challenging choice of interaction potential, this is one of the major downsides of MD, which therefore does not allow studying of large structures, although in principle not being limited to flat samples [110, 111]. During this thesis, only BCA codes were used to accompany experimental results. Instead of the most commonly used code at the time writing – SRIM – SDTrimSP was used for this purpose. This is due to the incapability to describe sputter yields correctly and the inflexibility with regard of input parameters of SRIM (see chapter 2).

3.4.1 SDTrimSP

There are several BCA codes available, each of them having their own advantages and disadvantages. SDTrimSP [65] (based on the **S**tatic **TRIM.SP** [112] and the

Dynamic TRIDYN [113], hence the name) is known to deliver good agreement with experiments when it comes to the sputter yield and its angular dependence. It furthermore offers the user a wide range of input parameters, beginning with the choice between various interaction potentials or integration methods. Also more sophisticated tweaks are possible, as for example the use of different surface binding models (a more detailed discussion on this topic is found in 2). Those facts alone make SDTrimSP a much more suited tool for simulation studies on sputtering than the often used SRIM code. In SDTrimSP, the target is made up of layers of constant composition. The material properties are calculated for those layers separately according to tables included in the program, but they can also be manually overwritten with separate input files. Besides the depth information, the sample itself does not possess any structure, which makes the program a *1D code*. The trajectories in the sample are however still calculated in all three dimensions. When a projectile is hitting the sample, it is tracked together with all generations of recoils, as long as their kinetic energy is above a defined cutoff value E_{cutoff}. Just as the other parameters, this value can either come from a table or be set manually by the user. When only sputtering is of interest and a surface binding energy model is used, E_{cutoff} can be set equal to the smallest surface binding energy of the sample components: $E_{cutoff} = min\,(E_{SB})$. Particles with smaller energy get reflected at the surface anyways and are therefore not contributing to the sputtering process. This is valid due to the nature of the BCA approach, where no transfer of momentum from one moving particle to the others is possible and all recoils are treated independently. The program allows the output of various data generated from the performed simulations. Besides the scalar values like sputter yields and reflection coefficient, also trajectories, energy- and angular distributions of sputtered particles can be extracted.

In addition, SDTrimSP features a dynamic mode, where changes in sample composition can be taken into account. Such can be caused for example by preferential sputtering, the implantation of ions into the sample or mixing of composition between different layers. Therefore, fluence dependent studies of exactly those processes become possible. These however often also require special treatment of the implanted ions, as the calculated implantation can lead to nonphysical accumulation of the ions at their range in the sample. This means, that some sort of limiting measure has to be considered, when increasing fluences are to be calculated. The most simple solution is a limitation of the allowed local projectile density. This is implemented in SDTrimSP, but has the disadvantage of assuming unphysical effects. Projectiles as far in the solid as the ions penetration depth (e.g. some 10 nm for 4 keV He on $MgSiO_3$) are disregarded without any measure of transport out of the sample as soon as a certain local projectile density is reached. Nevertheless, this method can be able to reproduce experimental results to some degree [76]. More sophisticated concepts implemented in SDTrimSP consider actual transport of the projectile in the sample. During this thesis, *Damage-driven diffusion* and *Pressure-driven transport* models were used, which allow a transport of implanted projectiles due to damages caused by the impinging ions and concentration gradients in the sample. They are thereby transported toward the surface, leading to a removal of material in a physical way instead of an artificial removal from within the bulk. The downside is however, that adequate coefficients determining the amplitude of the diffusion process have to be found. A detailed description of the transport mechanisms and the dynamic mode of SDTrimSP can be found in [65].

In addition to the capabilities discussed above, one of the main advantages of SDTrimSP is its active support. The maintainer of the code, Andreas Mutzke is not only fixing bugs in the code if they appear, but is still implementing new features if they can help at solving a scientific question or improve accuracy of the simulations.

The results for all simulations presented in this thesis were performed with a specific set of parameters. Szabo *et. al* described adaptations to the inputs, which allowed for simulation results to match experimental observations of sputtering very well [30]. The main adaptation was to override the input for the surface binding energy of O used for calculation and to fix it to $E_{SB,O} = 6.5\,\mathrm{eV}$, while setting the input flag *isbv = 2*. This flag defines the model used for calculating the values of $E_{SB,i}$ actually used during the simulations for all constituents. In the used mode (*isbv = 2*), all components get the same value ($E_{SB,i}$=$E_{SB,j}$), calculated according to the input values and a weighting with their abundance. Furthermore, the density of the sample had to be adjusted. By default, SDTrimSP does not offer the option to adapt this value and only calculates a value from tabulated values of the constituents. This can however result in large deviations from the actual materials density. To overcome this issue, either the oxygen density was adapted in such a way, that the sample density was matched (used for dynamic simulations) or all densities were set equal to the desired final value (used in the static simulation mode). The latter is more straight forward to implement, but suppresses density variations caused by preferential sputtering and is therefore not recommended in dynamic simulations.

3.4.2 SDTrimSP-3D

For very fundamental sputtering investigations, perfectly flat samples are preferred due to the influence of surface roughness on the sputtering process discussed in detail in section 2.1. Oftentimes however, more realistic samples are to be analyzed or there are constraints in sample preparation, giving rise to roughened surfaces. This was also the case for the samples used for the studies presented in section 5

and 6. Here, the pressed mineral pellets could not be flattened after pressing, leaving them with a significant surface roughness. In such cases, it is desired to investigate or untangle the effect of this roughness on the sputtering process. Therefore, a 3D version of SDTrimSP is available – called SDTrimSP-3D, where whole topographies can be implemented [68]. Within that program, the target is made up from volume elements, so-called *voxels*, which are stacked to resemble the desired structures. This way, surface information from microscopy data like AFM [114] or computer generated inputs can be simulated [115]. In addition to the parameters which have to be taken care of in SDTrimSP, the size of these voxels is a new, essential parameter of SDTrimSP-3D. Smaller voxels are preferred in terms of accuracy, but require more computational resources. It has been found, that the size of the voxels should be smaller than the mean penetration depth of the ions in a flat sample of same material [68]. Furthermore, simulation cells have a finite size and the boundaries of those need to be considered. For AFM inputs, SDTrimSP-3D uses periodic boundary conditions, where particles leaving the cell on one side enter it again on the other side while preserving their momentum vector. This however also implies, that the structures on the surface are not continuous at the border, leading for example to saw-tooth structures when tilted planes are in the cell. The most simple solution is mirroring the input along the front and a side border. This way, the surface becomes continuous, but looses possible anisotropies (as for the example with the plane) and becomes four times bigger. Due to the increase of necessary computational resources, this effectively reduces the size of the usable input by 75%. Another way SDTrimSP-3D offers to minimize that problem is by tilting both the surface and the particle directions (for the ion beam as well as for the scattered/recoiled particles) by the mean angle of the surface plane. This can reduce the problem, but textures at the borders still lead to artifacts there. To address this further, an additional borderline can be generated, where the height values between both sides are interpolated. The use of this feature and the width of this zone can be chosen by the user. The biggest factor for minimizing the border artifacts is the choice of simulation cell size. It should be big compared to the elevations on the surface and therefore chosen as large as allowed by the constraints set by the computational resources.
Just as its 1D variant, the program is able to calculate dynamic changes of the sample. In addition to the effects mentioned above, also changes of the sample structures during ion beam irradiations can be studied. This has already been shown to deliver good agreement with experimental results in a reduced 2D-version of the program [57] and is the main benefit compared to the SPRAY code for sputtering of 3D structures discussed below.

Due to the requirement of big amounts of primary memory, cluster infrastructure is typically needed for calculations with SDTrimSP-3D. Oftentimes, however, such computational clusters set constraints on simulation times. Hence, simulations on the *Vienna Scientific Cluster* were very limited. Instead, a regular computer dedicated for this task was utilized.

3.4.3 SPRAY

Complex 3D-variants of BCA codes, building up whole pieces of material from volume elements is not the only way of simulating the effects of surface morphology on sputtering. As discussed in chapter 2, the influence of surface roughness can be reduced to geometrical effects - at least in a wide range of cases [39–42]. Therefore it is also possible to treat both, the sputtering of material by an ion species, and the changes in particle emission due to surface structures separately. The so-called SPRAY code [41] can be used for exactly that purpose. It is based on a ray-tracing algorithm, which is utilized for trajectories of particles instead of beams of light. With that technique, SPRAY combines sputtering information of flat surfaces and topography data in order to evaluate changes on sputter yield and emission profiles caused by the surface structures. In principle, sputtering information can be provided from any source, but it has to be grouped into two data sets. First, the angular dependence of the sputter yield for a flat sample of the given material is needed from close to 0 eV to the projectiles energy. It is used to evaluate the sputter yield for each impact point based on local surface angles. This happens for primary impacts as well as for reflected ions, hence the need for the information at lower energies. According to the second data set – the distributions of emitted particles for each of those local impact angles – material is released from the surface. Depending on whether those hit another wall or can escape, they contribute to the global sputter yield or not. By collecting also direction information of the sputtered particles, not only the scalar sputter yield, but also the emission characteristics are available as outputs.

Per design, SPRAY does not deal with the actual size of the objects – its results are scale independent. It is however important to keep in mind, that inputs have to be selected which have surface information at the correct resolution. In a study, Cupak *et. al* have compared AFM and Confocal Microscope data as inputs – a study only possible with SPRAY due to this scale independency [41]. They have shown, that AFM images – with their information in the nm regime – are well suited for this purpose, whereas the Confocal Microscopy inputs fail. Therefore, AFM images are used as inputs for SPRAY in the studies where considering surface roughness was important.

The main limitation of SPRAY lays in its solely static simulation mode. It does not compute changes on the target topography and can therefore only be applied if such changes do not need to be taken into account. For studies with high ion fluences or high sputter yield, such changes can be severe and completely alter sputtering processes over the course of an irradiation [44]. Here, BCA based 3D-codes like SDTrimSP-3D can fully show their potential and account also for the dynamics of the system.

4 Results I: Implantation of solar wind ions in minerals

The work presented in this chapter has partly been published in [76].

As protons (H^+) make up the vast majority of the solar wind, their interaction with minerals is of particular interest. A study by Zhu *et. al* has for example shown, that these protons can lead to the formation of water in silicate minerals [10]. Helium – as noble gas on the other – hand will not make chemical reactions with a mineral environment. The accumulation of high He concentrations could however alter the way planetary surfaces interact with their environment and lead to differently populated exospheres. However, so far only limited studies have been conducted on that topic by Lord and Futagami *et. al* [116, 117] and typically He saturated surfaces are assumed, e.g. at Mercury [118]. Both, the effects of erosion due to sputtering with solar wind ions and the implantation of He into analogue materials for the planet Mercury are investigated in detail in this chapter. Therefore, experimental results obtained with QCMs and dynamic simulations with the SDTrimSP code are compared, allowing a determination of sputter yields and the amount of He in an augite ($(Ca,Mg,Fe)_2[Si_2O_6]$) sample.

4.1 Sample preparation and properties

The base material for this study was *augite* ($(Ca,Mg,Fe)_2[Si_2O_6]$), an iron and magnesium rich pyroxene [119]. It was provided as a single piece of some cm^3 size by the collaboration partners from the University of Bern. In order to achieve thin films from this donor material, it was necessary to have two plane-parallel surfaces. Therefore, the mineral was cut and polished by R. Miletich-Pawliczek from the Institute of Mineralogy and Crystallography at the University of Vienna. Based on the resulting sample, thin films were deposited onto QCMs by Andreas Nenning from the Institute of Chemical Technologies and Analytics at the TU Wien as described in detail in chapter 3. The resulting thin films were analyzed with respect to their composition and thickness by means of IBA by M. Moro at Uppsala University (see also chapter 3 for a details). Silicon platelets were placed next to the QCMs during the deposition process for this subsequent analysis. Those have the same layer stoichiometry as the films on the QCMs and can be used as substitute in destructive analysis. ToF-E ERDA was used to determine the composition, which is extracted from a depth dependent profile, shown in figure 4.1 (note, that minor contaminations are omitted for better visibility of the main constituents in that figure). The resulting values for all elements including contaminations are listed in table 4.1. The RBS measurements used for quantification of the film thickness resulted in a total area density of 1270×10^{15} atoms/cm². Due to the high Mg content of 8.9 %, the density of enstatite ($Mg_2Si_2O_6$) of 3.3 g/cm³ [119] was assumed for calculating the layer thickness from this value. Based on that density, the thickness is estimated to 139 nm.

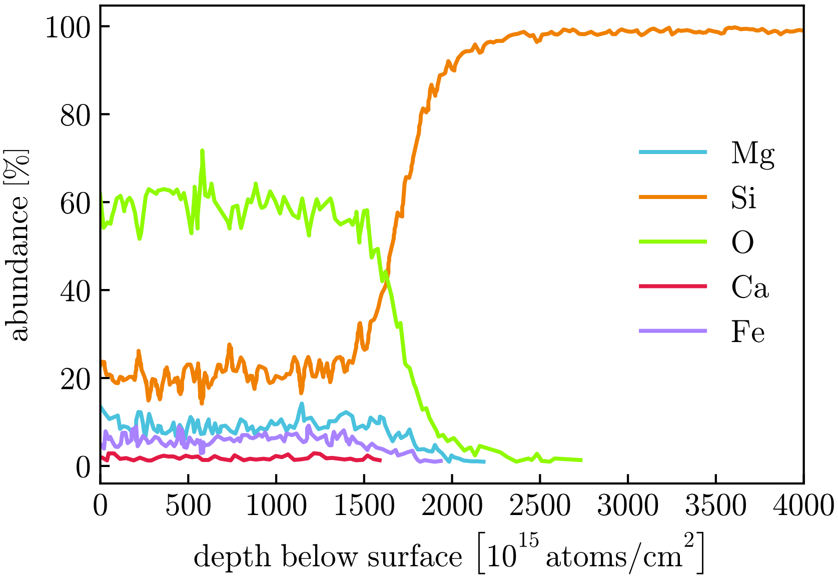

Figure 4.1: Depth dependent composition of the augite films according to ToF-E ERDA measurements performed by M. Moro. The layer was deposited on a Si platelet next to a QCM. Traces of H and C were omitted for better visibility of the main fractions but listed in table 4.1. At about 1300 at/cm², the O signal starts to decrease, indicating the end of the layer.

Since implantation as well as sputter yields were measured with the samples, investigations of the surface by means of AFM were necessary as well for estimating possible alterations in the signals due to surface roughness. Those revealed very smooth surfaces with a mean surface inclination angle of $\delta_m = 8.1° \pm 3.6°$. In this regime, the effect of surface roughness on the sputtering process is expected to be negligible [41]. Figure 4.2 shows the according surface inclination angle distribution evaluated from AFM images (left). A 3D visualization of a representative AFM image can be seen in figure 4.2 as well (right).

Table 4.1: Composition of the thin augite film deposited onto a platelet placed next to a QCM via PLD. The numbers result from average values over the depth profile obtained with ToF-E ERDA shown in figure 4.1.

	abundance [at. %]
O	60.3 ± 0.9
Si	20.5 ± 0.5
Mg	8.9 ± 0.3
Fe	6.0 ± 0.2
Ca	1.8 ± 0.1
H	1.4 ± 0.1
C	1.1 ± 0.1

4.2 Experimental- and computational efforts

For this study, solely mass changes during ion irradiation of the deposited thin films were obtained. Therefore, only the according QCMs had to be installed in the sample holder for experiments. This allowed to use both, the SOPHIE and the SPECS ion beam setup, since neither the additional slot in the sample holder nor the electron source attached to the SOPHIE based setup were needed. The achievable ion current densities for 4 keV He^+ are similar in both setups, enabling irradiations with fluences in order of 10^{21} ions/m² within some 10 hours. After cleaning with 2 keV Ar^+ ions, irradiations under various different conditions were performed. As a first step, angular resolved sputter yield measurements with 2 keV Ar^+ ions were carried out. This standard scenario was already extensively studied with another silicate mineral wollastonite ($CaSiO_3$). Therefore, experience with sputtering of such thin films with similar composition was available (see [30] and [29]). Furthermore, the combination of a penetration depth of Ar in augite and its high sputter yield allow to reach a steady state of possible ion implantation and release due to sputtering much faster than for He or H at solar wind velocities [30]. In order to study the interaction of the solar wind with the Mercury analogue augite, mass change measurements were performed with 2 keV H_2 and 4 keV He^+ ions. The first was used as a substitute for 1 keV H, since achievable currents and signals are significantly increased for 2 keV H_2. Szabo *et. al* discussed the comparability of the sputter yield of 2 keV H_2 and 1 keV H, stating that a substitution is appropriate for the calcium silicate wollastonite. Tests of this hypothesis on the augite sample for a few angles verified the substitution $Y_{H,1\,keV} \rightarrow 0.5 \times Y_{H_2,1\,keV}$. Typically, sputter yield measurements with pristine samples and solar wind ions started under normal angle of incidence ($\alpha = 0°$). After prolonged irradiations, also more grazing angles up to $\alpha = 75°$ were measured as well. The experiments

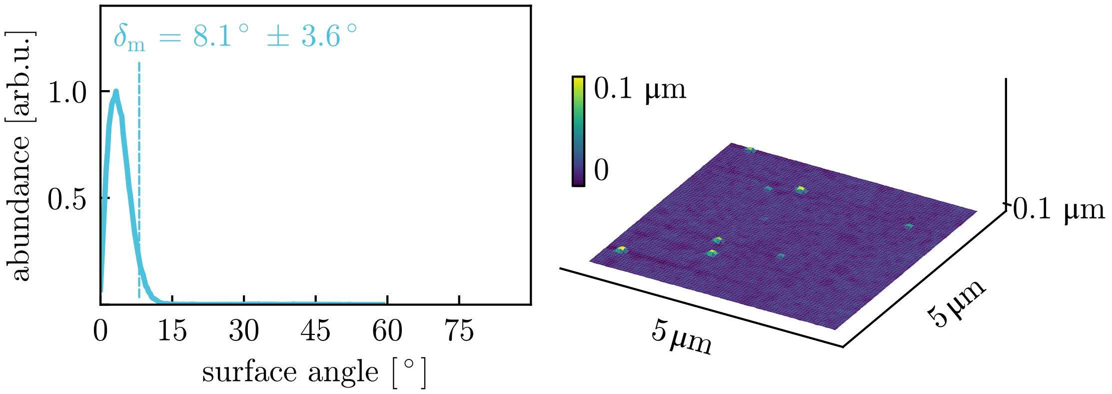

Figure 4.2: Angular distribution of the local surface inclination of a representative AFM image taken from an augite coated QCM (left). The mean surface inclination calculated from all obtained AFM images of that sample is indicated by an arrow. A 3D-visualization of the same image is shown on the right.

were accompanied with computer simulations using SDTrimSP in its 1D variant. Here, the set of parameters described in section 3.4.1 was used. The same density as for the thickness estimation from IBA of $3.3\,\mathrm{g/cm^3}$ was achieved via adaption of the oxygen sub-density. For calculations of sputter yields in dependence on the incidence angle α, the static mode of operation was used. All corresponding curves in this chapter show a fit according to Eckstein and Preuss [120] as calculated with the *angular sweep* feature in the SDTrimSP GUI program [121] to the simulation data. In addition, dynamic simulations including implantation of the ions and possible preferential sputtering were performed for selective cases. Due to the small δ_m value, no separate treatment of surface roughness by means of SDTrimSP-3D or SPRAY was necessary. With the dynamic mode of SDTrimSP, the fluence dependence of the mass change per impinging ion could be calculated and compared to the experiments.

Furthermore, TDS measurements were performed from the samples after irradiations with 4 keV $\mathrm{He^+}$ ions. Those could be used to verify whether He was implanted into the resonator samples by means of the attached QMA. An evaluation of the quartz frequency for the TDS measurements additionally allowed to quantify the amount of He released during a TDS heating cycle.

4.3 Results

The different methodologies used during this study allowed to analyze various aspects of sputtering and implantation of ions in the augite based thin films. In the following, the respective results are broken down into those two topics.

4.3.1 Sputter yields

Sputtering of augite with 2 keV Ar^+ ions was measured with various angles of incidence, showing no fluence dependence of Δm_{ion}, what could be verified with static computer simulations. The experimental values of Y are shown in figure 4.3 (orange points) together with SDTrimSP-1D simulations (blue line).

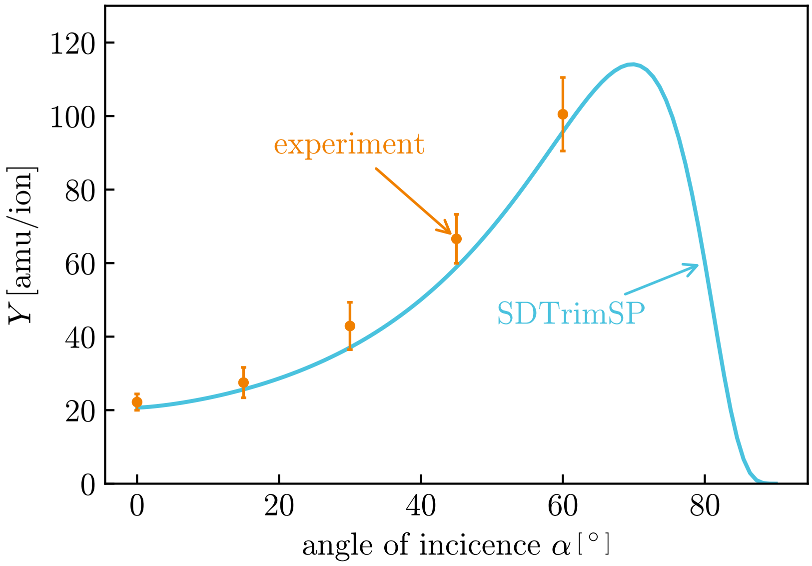

Figure 4.3: Sputter yield of 2 keV Ar^+ on augite, measured with the QCM (orange points) and simulated using SDTrimSP (blue line) in dependence on the angle of incidence α. The composition from table 4.1 was used together with a density of 3.3 g/cm^3 and the adaptations proposed in [30].

In the case of 2 keV H_2 ions, implantation into the pristine sample (i.e., after cleaning with Ar ions) at $\alpha = 0°$ was observed as reduced $\Delta f/\Delta t$ (cf figure 3.1 in den Methods). After this initial implantation, stable signals in Δm_{ion} were obtained. The sputter yields of 2 keV H_2 – divided by a factor of 2 – in dependence on α are shown in figure 4.4 as violet points, labeled *H*. According SDTrimSP results are shown by the dashed blue line, agreeing well with the experimental data.
For the case of 4 keV He^+ ions, prolonged irradiations were necessary under $\alpha = 0°$ in order to reach a steady state in the mass change per impinging ion Δm_{ion}. Similar as discussed by Szabo *et. al* in [30], this is attributed to an implantation of He in the sample. The steady state value, however, allows for an evaluation

of the sputter yield. Just as for Ar and H, these experimental values and the simulation results with SDTrimSP match very well. When turning the sample to different values of α, no further implantation was observed. Directly evaluated sputter yields, however, were substantially higher than predicted by simulations. Figure 4.4 shows those sputter yields initially obtained at the irradiation start. Just as for the implantation phase under normal incidence, prolonged irradiation revealed a (much smaller) fluence dependence of Y (or more precisely of Δm_{ion}), but here observable as continuous reduction. Steady state values of the sputter yield are also shown in figure 4.4 as green points, being in line with the according SDTrimSP simulations shown as blue line.

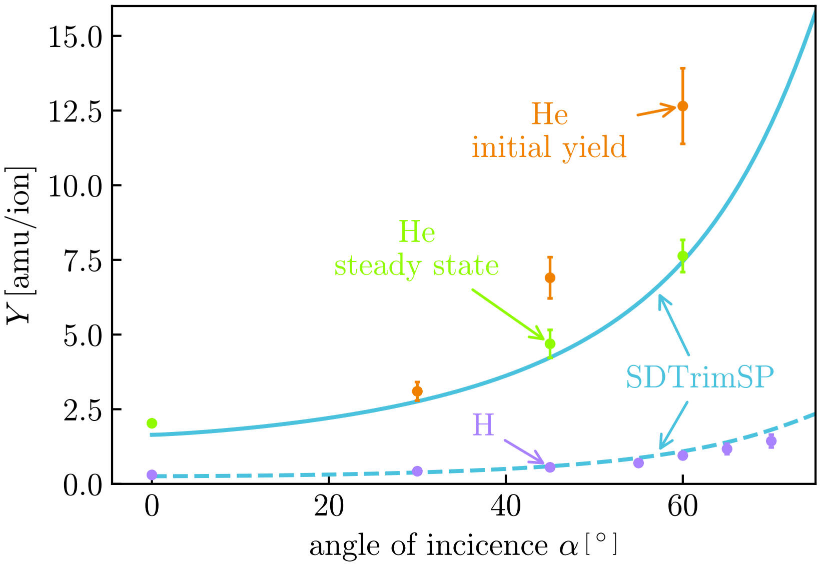

Figure 4.4: Angular dependent sputter yields for 4 keV ^{4}He$^+$ and 1 keV H. For He, signals directly at the irradiation start (labeled initial yields, orange points) and and after prolonged irradiations (steady state, green points) are shown. The data for 1 keV H was obtained by dividing data for 2 keV H_2 by a factor of 2. Corresponding SDTrimSP simulations with the same parameters as for 2 keV Ar are shown as well in blue (full line for He, dashed line for H).

4.3.2 Implantation of He

The mass change per ion upon the irradiation with 4 keV He$^+$ under $\alpha = 0°$ showed a very distinct dependence on the fluence, where even a net mass increase could be seen. The blue line (labeled RT) in figure 4.5 shows this fluence dependence for irradiations at room temperature. After a net mass increase of 1 - 2 $^{\mathrm{amu}}/_{\mathrm{ion}}$ in the beginning, Δm_{ion} continuously decreases, until a minimum of about $-4\,^{\mathrm{amu}}/_{\mathrm{ion}}$ is reached after a fluence of about $1 \times 10^{21}\,^{\mathrm{ions}}/_{\mathrm{m}^2}$. After some overshooting at shortly after $1.5 \times 10^{21}\,^{\mathrm{ions}}/_{\mathrm{m}^2}$, a steady state value of $\Delta m_{ion} = -2\,^{\mathrm{amu}}/_{\mathrm{ion}}$ is reached at a fluence of about $2.2 \times 10^{21}\,^{\mathrm{ions}}/_{\mathrm{m}^2}$. Variations of the ion current density between $(36 \pm 4) \times 10^{15}\,^{\mathrm{ions}}/_{(\mathrm{m}^2 \times \mathrm{s})}$ and $(68 \pm 7) \times 10^{15}\,^{\mathrm{ions}}/_{(\mathrm{m}^2 \times \mathrm{s})}$ in several irradiation cycles did not alter this trend. A flux dependence of the oscillatory behavior could therefore not be observed within that range. An implantation of the ions can lead to such a change in Δm_{ion} compared to sputtering alone, as was discussed in section 3.3.2. Therefore, experiments at elevated temperatures were conducted, potentially altering the mobility of implanted He and leading to a different fluence dependence of Δm_{ion}. Those measurements were carried out at a temperature of $T = 415\,\mathrm{K}$ – the minimum of the temperature dependence of the QCM's natural frequency ($^{df}/_{dt} = 0$). The resulting data are also shown as orange curve in figure 4.5 and labeled $T = 415\,\mathrm{K}$. Just as for room temperature, an oscillatory behavior can be seen and again a steady state value of $\Delta m_{ion} = -2\,^{\mathrm{amu}}/_{\mathrm{ion}}$ (see also 4.4) is reached after about $2.2 \times 10^{21}\,^{\mathrm{ions}}/_{\mathrm{m}^2}$. However, the dependence is much less pronounced and net mass increase never occurs. Assuming that implantation is the reason for deviations from the steady state sputter yield, equation 3.5 can be evaluated in both cases. Thereby, the total implanted mass density until an equilibrium of implantation and release of He is reached, can be approximated with a steady state sputter yield of $Y = 2.0\,^{\mathrm{amu}}/_{\mathrm{ion}}$. This results to $m_{impl,RT} = (222 \pm 40) \times 10^{19}\,^{\mathrm{amu}}/_{\mathrm{m}^2}$ for the irradiation at room temperature and $m_{impl,415K} = (105 \pm 22) \times 10^{19}\,^{\mathrm{amu}}/_{\mathrm{m}^2}$ at the elevated temperature of $T = 415\,\mathrm{K}$. A corresponding mean density of He in the material can be calculated under the assumption of a known depth profile. Yamamura [122] found similar trends in the implantation of ^{3}He with a kinetic energy of 4 keV into Mo. In that scenario, a constant concentration spanning from the surface to twice the range of the ions was found. Calculating the predicted range of He in augite with SDTrimSP, a value of $31 \pm 1.7\,\mathrm{nm}$ is found. Combining the implanted mass density for room temperature with the double range according to Yamamura, the He density can be approximated to $59\,^{\mathrm{g}}/_{\mathrm{cm}^3}$ or 1.8 wt.% of the sample, assuming a density of $3.3\,^{\mathrm{g}}/_{\mathrm{cm}^3}$. With an average mass of $21.8\,^{\mathrm{amu}}/_{\mathrm{atom}}$ in the sample according to IBA, this even results in 10 at. %.

To further evaluate the implantation of He in the samples, TDS measurements were performed for measurements at room temperature. Here, the samples were heated with ramps of $10\,^{\mathrm{mK}}/_{\mathrm{s}}$ and $20\,^{\mathrm{mK}}/_{\mathrm{s}}$, respectively, while simultaneously monitoring the He background pressure with the attached QMA. Those measurements were started shortly after irradiations were ended, guaranteeing that as little as possible He was released from the sample before the acquisition stared. Furthermore, an

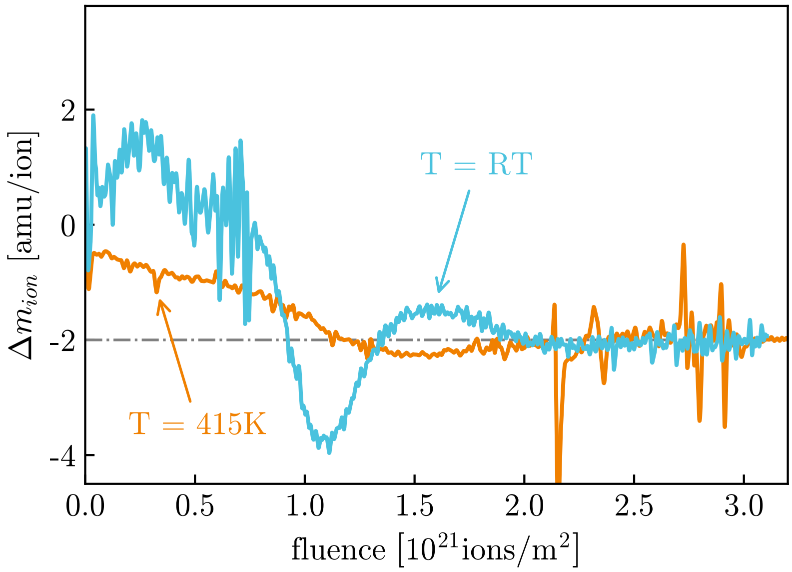

Figure 4.5: Mass change per impinging ion Δm_{ion} over ion fluence for 4 keV He^+ irradiations of the augite film under normal incidence. Two scenarios with the sample being at room temperature (RT, blue line) and at the minimum of the temperature dependence of the quartz resonators natural frequency at $T = 415\,K$ (orange line) are shown. Figure adapted from [76].

evaluation of the integrated frequency drift between irradiation and TDS revealed changes below 0.5 Hz, which equals $4 \times 10^{19}\,{}^{\mathrm{amu}}/_{\mathrm{m}^2}$ and therefore less than 2 % of the implanted mass. The relative He signals at the QMA for both heating ramps are shown in figure 4.6 ($10\,{}^{\mathrm{mK}}/_{\mathrm{s}}$ in blue, $20\,{}^{\mathrm{mK}}/_{\mathrm{s}}$ in orange; solid lines) together with the relative integrated signals (dashed lines). Both cases show a pronounced peak in He release, which is reached at $T = (411 \pm 20)$ K for the steeper ramp of $20\,{}^{\mathrm{mK}}/_{\mathrm{s}}$ and at higher temperatures of $T = (456 \pm 20)$ K for the flatter ramp of $10\,{}^{\mathrm{mK}}/_{\mathrm{s}}$. The according change in mass density cannot be resolved in real-time by the QCM, as the temperature dependence of the resonance frequency is superimposed to changes in f_Q due to the release of material and is much stronger in magnitude in this regime. However, the difference in f_Q at room temperature before and after such a TDS allows for a calculation of the total change of mass density $m_{released}$. On average, $m_{released} = (256 \pm 25) \times 10^{19}\,{}^{\mathrm{amu}}/_{\mathrm{m}^2}$ is released from the augite film during TDS. The contribution of adsorbed residual gas from the front of the quartz resonator can be neglected, due to the sputtering process and the starting of the TDS measurement directly after the irradiation. However, the backside of the QCM cannot be cleaned and release of material from this side can therefore alter the measurement results. In order to estimate uncertainties due this contribution, reference measurements after sputter cleaning of the front with 2 keV Ar^+ ions were carried out as well. Those resulted in $m_{control} = (10 - 60) \times 10^{19}\,{}^{\mathrm{amu}}/_{\mathrm{m}^2}$. When performing irradiations with 4 keV He^+ subsequently to such a heating cycle, the exact same behavior of Δm_{ion} over fluence as for pristine samples is observed. Consequently it can be stated that the amount of He released during TDS corresponds well to the total He mass implanted before.

The dynamic mode of SDTrimSP allows to conduct accompanying studies on fluence dependent measurements. Therefore, the irradiation of augite with He ions was simulated, using various different scenarios for the implanted ions. As inputs, results from IBA as depicted in figure 4.1 (without the contaminations) were used. Figure 4.7 shows the results for Δm_{ion} for the different calculated scenarios together with the experimental curve obtained at room temperature (blue). The static simulation value obtained without considering changes of the sample are indicated by the dashed gray line at $Y = -\Delta m_{ion} = 1.7\,{}^{\mathrm{amu}}/_{\mathrm{ion}}$. This is 13.5 % below the value obtained in the experiments (see figures 4.4 and 4.5). When changes of the stoichiometry are allowed, but no specific treatment of He is considered, most of it is implanted at a range of 31 ± 1.7 nm. Sputtering is not sufficient to reach this zone due to erosion within the investigated fluence. The dashed pink line shows the mass change per impinging ion for this scenario with a constant value of $\Delta m_{ion} = 2\,{}^{\mathrm{amu}}/_{\mathrm{ion}}$. With a limit of the maximum local He concentration in the sample, an unphysical accumulation of the projectiles in the sample can be avoided, while substituting it with the – also unphysical – removal of ma-

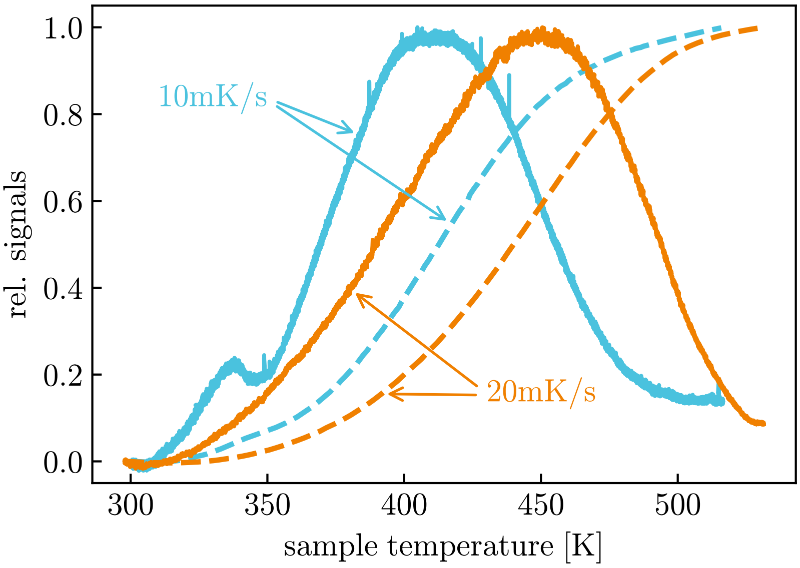

Figure 4.6: Relative signals of the ion current for He at the QMA over sample temperature while linearly increasing the latter (full lines) for two different ramps (10 mK/s in blue, 20 mK/s in orange). The relative integrated ion currents are shown as dashed lines. Figure adapted from [76].

terial from within the sample without transport mechanisms. However, setting this limit to 10 % (i.e., the value of implanted He assuming a box-shaped concentration profile mentioned above) allows for a reproduction of the general trend in the correct fluence regime (full pink line). Before the limit becomes effective, $\Delta m_{ion} = 2\,{}^{\mathrm{amu}}/_{\mathrm{ion}}$ just as in the case allowing unlimited implantation. At a fluence of about $0.45 \times 10^{21}\,{}^{\mathrm{ions}}/_{\mathrm{m}^2}$, Δm_{ion} first drastically declines and then slowly converges towards the sputter yield obtained with static simulations. The last investigated scenario allows for transport of implanted material in the sample. Best fitting values for the strength of *damage-driven diffusion* (η_0) and *pressure-driven transport* (K_0) were $\eta_0 = 5 \times 10^4$ and $K_0 = 100$ (see [65] for details on the implementation in SDTrimSP). The orange line in figure 4.7 shows the according results, also starting with $\Delta m_{ion} = 2\,{}^{\mathrm{amu}}/_{\mathrm{ion}}$, but slowly dropping directly afterwards. Again, the same value as in the static calculations is approached asymptotically. The spikes towards higher release (more negative values of Δm_{ion}) are related to artifacts of He release in the first computational layer. Just as for the simulation with a limited amount of He in the sample, the general trend is reproduced. However, all methods used for modeling He in the sample fail to catch the observed oscillations in Δm_{ion}. To further compare the computational outcomes to the experiments, the total implanted mass density can be calculated. For the scenario with 10 % He limit, this results to $m_{10\,\%} = 234 \times 10^{19}\,{}^{\mathrm{amu}}/_{\mathrm{m}^2}$. In the case of enabled transport, $m_{transp} = 184 \times 10^{19}\,{}^{\mathrm{amu}}/_{\mathrm{m}^2}$ of He are in total implanted in the sample.

4.4 Discussion

Sputter yields of the Mg rich pyroxene augite were investigated by means of a QCM technique for 2 keV Ar^+ ions as well as with the solar wind analogues 4 keV He^+ and 2 keV $\mathrm{H_2}^+$. Steady state values of the observed mass changes per impinging ion Δm_{ion} agree well with established computer simulations using the SDTrimSP code in all scenarios. In the case of He ions, however, repeatable pronounced phases of implantation lead to a fluence dependence of Δm_{ion} under normal incidence. The enhanced (negative) value of Δm_{ion} for the subsequent sputtering under grazing incidence angles is then attributed to smaller equilibrium concentration of He in the sample than for $\alpha = 0°$ due to the observed volatility of He in the sample. When performing TDS on the QCM previously saturated with He, clear signals of He can be seen in the QMA signal. Furthermore, a comparison of implanted mass during the irradiation $m_{impl,RT} = (222 \pm 40) \times 10^{19}\,{}^{\mathrm{amu}}/_{\mathrm{m}^2}$ and change in mass due to the heating cycle $m_{released} = (256 \pm 25) \times 10^{19}\,{}^{\mathrm{amu}}/_{\mathrm{m}^2}$ match within the measurements' uncertainties. Combined with the fact, that the same curves of Δm_{ion} over fluence are measured after heating, TDS measurements support the idea that indeed He implantation and release are observed. A more detailed inspection of

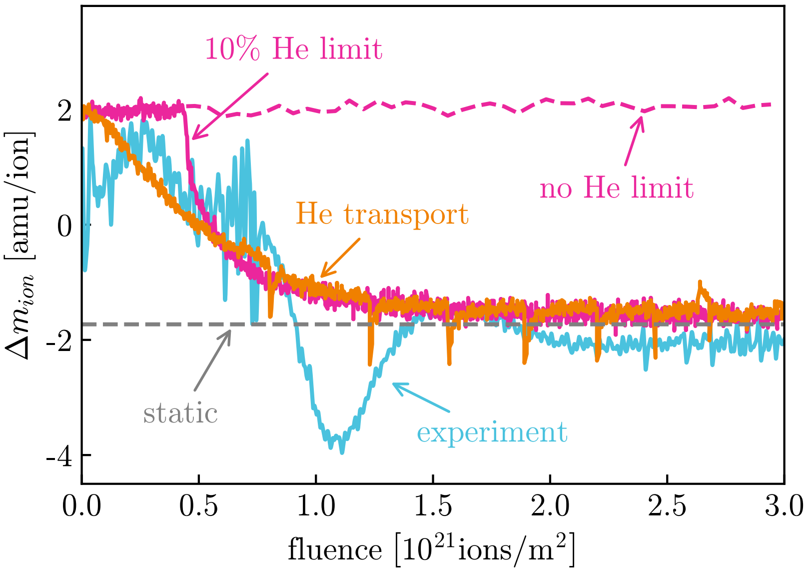

Figure 4.7: Fluence dependence of the mass change per impinging ion Δm_{ion} for irradiations of augite with 4 keV He^+ ions under normal incidende. The experimental curve taken at room temperature (blue line) is compared with SDTrimSP results. Static sputter yields (grey) and various dynamic approaches are shown. In those, He is either not treated specially (dashed pink line), limited to 10 % locally (full pink line) or transported in the sample via *damage-driven diffusion* and *pressure-driven transport* (orange line). Figure adapted from [76].

the TDS signals in combination with the irradiations performed at $T = 415\,\mathrm{K}$ might also explain the differences in Δm_{ion} compared to room temperature. At this temperature, even the peak of He can already be seen in the TDS spectrum with a ramp of $10\,\mathrm{mK/s}$. Helium is therefore much more mobile at this point than for irradiations at room temperature. Supplementary simulations with the dynamic mode of SDTrimSP allow to reproduce the implanted mass very well for the two different scenarios of limiting the total amount of He locally in the sample (105 % from the experiment) as well as with computation of diffusion (83 % of the experimental value). Also, the fluence range in which the implantation takes place fits the experimental results in both cases. However, since the distinct oscillatory behavior of Δm_{ion} could not be seen in the simulations, the precise mechanics seem to be missing in the simulations. Nevertheless, as mentioned when estimating the He density in the sample, Yamamura observed similar trends – although working with very different material. The fluence dependent study of ^{3}He implantation into Mo at the same kinetic energy of 4 keV shows this very similar behavior of He implantation [122]. Computer simulations with the ACAT-DIFFUSE code – another BCA code which allows for more advanced treatment of implanted projectiles – also show oscillatory emission of He from Mo within the same fluence range. This is achieved by implementing trapping and de-trapping as well as thermal diffusion of He at sites with different activation energies in the sample. Such mechanisms are not implemented in SDTrimSP. Although comparing Mo and a mineral might seem far-fetched, similarities during irradiations with He of both types of material go beyond this particular study. The formation of vesicles for example can be seen in Mo [123] as well as in Al_2O_3 [124] and the mineral olivine $(Mg_Fe)_2SiO_4$ [125].

4.5 Conclusion

Sputtering of the complex silicate augite ($(Ca,Mg,Fe)_2[Si_2O_6]$) could be reproduced by established simulation parameters for the SDTrimSP code, optimized for the calcium silicate wollastonite ($CaSiO_3$) [29, 30]. This worked in the reference case of 2 keV Ar^+ ions as well as for the solar wind relevant cases of 4 keV He and 1 keV H ions (resp. 2 keV H_2). The use of augite as an analogue material for the surface of the planet Mercury allows for conclusions about the interaction of the solar wind with the latter. Steady state sputter rates were not only in line between experiments and simulations within this study, but also agree well with values for wollastonite by Szabo *et. al* [29, 30]. However, no investigation of the charge state dependence of Y due to the He^{2+} content in the solar wind were performed. Since kinetic sputter yields are very similar, an extrapolation of the values presented by Szabo *et. al* in [30] for Mercury would seem plausible. Therefore, this study showed the broad applicability of the adaptations to SDTrimSP inputs suggested by Szabo

et. al. In addition, the implantation of He into the samples was analyzed by means of a QCM technique as well as with TDS. Fluences in the order of 1 - 2 $\times 10^{21}$ $^{\mathrm{ions}}/_{\mathrm{m}^2}$ were necessary to reach an equilibrium state of implantation and re-emission of He. Considering solar wind fluxes on the planet Mercury, only some hundreds of years would be needed to saturate minerals like augite on the surface [22]. With the measured total implanted mass per area of He, up to 10 at. % of He are found in the near surface region, assuming a box profile up to the double range of the ions in similarity to Yamamura [122].
However, at such time scales, the temperature dependence of both the mass change per ion during irradiations as well as for the release of He need to be taken into account as well. Helium has been seen to be very volatile in augite, completely leaving the implanted sample during heating to up to 530 K, restoring the samples previous state regarding implantation. Due to the lack of an atmosphere, surface temperatures on Mercury are very much dependent on the illumination by the sun - ranging from 100 K to 700 K [126]. Therfore, a complex cycle of He implantation and emission might be formed, depending on local impact points and their temperature in the 176 days it takes for Mercury to reach the same orientation and position in orbit around the sun. In this time span, temperatures are below 298 K (i.e., room temperature in the experiments) for half of the time [127]. In addition, other effects in outer space, like the circulation of material close to the surface due to various impacts called *gardening* [128] make precise predictions for real planetary bodies predictions even further challenging.

5 Results II: Interaction of ions with pressed Mercury analogs

The work presented in this chapter has partly been published in [83]

The interaction of the solar wind with planetary bodies in space represents a fairly complex system. Even when looking solely at a single mechanism, e.g., the sputtering of material, many parameters have to be dealt with. In corresponding experiments, sputter yields are oftentimes acquired with amorphous thin films. It is however questionable, how representative those results are for planetary bodies. Both the sputter yield as well as the emission characteristics can vary significantly between single crystals and amorphous materials, as was discussed in chapter 2. Quantifying possible differences for representative minerals can help to improve modeling efforts of the sputtering processes in general and therefore also lead to a better understanding of the total influence of the solar wind on planetary bodies in particular. For this purpose, the newly developed catcher QCM setup was utilized. Sputter yields of thin films on quartz resonators are compared with those of mineral pellets from the same material. Two different minerals are used – wollastonite ($CaSiO_3$) and enstatite ($MgSiO_3$). Both are pyroxene(-oids) and relevant as analogs for the planet Mercury. According to Jäggi *et. al* wollastonite can serve as proxy for the low-Fe regions, while enstatite is relevant due to the expected high Mg content on Mercury [26, 82].

5.1 Sample preparation and properties

Both silicates – provided by the collaborators at the University of Bern – were deposited onto QCMs by means of PLD (see section 3.2.2) and the resulting films analyzed subsequently. For the wollastonite, a single piece of mineral could be used as donor for the PLD process, while no enstatite of sufficient size was available. Therefore, a pressed pellet from ground enstatite was used for deposition instead. Characterization of the minerals used (i.e., the materials used as donors and for the pressed pellets) can be found in publications by Szabo *et. al* [29] and Jäggi *et. al* [82].

Sputtering of wollastonite based thin films was previously studied extensively by Szabo *et. al* (see [29, 30]). Therefore, the according QCM samples were already well characterized regarding their composition and their sputtering behavior understood well. For the enstatite on the other hand, no previous data existed. Due to the similar composition as the more complex augite (about 60 at.% O, 20 at.%

Si and > 8 at.% Mg; see chapter 4), however, no large differences in sputtering from that sample were expected. IBA analysis of the enstatite by Uppsala University revealed a composition very close to $MgSiO_3$, listed in table 5.1. This is in line with the results for the enstatite used as donor presented in [82].

Table 5.1: Composition of the thin enstatite film deposited onto a platelet placed next to a QCM during the PLD process. The numbers result from average values over a depth profile obtained with ToF-E ERDA as described in Chapter 3 and were evaluated at Uppsala University. Table adapted from [83].

	abundance [at. %]
O	58.2 ± 0.4
Mg	20.9 ± 0.4
Si	20.0 ± 0.4
C	0.5 ± 0.2
Fe	0.3 ± 0.1
H	0.2 ± 0.1

Analyses with AFM were performed as well on all the samples including PLD films and pressed pellets from both materials. This allowed to investigate possible influences of surface roughness on the samples during sputtering experiments. The according results for both materials can be seen in figure 5.1, where the distributions of surface slopes are shown. The average value of the first moments from all acquired AFM images are labeled as δ_m at their positions in the graphs, including their values and an uncertainty approximation. In the case of the wollastonite samples, both the pellet (orange curve) and the thin film on a QCM (blue) show very similar trends and small values of δ_m. Cupak *et. al* have shown, that the contribution of surface roughness on the sputter yield is only minor for this regime [41]. For the QCM, however, a second peak is seen at about 30°, which is related to some larger particles deposited at the surface during the PLD process. For the enstatite samples, a different situation was encountered (figure 5.1 right). While the thin film was smooth (blue line) – just as in the other investigated cases – a significantly rougher surface was found for the pellet (orange line). This can also be seen in the high δ_m value of 35.7° ± 4.5° compared to 10.2° ± 2.1° for the thin film. At such a high value as seen for the pellet, a modification of the sputter yield due to its surface roughness is expected and a separate treatment required. The discrepancy between the two enstatite surfaces can also be seen in figure 5.2, where representative 3D visualizations of AFM images from the QCM (left) and the pellet (right) are compared at the same z-scale (but with different color scale for visibility of the flat QCM sample).

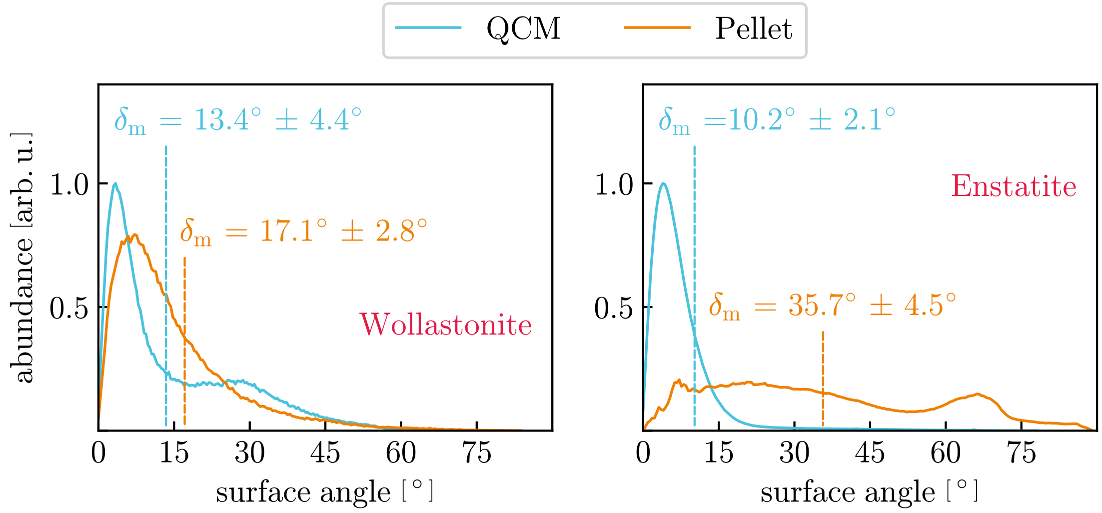

Figure 5.1: Distributions of the local surface angles of representative images for the wollastonite (left) and enstatite (right) samples used for this study. Both QCMs (blue) and the wollastonite pellet (orange) show characteristics of rather flat samples according to Cupak *et. al* [41]. The enstatite pellet (orange), however, has a much rougher characteristic. The first moments calculated from all respective images are indicated by arrows with label δ_m. The peak for the wollastonite QCM at 30° is related to a few individual particles from the PLD process at the otherwise smooth surface. The one seen for enstatite between 60° and 70°, however, is a tip artifact (see explanation in chapter 3)but only has a minor contribution to the total distribution. Figure adapted from [83].

5.2 Experimental and computational efforts

Investigations of the sputtering properties of the QCMs and the pressed mineral pellets were carried out using 2 keV Ar^+ ions for both wollastonite and enstatite samples. Further analysis with more solar wind relevant He^+ ions at a kinetic energy of 4 keV were carried out solely for the enstatite case. For the irradiations of the samples with ions in the keV energy regime, not only sputtering has to be considered close to the surface, but also the formation of damages. The depth of penetration for the Ar ions in the enstatite is only 1.1 nm according to SDTrimSP simulations. As all samples are sputter cleaned with Ar ions prior to the actual measurements, this damaged layer is always present in the beginning. Due to the

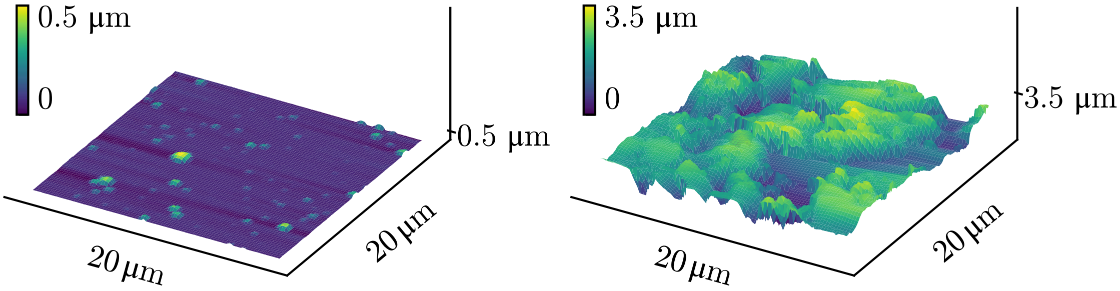

Figure 5.2: Representative AFM images of the enstatite samples. The thin film on a QCM (left) shows only small surface features, while the pressed mineral pellet (right) does posses a significant roughness. Both images have the same scaling, the color-code however is different in order to visualize also structures on the QCM. Figure adapted from [83].

comparably small range of a few material layers and the high sputter yield of Ar, the 1.1 nm present an upper limit for the damaged zone. Due to the dynamic situation of damage production and the retraction of the surface by sputtering, a precise evaluation of a damage profile is complicated and not possible by static simulations. This is of course also the case for all Ar experiments.

For He, however, the situation is quite different. A saturation of damages in silicate minerals upon He impact and the resulting amorphization has already been seen and discussed in various studies (cf. [82, 125, 129–131]). The fluences required to reach a saturation of damages has been found to be in the range of $10^{21} - 10^{22}\,\mathrm{ions}/\mathrm{m}^2$. Not only is the zone reached and altered by the Ar ions used for cleaning sputtered away within this fluence, but also is the sample in a saturated state considering amorphization by ion beam damages within the depth relevant for sputtering. Furthermore, reference measurements were performed, where the pellet was cleaned with the combined heating and injection of 20 eV electrons. Those also resulted in measurements without fluence dependence.

For the pressed mineral pellets, a determination of sputter yields was not possible with a classical QCM technique alone. In addition to the evaluation of sputter yields of the QCM samples via direct irradiation, catcher measurements with both methods described in section 3.1.2 were performed. For enstatite, pre-coating of the catcher was carried out, while being not necessary for experiments with wollastonite. The fluence required for one measurement cycle was in the same range as for amorphization of the minerals - namely about $10^{21}\,\mathrm{ions}/\mathrm{m}^2$.

In order to accompany the experiments on sputtering of flat samples (i.e., both wollastonite samples and the enstatite coated QCM), SDTrimSP simulations with the adapted parameters introduced by Szabo *et. al* [30] were carried out. Due to the close proximity of the IBA results to the nominal compositions for both samples, the latter were used for calculations. Regarding sample density, a value of 2.86 g/cm³ [132] was used for wollastonite and 3.3 g/cm³ for enstatite [119]. In addition to those simulations for flat samples, calculations with the SPRAY code were carried for the pellet. Therefore, the effects of surface roughness on the sputtering process for both – flat wollastonite pellet and the rough enstatite pellet– could be evaluated. For this purpose, the same sets of of AFM images as used for characterization were used as inputs together with SDTrimSP generated data for sputtering of flat samples.

5.3 Results

The use of QCMs with thin, amorphous layers of the desired material deposited first allowed for a determination of sputter yields as described in section 3.1.1. Such measurements were performed for 2 keV Ar^+ on wollastonite and enstatite. Additionally, the solar wind relevant 4 keV He^+ ions were used for irradiations of enstatite alone. For wollastonite, literature values for sputtering by Ar exist by Szabo *et. al* ([30]), which could be very well reproduced. The directly measured sputter yields obtained during this thesis and literature values from Szabo *et. al* are listed in table 5.2.

Table 5.2: Sputter yields directly obtained with QCMs (Y_{QCM}) using the conventional QCM technique for 2 keV Ar^+ and 4 keV He^+ ion irradiations. Data for wollastonite are from [30] and were verified with the used sample. Table adapted from [83].

Thin film sputter yields [amu/ion]

α	*Wollastonite [30]*	*Enstatite*	
	Ar	Ar	He
0°	21.0 ± 1.5	17.6 ± 2.1	1.8 ± 0.14
30°	36.3 ± 3.8	55.0 ± 11.0	-
45°	58.2 ± 5.5	78.3 ± 9.4	4.8 ± 0.42
60°	89.8 ± 6.6	132 ± 15.9	9.5 ± 0.82

Measurements with wollastonite represent an ideal reference case for comparison of amorphous thin films (the QCM samples) and pressed mineral pellets with the catcher setup. Not only are literature values for sputtering from past studies available, but also effects of surface roughness can be expected to contribute only marginally (for the QCM and the pellet). Those measurements were solely performed without the pre-coating procedure, therefore absolute signals are not quantitative. Due to the repeatability of the catcher signals for measurements performed directly after each other, however, a relative comparison between pellet and QCM is possible. Irradiations were performed with 2 keV Ar^+ ions, where effects of ion induced heating of the catcher discussed in section 3.3.3 are negligible. Figure 5.3 compares the obtained signals for irradiations of pellet (orange) and QCM (blue). There, the catcher signals normalized to the maximum from irradiations of the QCM are given for various angles β between sample surface normal and catcher. The ion beam impact directions are indicated at $\alpha = -\beta$ (i.e., backward direction). In addition, a fit of shape $A \cos{(\beta - \zeta)}^n$ (Equation 3.12) to the distribution of sputtered material from SDTrimSP simulations for the same system (counting only particles emitted in the solid angle of the sensitive catcher surface) and scaled to the experimental data is shown as dashed purple line. Two angles of incidence were investigated, placed in the meaningful range of α which can be used in the experiments (also see section 3.3.3). On the left side of figure 5.3, the angle of incidence $\alpha = 45°$ is shown, while $\alpha = 60°$ can be seen on the right side. In both cases, agreement between pellet and QCM data is excellent. It has to be noted, however, that only four data points exist for QCM irradiations at $\alpha = 45°$. For one of those – at $\beta = 55°$ – a discrepancy between pellet and QCM signals can be seen. Due to the fact, that all other data points for the respective value of α match well, this is seen as an outlier. Another aspect that can be seen are the higher signals in forward direction ($\beta > 60°$) in the experiments for $\alpha = 45°$ compared to $\alpha = 60°$. This is not only counter-intuitive considering the physics of sputtering, but also not in line with the SDTrimSP results, where no clear difference can be seen. A possible explanation for this observation is given in the discussion section of this chapter.

In the case of enstatite the quantitative approach was used, allowing a determination of the quantity $Y_{C,\Omega}$. Just as for wollastonite, a comparison between pellet and QCM sample were first performed with 2 keV Ar^+ ions. The results are shown in figure 5.4. Again, pellet data is shown in orange, QCM data in blue and SDTrimSP emission profiles as dashed purple lines, with the maximum scaled to the QCM data. In addition to the obtained data points, cosine fit functions of shape $A \cos{(\beta - \zeta)}^n$ to the experimental data are plotted as full lines in the respective colors. Those fitted functions were then also used for integration of the distributions of sputtered material and the calculation of r. The results for $\alpha = 45°$ (left) and $\alpha = 60°$ (right) are presented with the same scale, making them directly comparable. A clear increase in the signal for irradiations of the

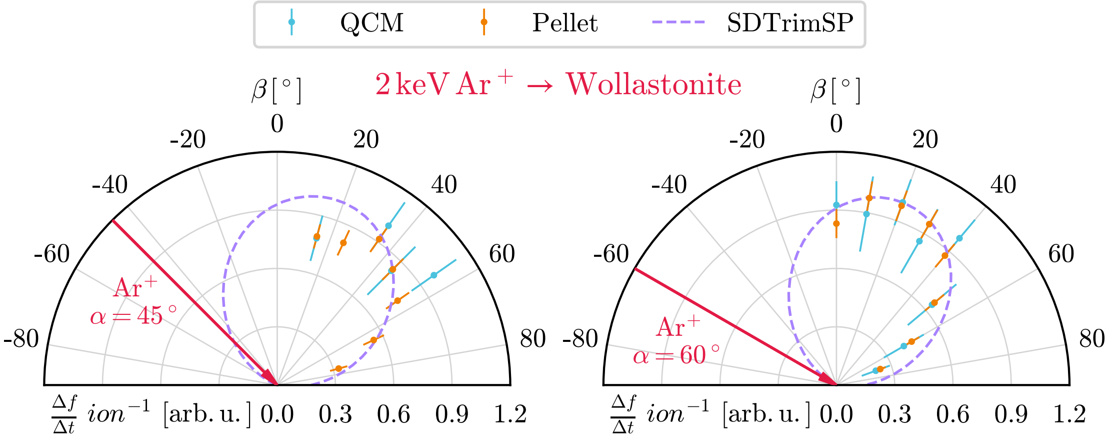

Figure 5.3: Signal at the catcher in dependence on the detection angle β for experiments with wollastonite ($CaSiO_3$) and 2 keV Ar^+ ions. Data for irradiations of the pellet (orange) and the QCM (blue) are shown for the impact angles $\alpha = 45°$ (left) and $\alpha = 60°$ (right). In addition, SDTrimSP results for the sputtered material in the same angle as covered by the sensitive catcher area are shown as dashed purple line by a fit of the shape $A \cos(\beta - \zeta)^n$. Figure adapted from [83].

QCM can be seen from $\alpha = 45°$ to $\alpha = 60°$. This is in line with the increase of the directly measured sputter yield for this (rather flat) sample, listed in table 5.2. For the pellet, however, curves with similar magnitude are obtained for both impact angles. The qualitative agreement for the flat samples between the simulations (SDTrimSP) and the experimental curves (QCM) is also good.

For the solar wind relevant 4 keV He^+ ions, the same curves were obtained, again varying β for the impact angles of $\alpha = 45°$ and $60°$. In figure 5.5, the results of those measurements are shown with the same layout as in figure 5.4. This time, the scale for $Y_{C,\Omega}$ is reduced by a factor of 10 compared to the results with 2 keV Ar^+ ions. Again, a significant increase in signal can be seen for the irradiations of the flat QCM sample when going from $\alpha = 45°$ to $60°$. This increase is much less pronounced for the pellet sample, but this time noticeable. The direction of the emission cone is also very similar to the irradiations with 2 keV Ar^+ ions. This is, however, not captured by the SDTrimSP simulations, which predict distributions closer to the surface normal ($\beta = 0°$).

From the combined results of both – conventional QCM and catcher measurements – angular dependent sputter yields for the pellet Y_{pellet} can be calculated using Equation 3.10 as described in section 3.1.2. The necessary ratio r between the catcher signals of QCM and pellet were evaluated by weighted summation

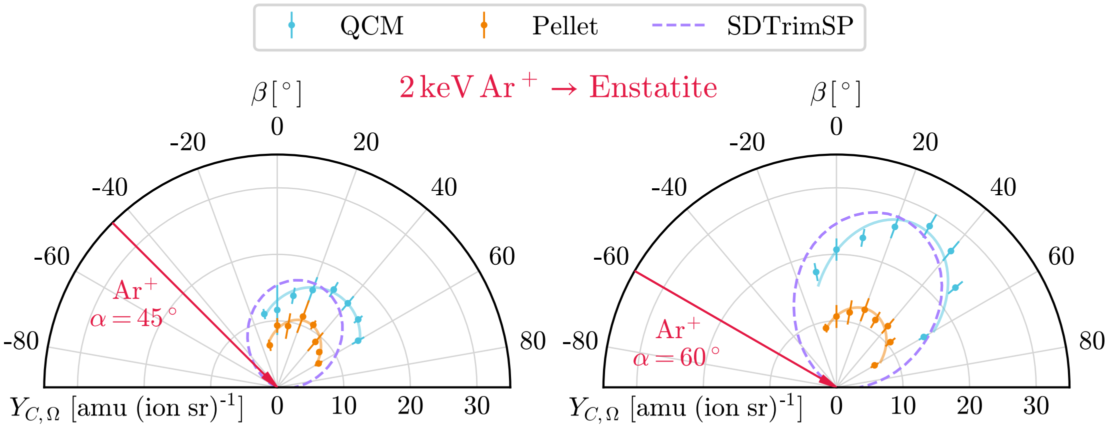

Figure 5.4: Signal $Y_{C,\Omega}$ at the catcher in dependence on the detection angle β for experiments with enstatite ($MgSiO_3$) and 2 keV Ar$^+$ ions. Data for irradiations of the pellet (orange points) and the QCM (blue points) are shown for the impact angles $\alpha = 45°$ (left) and $\alpha = 60°$ (right). Fit functions of the shape $A \cos(\beta - \zeta)^n$ are added to the data as lines in the according colors. In addition, fits with the same function are also shown for SDTrimSP results of the sputtered material in the same angle as covered by the sensitive catcher area as dashed purple lines. Figure adapted from [83].

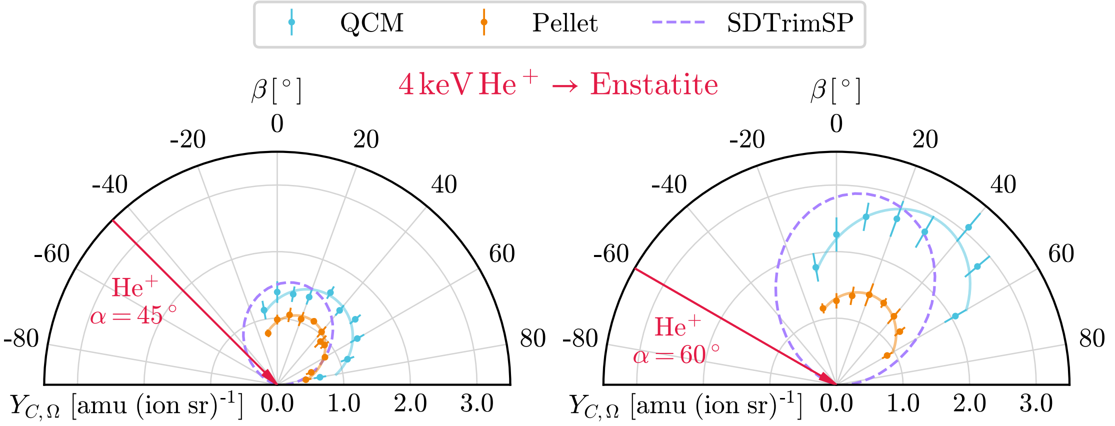

Figure 5.5: Signal $Y_{C,\Omega}$ at the catcher in dependence on the detection angle β for experiments with enstatite ($MgSiO_3$) and 4 keV He^+ ions. Data for irradiations of the pellet (orange points) and the QCM (blue points) are shown for the impact angles $\alpha = 45°$ (left) and $\alpha = 60°$ (right). Fit functions of the shape $A \cos(\beta - \zeta)^n$ are added to the data as lines in the according colors. In addition, fits with the same function are also shown for SDTrimSP results of the sputtered material in the same angle as covered by the sensitive catcher area as dashed purple lines. Figure adapted from [83].

according to Equation 3.11 for the wollastonite samples and from the integrated fitting functions for the enstatite. Table 5.3 lists the calculated values for Y_{pellet} and the according used ratios r.

Table 5.3: Sputter yields of the mineral pellets Y_{pellet}. The values were calculated from the ratios r between catcher signals of QCMs and pressed mineral pellets combined with Y_{QCM} using Equation 3.10. The corresponding values of r are given below. Table adapted from [83].

Pellet sputter yields [amu/ion]

	α	*Wollastonite*	*Enstatite*	
		Ar	Ar	He
Y_{pellet}	45°	53.5 ± 13.3	43.8 ± 11.0	3.26 ± 0.82
	60°	89.8 ± 22.5	66.0 ± 16.5	5.13 ± 1.28
r	45°	0.92 ± 0.18	0.56 ± 0.13	0.68 ± 0.14
	60°	1.0 ± 0.20	0.50 ± 0.10	0.54 ± 0.11

The use of SDTrimSP and SPRAY – the latter with SDTrimSP data and AFM images as input – allows for a direct evaluation of the effects of surface roughness on the sputter yield. Those results are directly comparable to the experiment, where flat QCM samples and rough pellets were used. Just as in the experiments, the ratio between the two outcomes can be calculated and subsequently compared to r. The according simulated sputter yields for all combinations of samples and ions are listed in table 5.4 for wollastonite and in table 5.5 for enstatite. In both tables, the ratio between the two corresponding simulations (SPRAY and SDTrimSP) are given in brackets. For wollastonite, almost no difference for $\alpha = 45°$ and a reduction of 16% for $\alpha = 60°$ are calculated. This is very much in line with the expected modifications for the given small value of $\delta_m = 17.1° \pm 2.8°$ (see figure 7 in [41]). For enstatite, however, significant reductions are predicted by the SPRAY simulations. This reduction can be seen in all cases listed in table 5.5.

Additionally, all sputter yield results obtained for enstatite are compared in figure 5.6. On the left side, the case of 2 keV Ar^+ is shown, while 4 keV He^+ measurements can be seen on the right. Simulation outcomes are indicated by lines, with SDTrimSP in solid blue and SPRAY as orange dashed lines. Experimental values are shown by points (flat QCM in blue, rough pellet in orange). Therefore, all *flat* cases are represented in blue, whereas *rough* cases have an orange coloring. The agreement between the experiments and the simulations is very good in general. SPRAY outcomes match all four experimental values within the respective

Table 5.4: Simulated sputter yields for wollastonite from SDTrimSP – representing flat – and the SPRAY code using AFM images as input – representing the rough pellet samples. The ratio between those results is given in brackets. Table adapted from [83].

Simulated sputter yields:
Wollastonite [amu/ion]

α	*SDTrimSP*	*SPRAY*	
45°	60.16	58.35 ± 1.11	(0.97)
60°	98.28	82.46 ± 3.77	(0.84)

Table 5.5: Simulated sputter yields for enstatite from SDTrimSP – representing flat – and the SPRAY code using AFM images as input – representing the rough pellet samples. The ratio between those results is given in brackets. Table adapted from [83].

Simulated sputter yields:
Enstatite [amu/ion]

α	*Ar*			*He*		
	SDTrimSP	*SPRAY*		*SDTrimSP*	*SPRAY*	
45°	61.35	43.94 ± 3.56	(0.72)	4.40	4.06 ± 0.22	(0.92)
60°	97.84	55.80 ± 5.38	(0.57)	7.99	5.53 ± 0.65	(0.69)

error bars. However, SDTrimSP generally underestimates the angular dependence of the sputter yield for both ion species. Therefore, the results are below the experimental values for grazing ion incidence but above at $\alpha = 0°$.

5.4 Discussion

The influence of sample roughness and crystal structure on the sputtering process was investigated for 2 keV Ar^+ and 4 keV He^+ ions impinging on analogs for planetary surfaces like that of Mercury. In order to untangle the influence of surface roughness, results for flat (thin films and the wollastonite pellet) and a rough sample (the enstatite pellet) are compared. The use of flat, amorphous films of same stoichiometry on QCM also allowed for a calibration and therefore for quantitative analysis of pellet sputter yields. In the case of wollastonite, where a similar

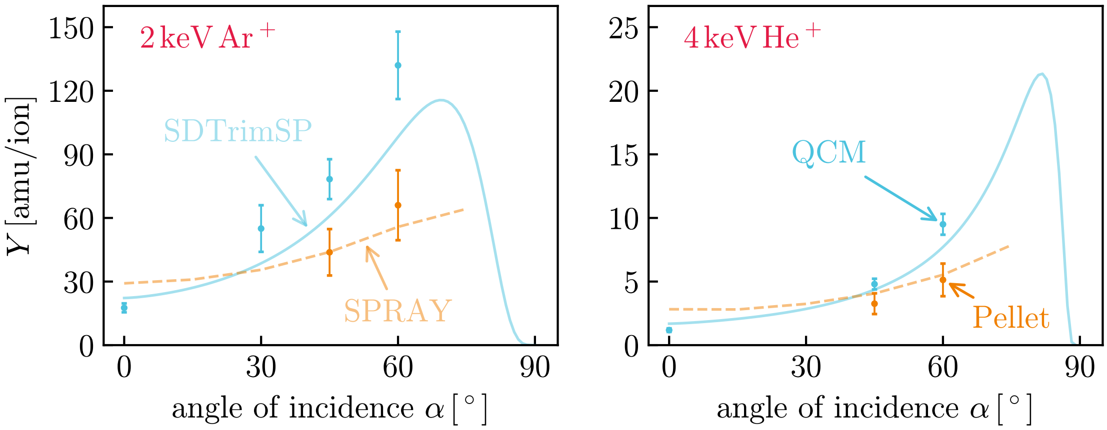

Figure 5.6: Sputter yields of enstatite as they are obtained from experiments (points) and simulations (lines) for 2 keV Ar^+ (left) and 4 keV He^+ (right) irradiations. QCM sputter yields Y_{QCM} represent flat samples and were obtained with the classical QCM technique for sputter yield measurements. The pellet sputter yields Y_{pellet} had to be calculated from catcher data and the reference value of Y_{QCM} using Equation 3.10. SDTrimSP simulations are shown as full blue lines, whereas SPRAY outcomes including the pellet surface are depicted by dashed orange lines. Figure adapted from [83].

roughness parameter was found between QCM and pellet by AFM measurements, excellent agreement is seen in the catcher data. The calculated values of the ratio r for both incidence angles underline this statement ($r = 0.92$ for $\alpha = 45°$, $r = 1.0$ for $\alpha = 60°$, see table 5.3). This is in line with the accompanying simulations for roughness effects by the SPRAY code, where only minor reductions in the sputter yield are seen. The corresponding values from table 5.4 show ratios between rough and flat simulations of 0.97 for $\alpha = 45°$ and 0.84 for $\alpha = 60°$. These results are a clear indication, that the material's crystal structure does not alter the sputtering process for wollastonite – at least not in the investigated fluence range of $10^{21} - 10^{22}\,\mathrm{ions/m^2}$.

The unexpected decrease in signals for large catcher values ($\beta > 60°$) at $\alpha = 60°$ compared to 45°, however, also needs to be discussed, ensuring that no systematic errors in the method are overseen. An explanation might be found in the measurement principle. By measuring mass changes at the catcher, no deposition of material alone is detected, but rather a total mass change. When looking at the reflection of Ar ions upon impact on wollastonite for the two different incidence angles with SDTrimSP, reflections of 16 % of the ions for $\alpha = 60°$ and only 3 % for 45° are found. Figure 5.7 shows the distributions of those reflected ions, restricted for the catcher solid angle with same parameters for $\alpha = 45°$ (purple line) and $\alpha = 60°$ (red line). Due to equal binning, the distributions can be directly compared. It is eminent, that the main fraction of reflected ions for $\alpha = 60°$ impacts the catcher in exactly that region, where the unexpected decrease in deposition rates is observed. Therefore, the small deposition rates get further reduced due to sputtering of the material from the catcher by those reflected ions.

For the enstatite samples, quite different observations were made than for wollastonite. In this case, data points were acquired in a broader range of β due to the higher relevance for the planet Mercury. This allows for a more precise evaluation of angular distributions, including a fitting of the data points as was presented in figures 5.4 and 5.5.
In contrast to the flat wollastonite pellet, the ratios r (this time calculated from the integrated fit functions) are significantly smaller than unity for all cases. Furthermore, the angular dependence of the sputter yield is reduced, which can be seen from the decreasing r values when going from $\alpha = 45°$ to 60°. This is a common phenomenon for roughened surfaces, as was discussed in Section 2.1. Not only the magnitude of the signals varies between QCM and pellet irradiations. Also the shift of the distributions with respect to the surface normal is different. The according tilt angle ζ from the fit functions ranges from $21° - 25°$ for the pellet irradiations and $27° - 34°$ for the QCM. Such changes in the angular distributions

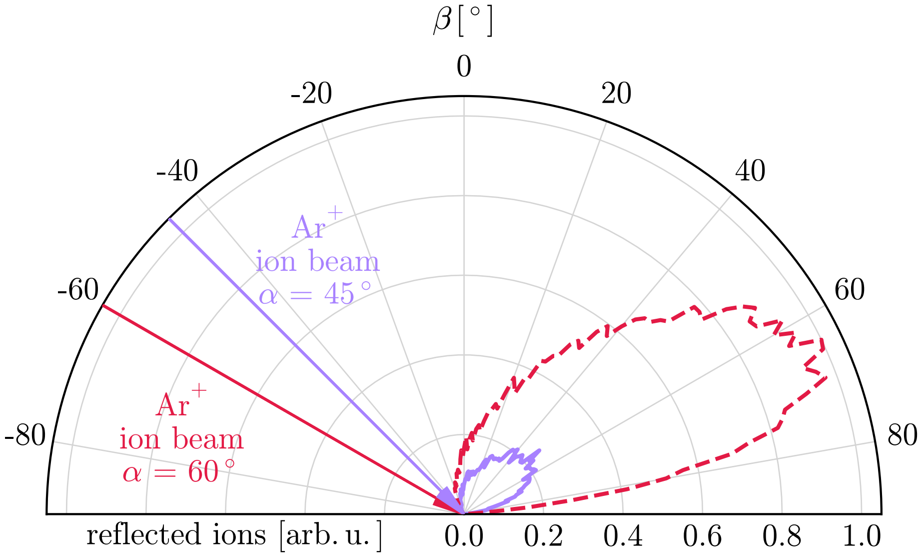

Figure 5.7: Distributions of reflected ions for flat samples from SDTrimSP for 2 keV Ar^+ impinging onto wollastonite, restricted to the catcher solid angle. The data for $\alpha = 45°$ is shown in purple, $\alpha = 60°$ in red. Both were obtained with the same number of primary particles and are plotted with equal binning, making them comparable quantitatively. Figure adapted from [83].

of sputtered material are also known to be caused by surface roughness [41]. When comparing the experimental results with the simulated influence of surface roughness, however, some deviations can be seen. The reduction of the sputter yield due to surface roughness is not fully captured by the SPRAY code, as can be seen when comparing r from table 5.3 with the ratios given in table 5.5. This is especially the case for irradiations with 4 keV He^+ ions. A possible explanation might be found in the angular dependency of the sputter yield calculated by SDTrimSP and shown in figure 5.6 and used as inputs for SPRAY. The sputter yield reaches its maximum shortly after the experimental values for 2 keV Ar^+, whereas it climbs further for 4 keV He^+ ions. There, it increases by 390 % from $\alpha = 45°$ to the maximum value at $\alpha = 82°$ (see figure 5.6). Such an angular dependency could reduce roughness effects at the intermediate angles of $\alpha = 45°$, since the sputter yield on local slopes $(Y(\alpha_{loc}))$ leads to an increased value $(Y(\alpha_{loc}) > Y(\alpha))$ for a wider range of impact angles compared to Ar. Sputter yields for such grazing incidence angles, however are not verified experimentally. Shortcomings for sputtering by 4 keV He^+ at grazing incidence, however, can be seen in the angular distribution of the sputtered particles, where SDTrimSP predicts an emission closer to the surface normal as was observed experimentally.

Nevertheless, the SPRAY code is still able to reproduce the general trend of the sputter yield very well when going from the flat sample to the pellet, which can also be seen in figure 5.6. This supports the hypothesis, that differences between QCM and pellet sputter yield can be solely explained by surface roughness in the investigated fluence range. Furthermore, the lack of a dependency of catcher signals on the irradiation fluence indicates, that this is also valid for a fluence smaller than 10^{21} ions/m² (i.e., one measurement cycle).

5.5 Conclusion

By combining conventional QCM techniques and the newly developed catcher QCM for full angular studies of ejecta, sputter yields for amorphous films and mineral pellets could be compared. Thereby, not only qualitative analysis could be made, but quantitative statements were possible. Due to the use of the two minerals wollastonite ($CaSiO_3$) and enstatite ($MgSiO_3$), a more comprehensive study was possible. On the one hand, wollastonite samples were solely flat and had equal stoichiometry. Therefore, only the crystal structure remained as distinctive feature with regard to ion sputtering. There, no difference could be seen upon irradiations with 2 keV Ar^+ ions. This also validates the results of previous measurements performed with amorphous wollastonite based films (cf. [29,30]) for material phases more applicable for planetary bodies. For the Mercury analog enstatite ($MgSiO_3$), in addition to the structural differences between the amorphous films and the polycrystalline pellets significant surface roughness was found for the latter. In this case, sputter yields for the investigated impact angles were reduced for the mineral pellets when compared with the flat QCM samples.

The combination of the BCA code SDTrimSP and the ray-tracing code SPRAY for roughness evaluation allowed to reproduce the trends by using AFM images of the pellets as input. Combining the results for both samples it can be concluded, that the sputter yield for planetary analog materials like the used silicates does not depend on the crystal structure – at least not in the investigated fluence range. As this range corresponds to only several hundreds of years of solar wind exposure on Mercury, a general validity for Mercury can be expected [22]. Therefore, both laboratory experiments with amorphous thin films as well as simulations with BCA codes (also assuming amorphous solids) are justified. It could also be experimentally observed, that surface roughness has a significant impact on the sputter yield for planetary analogs, even though only conventional rough surfaces were investigated during the experiments. Taking realistic – regolith covered – surfaces for planetary bodies into account, might have an even greater influence on the sputtering behavior which will be elaborated in further studies.

6 Results III: Sputtering of the Moon

It was already extensively discussed, that laboratory experiments are crucial for understanding the interaction of the space environment with bodies in space. For most such bodies, this involves investigations of the surface composition far from earth as a first, and the selection of adequate analogs for experiments on earth as second step. For the Moon, however, the situation is different. With the sample return by the Apollo missions, the search for adequate analogs can be skipped and actual lunar material used for experiments.

So far, no experimental sputter yields for actual lunar samples have been published – at least to the author's knowledge. Estimations of sputtering of the lunar surface is therefore approximated with simulations, e.g. with TRIM.SP [133] or also by experimental data of analog materials. An extensive study with a wide range of such materials was even performed before the first landing on the Moon by Wehner *et al.* in 1963 [134].

In this thesis, however, sputter yields of the sample with the number *68501* returned from the Moon by the *Appollo-16* mission could be investigated. Since the reliability of the method was already established with the results of chapter 5, the focus was exclusively on solar wind relevant ion species. For this purpose, conventional sputter yield measurements with QCMs – i.e., thin film sputter yields – were acquired for 2 keV H_2^+ and 4 keV He^+, two proxies for the solar wind with its approximate velocity equivalent to 1 keV per amu. In the following, data for 2 keV H_2^+ ions divided by a factor of two are referred to as 1 keV H^+ results.

Computer simulations with SDTrimSP – in both the 1D and the 3D variant – and the SPRAY code were performed used for evaluation and interpretation of the experimentally obtained data.

6.1 Sample preparation and properties

The lunar sample with the number 68501 was collected by the astronauts of the Apollo 16 mission at Station 8 during their stay on the Moon in April 1972 [95,96]. Figure 6.1 shows the position of the mission's landing site and illustrates the collection of material by an actual photograph taken during that mission. It was delivered by NASA (curator Ryan Zeigler) to the collaborators at the University of Bern in the form of loose powder. Just as the ground material used in the study presented in chapter 5, this powder was pressed into stainless steel holders with a hydraulic press. In contrast to those pellets, however, a layer of KBr was used underneath to to improve the materials' adhesion after pressing in the holders.

For utilizing the same experimental methodology as for sputter yield evaluation of realistic Mercury analogs (chapter 5), amorphous thin films on QCM resonators were needed for the lunar samples. Just as for the other investigated materials, those were produced by A. Nenning at the Institute of Chemical Technologies and Analytics at the TU Wien by means of PLD. Since only the pressed pellets were available, those were used as donors for the PLD process as well.

Subsequently, all thin film samples used for sputter yield evaluation were characterized by means of ToF-E ERDA performed on platelets placed next to the resonators during the PLD process. As was discussed in 3.2.2, only limited data on the Apollo sample composition was available. Therefore, ToF-E ERDA was performed for one of the pressed mineral pellets as well. For the combinations of Al:Si, Fe:Cr and Ca:K a clear separation in the ToF-E ERDA spectra was not possible. Therefore, those were divided according to their occurrence in the lunar sample as stated in [102]. For the elements Cr and K, this results in negligible contents. Only minor deviations between the two types of samples were found, showing that PLD also reproduced the stoichiometry in this case.

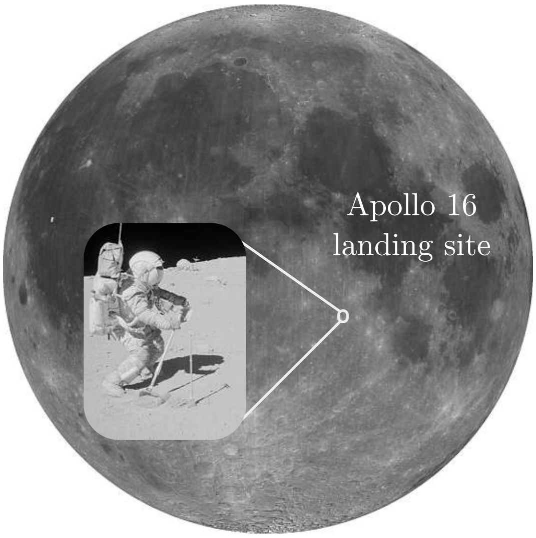

Figure 6.1: Landing site of the Apollo 16 mission on the Moon. Illustration with one of the astronauts collecting lunar material in course of the mission.

Just as in the previous study using pressed pellets from analog material, a characterization of the surface regarding roughness was crucial for meaningful interpretation of the experimental data. Since the applicability of AFM for this purpose has proven itself, it was also utilized for this study. By using the super sharp *SSS-FM* tips from *NANOSENSORS*, it was furthermore possible to overcome the problems with tip artifacts discussed in section 3.2.2. The combined distributions of surface angles from all AFM images obtained (fourteen AFM images of 20 µm × 20 µm in

Table 6.1: Composition of the thin film of lunar material deposited onto a platelet placed next to a QCM during the PLD process and of a pressed mineral pellet. The numbers result from an integration of ToF-E ERDA signals and were evaluated at Uppsala University. Note that Al and Si, Fe and Cr as well as Ca and K could not be separated in ToF-E ERDA and according values were calculated based on [102] (resulting in a negligible K and Cr content).

	abundance [at. %]	
	QCM	Pellet
O	61.0 ± 0.6	58.6 ± 0.6
Si	14.3 ± 0.4	17.0 ± 0.5
Al	9.96 ± 0.4	11.9 ± 0.5
Ca	8.14 ± 0.2	7.26 ± 0.2
Mg	3.27 ± 0.1	3.10 ± 0.1
Fe	2.76 ± 0.1	1.47 ± 0.1
Ti	0.45 ± 0.1	0.18 ± 0.1
C	0.30 ± 0.1	0.31 ± 0.1
N	0.17 ± 0.1	-
H	-	0.23 ± 0.01

total for PLD films and nine for the pellet) are shown for both sample types in figure 6.2 (top). The according values of δ_m including an uncertainty estimation for both QCM and pellet are also given there. Below, 3D visualizations from representative images are given for the QCM on the left and the pellet on the right. All scales are the same in both cases, but the coloring is different for the sake of visibility of structures on the QCM.
14 qcm afm bilder 9 zu pellet

6.2 Experimental- and computational efforts

As in the case of the study using Mercury analogs (chapter 5), sputtering properties of pressed mineral pellets and thin films on QCMs were investigated. Therefore, the same methodology was used, consisting of direct sputter yield measurements from QCM irradiation (see section 3.1.1) and such with the catcher QCM (section 3.1.2). In order to obtain quantitative data which allow for reproduction in different experiments, solely the method including a pre-coating of the catcher was used for this study. Fluences were in the range of 10^{21} ions/m² during a full sweep

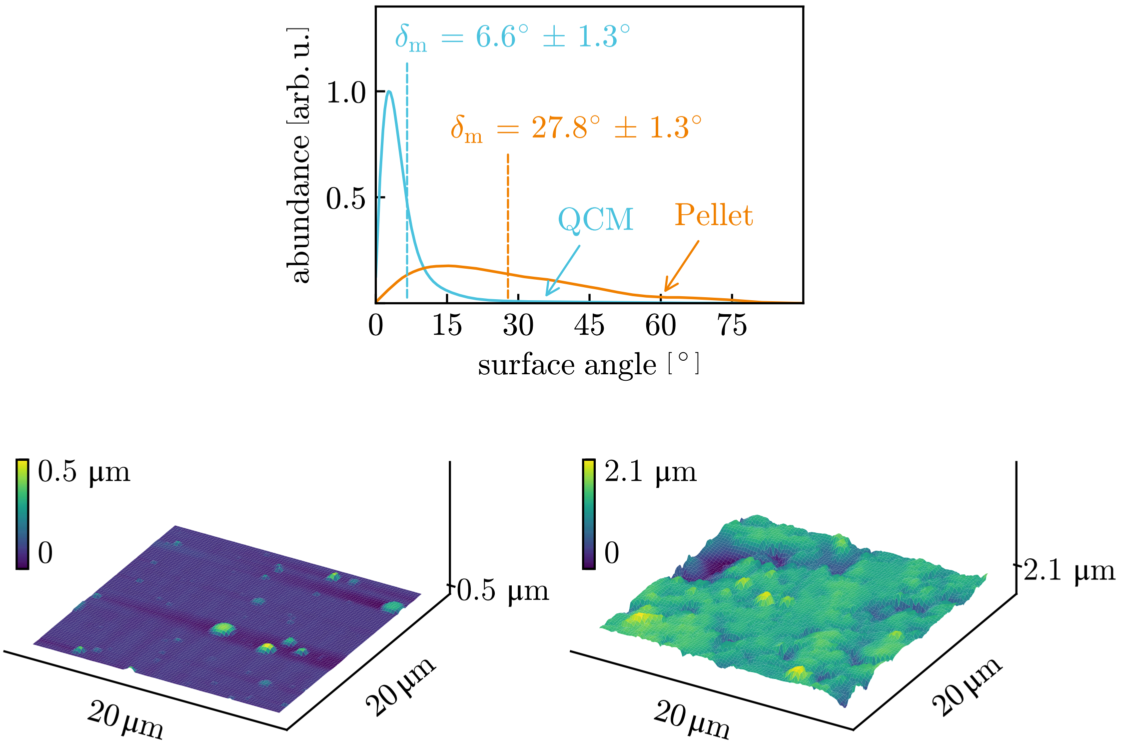

Figure 6.2: **Top:** Combined distributions of the local surface angles of all AFM images for the samples from Apollo 16 material. The δ_m values calculated from all respective images are indicated by arrows with the according numbers being given as well. The QCM (blue) shows the characteristics of a flat sample according to Cupak *et. al* with a value of $\delta_m << 10°$. The pellet (orange), however, has a significantly rougher characteristic.
Bottom: Representative AFM images of the lunar samples. The thin film on a QCM (left) shows only small surface features, while the pressed pellet (right) does posses a very structured surface. Both images have the same scaling but different color-codes in order to visualize also structures on the QCM.

of the catcher angle β.

Regarding computer simulations, the composition as obtained from IBA was used as inputs for SDTrimSP in its 1D and 3D variant. Again, the so-far reliable method of manually adjusting the value of E_{SB} for O to 6.5 eV combined with $isbv = 2$ was used. The materials density was adjusted to the value of $3.1\,\mathrm{g/cm^3}$, which is the recommended value for the specific gravity of the lunar soil from [135]. Due to the higher complexity of the simulation, additional parameters had to be set in SDTrimSP-3D. The voxels were set to have a cubic shape with an edge length of 12.5 nm. With ion ranges of about 33 nm for 4 keV He and 18 nm for 1 keV H^+ for flat samples (according to SDTrimSP), this should be a sufficiently small size to also adequately simulate surface roughness effects [68, 115]. It furthermore allowed to use the whole AFM images with sizes of 20 µm × 20 µm (see section 3.2.2) as inputs regarding the computational resources. Solely simulations including the tilting mechanism with two voxel rows for smoother transitions on the boarders were used to reduce edge artifacts. Reference simulations with a flat topography in SDTrimSP-3D were carried out as well, reproducing the SDTrimSP-1D results within a few percent. Both, SDTrimSP-3D and SPRAY simulations used sets of AFM images from the pellet as inputs, calculating roughness effects for both ion species.

6.3 Results

Thin film sputter yields were obtained with the conventional QCM technique as reference values for the catcher measurements as was done in chapter 5. Since the methodology has proven its reliability with the analog materials, solar wind relevant ion species were used exclusively. Therefore, 2 keV H_2^+ ions – as discussed an appropriate substitution for 1 keV H^+ – and 4 keV He^+ ions were used. The according total sputter yield data for thin films produced from lunar material by PLD are listed in table 6.2.

Table 6.2: Sputter yields for the lunar samples. Yields directly measured using the conventional QCM technique Y_{QCM} for 1 keV H^+ and 4 keV He^+ ions as well as pellet sputter yields Y_{pellet} calculated using equation 3.10 with Y_{QCM} and the ratio r (also given in brackets). The data for 1 keV H^+ was obtained by dividing 2 keV H_2^+ data by a factor of 2.

Sputter yields [amu/ion]

	H	*He*		
α	Y_{QCM}	Y_{QCM}	Y_{pellet}	
0°	0.10 ± 0.02	0.98 ± 0.15	-	
15°	0.16 ± 0.02	1.13 ± 0.18	-	
30°	0.26 ± 0.04	1.58 ± 0.24	-	
45°	0.50 ± 0.08	2.83 ± 0.44	2.6 ± 0.66	(0.93 ± 0.19)
60°	1.18 ± 0.18	5.35 ± 0.83	3.58 ± 0.90	(0.67 ± 0.13)
70°	1.95 ± 0.30	9.36 ± 1.44	-	

For sputter yields of the mineral Moon pellet, measurements with the catcher setup and 4 keV He$^+$ ions were carried out. Under equal conditions, angular distributions of sputtered material $Y_{C,\Omega}$ were obtained from deposition rates at the according positions using equation 3.9. figure 6.3 shows the resulting data for both impact angles $\alpha = 45°$ (left) and 60° (right) as points. Fits of shape $A \cos{(\beta - \zeta)}^n$ (equation 3.12) were added to the data, allowing for better visibility of the angular distributions and a direct integration of those for calculation of r – which is needed for evaluation of equation 3.9. At $\alpha = 45°$, only small differences between the two samples (thin film and pellet) can be seen. When going to 60°, however, a significant gap emerges, as the integrated signal $Y_{C,\Omega}$ increases only by 27% for the pellet but 74% for the QCM sample.
The resulting sputter yields of the mineral pellet Y_{pellet} calculated according to equation 3.10 with the reference values Y_{QCM} and the ratio r from the integrals of the fitted distributions are listed in table 6.2.

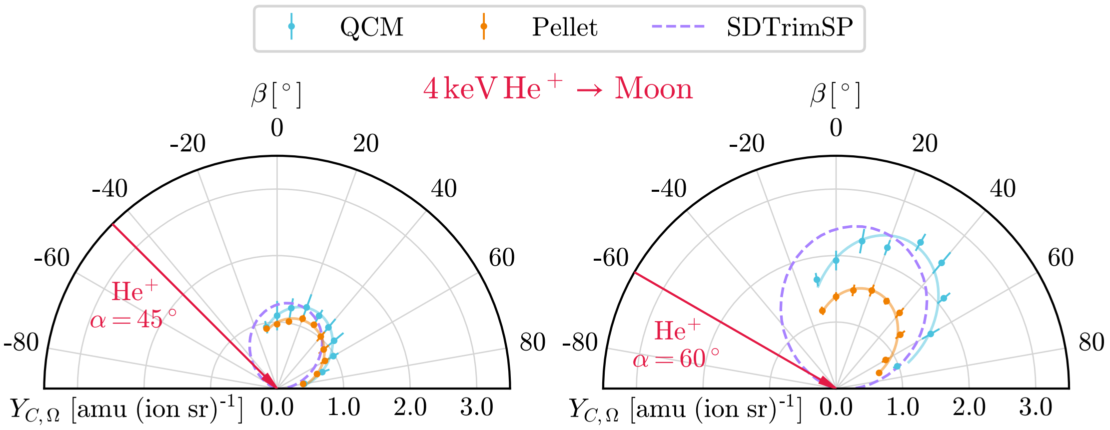

Figure 6.3: Signal $Y_{C,\Omega}$ at the catcher in dependence on the detection angle β for experiments with the lunar sample and 4 keV He$^+$ ions. Data for irradiations of the pellet (orange points) and the QCM (blue points) are shown for the impact angles $\alpha = 45°$ (left) and $\alpha = 60°$ (right). Fit functions of the shape $A \cos{(\beta - \zeta)}^n$ are added to the data as lines in the according colors. In addition, fits with the same function are also shown for SDTrimSP results of the sputtered material in the same angle as covered by the sensitive catcher area scaled to the experimental data and shown as dashed purple lines.

Regarding computer simulations, results for the flat samples (SDTrimSP in its 1D variant) and those with AFM images as inputs (SPRAY and SDTrimSP-3D) are grouped by the two projectiles used and listed accordingly: In table 6.3, sputter yields for 1 keV H^+ are listed, whereas 4 keV He^+ simulations can be found in table 6.4. The ratio between SDTrimSP 1D and the simulations including roughness is given in the brackets. Differences between the two approaches including roughness – mapping 1D BCA data on topography with SPRAY and directly simulating 3D structures with BCA methods – deliver almost exactly the same outcomes.

Table 6.3: Simulated sputter yields of 1 keV H^+ for flat samples with SDTrimSP and with AFM images as input using the SPRAY code and SDTrimSP-3D – representing the rough pellet sample. The ratios between flat and rough surface results are given in the brackets.

Simulated sputter yields: 1 keV H [amu/ion]

α	*SDTrimSP*	*SPRAY*		*SDTrimSP-3D*	
0°	0.25	0.36 ± 0.01	(1.42)	0.38 ± 0.01	(1.50)
15°	0.28	0.39 ± 0.02	(1.40)	0.40 ± 0.01	(1.42)
30°	0.38	0.47 ± 0.02	(1.24)	0.46 ± 0.02	(1.21)
45°	0.60	0.60 ± 0.02	(1.00)	0.58 ± 0.03	(0.97)
60°	1.08	0.77 ± 0.05	(0.72)	0.81 ± 0.06	(0.75)
75°	2.32	1.09 ± 0.13	(0.47)	1.21 ± 0.11	(0.52)

Table 6.4: Simulated sputter yields of 4 keV He^+ for flat samples with SDTrimSP and with AFM images as input using the SPRAY code and SDTrimSP-3D – representing the rough pellet sample. The ratios between flat and rough surface results are given in the brackets.

Simulated sputter yields: 4 keV He [amu/ion]

α	*SDTrimSP*	*SPRAY*		*SDTrimSP-3D*	
0°	1.72	2.52 ± 0.10	(1.47)	2.81 ± 0.08	(1.64)
15°	1.87	2.77 ± 0.12	(1.48)	2.99 ± 0.07	(1.60)
30°	2.68	3.32 ± 0.14	(1.24)	3.45 ± 0.07	(1.29)
45°	4.15	4.27 ± 0.10	(1.03)	4.39 ± 0.15	(1.06)
60°	7.42	5.40 ± 0.29	(0.73)	6.03 ± 0.36	(0.81)
75°	15.65	7.38 ± 0.87	(0.47)	8.60 ± 0.71	(0.55)

All sputter yield data from experiments and simulations are compiled in figure 6.4, with 1 keV H^+ on the left and 4 keV He^+ on the right. Here, good overall agreement for the flat cases – QCM data (blue points) and and SDTrimSP (blue lines) – for both projectiles, can be seen – albeit the simulations being systematically above the experiments.

This difference for the flat simulations is also passed on to both SPRAY (orange dashed line) and SDTrimSP-3D (pink dotted line) simulations. That is the case, since SPRAY uses SDTrimSP as input and SDTrimSP-3D reproduces the 1D results when running without structure inputs. Taking the flat simulations' offset into account shows even better agreement between the simulations including surface roughness and the experimental data. This is reflected by the matching r values, listed in tables 6.2 and 6.4, respectively.

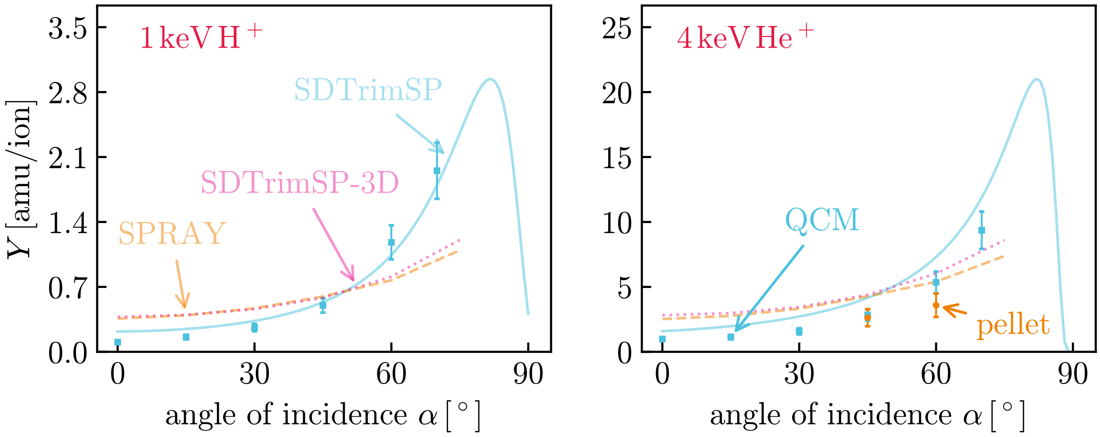

Figure 6.4: Sputter yields of the lunar sample as they are obtained from experiments (points) and simulations (lines) for 1 keV H^+ (left) and 4 keV He^+ (right) irradiations. QCM sputter yields Y_{QCM} represent flat samples and were obtained with the classical QCM technique for sputter yield measurements. The pellet sputter yields Y_{pellet} had to be calculated from catcher data and the reference value of Y_{QCM} using equation 3.10 and are therefore only available for 4 keV He^+. Experimental data for 1 keV H^+ was obtained by dividing data for 2 keV ${H_2}^+$ by a factor of 2. SDTrimSP simulations for flat surfaces are shown as full blue lines, SDTrimSP-3D simulations including the pellet surface structure are depicted as pink dotted line and SPRAY outcomes also including the pellet surface are depicted by dashed orange lines.

6.4 Discussion

Various experiments and simulations of the sputtering of samples returned to Earth by the Apollo 16 mission were carried out. Data was obtained for measurements with QCM techniques for a pressed mineral pellet as well as amorphous thin films on QCMs irradiated with the solar wind proxies H_2^+ and He^+ with energies of 2 keV and 4 keV respectively. Results from computer simulations for the same system allow for an evaluation of influences of surface roughness and therefore also crystallinity – the two remaining differences between the pellet and the thin films. From experience with various thin films produced from minerals by means of PLD it is known, that those have a glassy structure. The pellets, however, have a polycrystalline nature, since they are pressed from mineral powder [102]. Differences in surface morphology add complexity and flat amorphous thin films have to be directly compared to rough, polycrystalline mineral pellets. However, according to IBA, the compositions are matching and only minor differences in the percent range (see table 6.1) are present.

Looking at the data from sputter yield measurements with the conventional QCM technique (table 6.2), good agreement with SDTrimSP results for both projectiles can be seen (tables 6.3 and 6.4), especially when considering that no fitting of parameters was used at all. The signals $Y_{C,\Omega}$ for sputtering of the thin films measured with the catcher (figure 6.3) are also in line with an increase of Y_{QCM} from $\alpha = 45°$ to $\alpha = 60°$. As expected for a rough surface, this increase is much less pronounced for the pellet, where a smoother angular dependence of Y_{pellet} is to be expected.
At the first glance, the simulated pellet sputter yields by both SPRAY and SDTrimSP-3D seem to be too high compared to the experiments. This however can be explained by differences between the simulations of flat surfaces with SDTrimSP – used as inputs for SPRAY and also being reproduced by SDTrimSP-3D for flat surfaces – and the experiments with flat thin films. Accounting for those differences and looking solely at the ratio between Y_{rough} and Y_{flat}, a very good agreement can be seen. The ratios r from the experiment (0.93 for $\alpha = 45°$ and 0.67 for 60° – see table 6.2) and between the simulations (1.03/1.06 and 0.73/0.81 for SPRAY and SDTrimSP-3D, respectively – listed in table 6.4) match very well.
Another remarkable fact can also be found when comparing the two roughness evaluations with each other. Despite the quite different approaches, the resulting sputter yields are almost identical. Such straightforward comparison is however only possible in this special scenario, where the full AFM images could be directly evaluated with SDTrimSP-3D as well. With, e.g., 2 keV Ar^+ ions, much smaller voxel sizes would be required due to the shorter range of the ions. Therefore, the needed number of voxels would increase drastically. Unfortunately, the simulations with 12.5 nm cube length already pushed the computational limits.

6.5 Conclusion

By the combined efforts of conventional- and catcher QCM techniques, quantitative sputter yields for samples returned from the Moon could be measured. The data obtained is in line with the results for amorphous thin films created with PLD from the same material. Discrepancies between the thin film and the pressed mineral pellet in the catcher QCM data can be explained by solely taking the pellet surface morphology into account. Therefore, it could be shown that the assumption of BCA – treating the material as amorphous solid – is valid for the surface of the Moon. This has implications for all studies considering sputtering processes on rocky bodies in space. Regarding needed simulations, the agreement of sputter yields with the BCA code SDTrimSP is good, especially taking into account, that no fitting of parameters was done. Overall, the sputtering of minerals seems to be well described with SDTrimSP, with differences being typically below 50% using the parameters proposed by Szabo *et al.* [30]. In order to apply those results to the regolith covered surfaces of the Moon [2], computer generated structures might be sufficient to capture the differences caused by geometric effects. Such have recently been shown to reproduce the scattering of hydrogen from the solar wind on the lunar regolith with SDTrimSP-3D [115]. This could help to paint a more clear picture on this topic, where only limited studies based on statistical evaluations, e.g., by Cassidy and Johnson [136] or MD simulations with much reduced cell sizes exist so far, even leading to contradictory results [137]. A treatment of regolith sputtering on an adequate scale is therefore still missing in literature.

Another important finding is the perfect agreement for the prediction of roughness effects for the full BCA code SDTrimSP-3D – calculating trajectories of the ions in the amorphous solid made up from volume elements – and SPRAY, which only maps sputtering information from flat samples on the triangulated surfaces. This agreement shows, that the underlying assumption of solely geometrical effects on the sputter yield is also validated by SDTrimSP-3D. Of course, this conclusion is limited to ion species and structure sizes comparable to this study, where effects as transmission sputtering between structural features do not need to be taken into account.

7 Conclusion and Outlook

The impingement of solar wind ions onto the surfaces of rocky celestial bodies causes a variety of different effects. In this thesis, fundamental processes that occur when representative materials for the surfaces of the Moon or the planet Mercury are irradiated by solar wind ions were investigated. Protons and alpha particles, as they make up almost 100% of the solar wind at an approximate velocity of 1 keV per nucleon, penetrate some tens of nanometers into the used minerals. Therefore, the ions can get implanted in a certain depth and an equilibrium of implantation and release is formed after a certain ion fluence. Furthermore, sputtering of material due to the ions kinetic energy causes a continuous erosion of the surface. The exact characteristics of the sputtering process can depend on many parameters, like projectile energies, impact angle of the ions and even the crystal structure of the irradiated samples. However, a rigorous comparison of sputtering of crystalline phases compared to amorphous ones has so far not been conducted for minerals serving as analogs for rocky celestial bodies. In order to investigate both, the implantation of solar wind and the sputtering caused for rocky surfaces, silicate minerals were studied extensively in laboratory experiments and by means of computer simulations.

Implantation of ions upon impact and sputtering of sample material are two competing processes when it comes to the mass change of a sample during ion irradiations. While implantation leads to an increase due to the insertion of mass, sputtering reduces the material present on a sample. However, both effects can happen simultaneously upon ion impacts. The direct QCM technique utilized during almost all experiments conducted in the course of this thesis allows to obtain the net mass change caused by the sum of implantation and sputtering. This was used to obtain a precise value for the saturation fluence for irradiations of the iron and magnesium rich pyroxene *augite* ($(\text{Ca,Mg,Fe})_2[\text{Si}_2\text{O}_6]$) with 4 keV He^+ ions [76]. With it's high sensitivity, the QCM technique allowed to investigate transient effects caused by a variable flux of projectiles out of the sample up to a fluence of about $2.2 \times 10^{21}\ {}^{\text{ions}}/_{\text{m}^2}$. After that fluence, a steady state in mass change per impinging ion was found. Furthermore, it was possible to determine He concentrations from the integrated mass change measured with the QCM. The necessary constraints for the depth of the He in the sample and a negligible fluence dependence of the sputter yield were obtained from comparison with literature [122] and SDTrimSP simulations respectively.
In addition, a combination with TDS measurements of the saturated samples allowed to investigate the mobility of the implanted He at elevated temperatures.

Again, by determining the total mass change during TDS by means of the QCM technique showed, that heating the sample to 530 K is sufficient to remove all He. It could thereby be seen, that, e.g., typical surface temperatures on the day-side of Mercury of up to 700 K are sufficient to release all He – at least for the investigated analog mineral. In addition to investigations on the volatility of implanted He, extensive sputter yield measurements were carried out, validating parameters for SDTrimSP proposed by Szabo *et al.* for the silicate wollastonite ($CaSiO_3$) [30]. Again, dynamics in the mass change rate were observed for samples already in a saturated state, which is also attributed to the high mobility of He in the sample. Nevertheless, excellent agreement between simulations and experiments were found in the steady state, showing a broader applicability of the settings found by Szabo *et al.*.

The conventional QCM technique is restricted with regard to the types of samples that can be utilized, since the desired material has to be deposited onto quartz resonators as a thin film. Since deposition parameters are restricted by the quartz substrate and its phase transition at 847 K [73, 81], mineral samples with their specific crystal structure can hardly be manufactured on a quartz resonator as a substrate. It was therefore necessary to use a different approach to study the sputtering of crystalline samples. For this purpose, a method introduced by Berger *et al.* including a second QCM was used as basis for a new setup [84]. By placing a so-called catcher QCM on a rotary manipulator, it was possible to probe angular distributions of sputtered material from irradiations of various types of samples. Thereby, deposition rates for different material phases can be directly compared and the integrated angular distribution can be used to calculate the ratio of the according sputter yields. When an amorphous thin film on a QCM as a reference and a bulky sample with specific crystallinity and the same stoichiometry are compared this way, an evaluation of the bulky samples' sputter yield becomes possible as well.

By means of the new catcher QCM setup, sputtering properties like yield and angular distributions of ejecta could be studied for the planetary analog minerals wollastonite and enstatite ($MgSiO_3$). For this purpose, the amorphous thin films on QCMs typically used for sputter yield measurements for planetary analogs (cf. [29, 30, 76, 80]) and mineral pellets were irradiated with ion beams [83]. Since the latter ones were produced by pressing mortared single crystals into stainless steel holders, they represented polycrystalline samples [82]. In the case of wollastonite, solely Ar^+ ions with a kinetic energy of 2 keV were used. In that model system, no differences between the angular distributions of the amorphous QCM based samples and the pressed pellets could be observed. For enstatite, 4 keV He^+ ions were used as well, mimicking the interaction with the solar wind. In contrast to the wollastonite samples, clear deviations in the signals could be seen in all investigated scenarios (i.e., for both ion species and impact angles of 45° and 60°). However, those could be explained by calculating the effects of surface roughness for the pellets using the ray-tracing code SPRAY [41] with AFM images and BCA simulations of the flat samples as inputs. Therefore, no effects of the crystal structure could be observed when comparing amorphous thin films to polycrystalline samples. A reason for this observation – which is contrary to the results of a recent study by Schlueter *et al.* for irradiations of tungsten [37] – might be found in the amorphization of the mineral samples upon ion impact. Fluences in the experiments were in the range of $10^{21}\ \mathrm{ions}/\mathrm{m}^2$ for single measurement series, where the crystal structure is expected to be lost already. In contrast to metal samples, however, this damage does not heal for silicate mineral samples (see e.g. [125, 129]). In the context of sputtering of celestial bodies, this has significant implications. Since the fluences applied in the experiments are reached within a few hundreds of years on Mercury, a similar situation as in the experiment can be assumed [22]. This also further justifies the use of BCA codes for sputter yield calculation, where amorphous samples are assumed as well. In addition to the findings on crystal structure, the importance of taking surface roughness into account when investigating the sputtering of planets by solar wind ions was shown. A drastic reduction of the sputter yields especially for grazing ion incidence could be seen, even for a compactly pressed surface from mineral powder.

In a similar manner, sputtering of a sample returned from the Moon by the NASA Apollo 16 mission was investigated. Measurements of the sputter yield by means of the conventional QCM technique under irradiations with 4 keV He^+ as well as with 2 keV $\mathrm{H_2}^+$ ions for various impact angles again revealed good agreement of SDTrimSP with adapted parameters and the experiments. With those reference values, sputter yields for pressed mineral pellets could be obtained for the Lunar samples as well. For this purpose, the same methodology as for enstatite and wollastonite samples was used, probing the angular distributions of sputtered particles with the catcher QCM and scaling the sputter yields obtained with the conventional QCM by the integrals of those distributions. Just as for the much simpler enstatite system – consisting of only one mineral species – a reduction in sputter yield for the investigated impact angles of 45° and 60° was found for the mineral samples. Again, this reduction can be explained by surface roughness alone. In order to come to this conclusion, not only the SPRAY code was used for this study, but also SDTrimSP-3D, which directly calculates the interaction of ions with textured surfaces. In both cases, AFM images of the pellet surface were used as inputs, together with equal BCA parameters (for the BCA input data needed in SPRAY and for SDTrimSP-3D). The use of both codes also allowed the first rigorous comparison between the two approaches. It revealed a perfect agreement not only with the experiment, but also between the two codes – validating the assumptions made for the use of the SPRAY code in the first place. The sputter yields measured for the Lunar sample show, that BCA codes are able to describe sputtering for complex systems as well, as long as adequate input parameters are used. The settings proposed by Szabo *et al.* used for all simulations during this thesis have been proven to be such a set of parameters not only for silicate minerals, but also for real Lunar material. Future studies, however, should deal with the real structure of celestial bodies' surfaces, since the regolith covering them can significantly impact the way ions interact, as was also shown recently [115].

Bibliography

[1] Pieters C.M. and Noble S.K., "Space weathering on airless bodies", *Journal of Geophysical Research: Planets*, **121**, 1865 (2016)

[2] McKay D.S., Heiken G., Basu A., Blanford G., Simon S., Reedy R., French B.M. and Papike J., "The lunar regolith", *Lunar sourcebook*, **567**, 285 (1991)

[3] Hapke B., "Space weathering from Mercury to the asteroid belt", *Journal of Geophysical Research: Planets*, **106**, 10039 (2001)

[4] Meyer-Vernet N., *Basics of the solar wind*, Cambridge University Press (2007)

[5] Bauch K.E., Hiesinger H., Greenhagen B.T. and Helbert J., "Estimation of surface temperatures on Mercury in preparation of the MERTIS experiment onboard BepiColombo", *Icarus*, **354**, 114083 (2021)

[6] Madey T.E., Yakshinskiy B., Ageev V. and Johnson R., "Desorption of alkali atoms and ions from oxide surfaces: Relevance to origins of Na and K in atmospheres of Mercury and the Moon", *Journal of Geophysical Research: Planets*, **103**, 5873 (1998)

[7] Wurz P., Fatemi S., Galli A., Halekas J., Harada Y., Jäggi N., Jasinski J., Lammer H., Lindsay S., Nishino M. *et al.*, "Particles and Photons as Drivers for Particle Release from the Surfaces of the Moon and Mercury", *Space science reviews*, **218**, 1 (2022)

[8] Bame S., Asbridge J., Feldman W., Montgomery M. and Kearney P., "Solar wind heavy ion abundances", *Solar Physics*, **43**, 463 (1975)

[9] Feldman U., Landi E. and Schwadron N., "On the sources of fast and slow solar wind", *Journal of Geophysical Research: Space Physics*, **110** (2005)

[10] Zhu C., Crandall P.B., Gillis-Davis J.J., Ishii H.A., Bradley J.P., Corley L.M. and Kaiser R.I., "Untangling the formation and liberation of water in the lunar regolith", *Proceedings of the National Academy of Sciences*, **116**, 11165 (2019)

[11] Lyon J.G., "The solar wind-magnetosphere-ionosphere system", *Science*, **288**, 1987 (2000)

[12] Lundin R., Lammer H. and Ribas I., "Planetary magnetic fields and solar forcing: implications for atmospheric evolution", *Space Science Reviews*, **129**, 245 (2007)

[13] Fang X., Liemohn M.W., Nagy A.F., Luhmann J.G. and Ma Y., "Escape probability of Martian atmospheric ions: Controlling effects of the electromagnetic fields", *Journal of Geophysical Research: Space Physics*, **115** (2010)

[14] Carr M.H. and Wänke H., "Earth and Mars: Water inventories as clues to accretional histories", *Icarus*, **98**, 61 (1992)

[15] Nenon Q., Poppe A.R., Rahmati A., Lee C.O., McFadden J.P. and Fowler C.M., "Phobos surface sputtering as inferred from MAVEN ion observations", *Journal of Geophysical Research: Planets*, **124**, 3385 (2019)

[16] Szabo P.S., Biber H., Jäggi N., Wappl M., Stadlmayr R., Primetzhofer D., Nenning A., Mutzke A., Fleig J., Mezger K., Lammer H., Galli A., Wurz P. and Aumayr F., "Experimental insights into space weathering of phobos: laboratory investigation of sputtering by atomic and molecular planetary ions", *Journal of Geophysical Research: Planets*, **125**, e2020JE006583 (2020)

[17] Keller L.P. and McKay D.S., "The nature and origin of rims on lunar soil grains", *Geochimica et Cosmochimica Acta*, **61**, 2331 (1997)

[18] Schaible M.J. and Baragiola R.A., "Hydrogen implantation in silicates: The role of solar wind in SiOH bond formation on the surfaces of airless bodies in space", *Journal of Geophysical Research: Planets*, **119**, 2017 (2014)

[19] Jones B.M., Aleksandrov A., Hibbitts K., Dyar M. and Orlando T.M., "Solar wind-induced water cycle on the Moon", *Geophysical Research Letters*, **45**, 10 (2018)

[20] Xu Y., Tian H.C., Zhang C., Chaussidon M., Lin Y., Hao J., Li R., Gu L., Yang W., Huang L. *et al.*, "High abundance of solar wind-derived water in lunar soils from the middle latitude", *Proceedings of the National Academy of Sciences*, **119**, e2214395119 (2022)

[21] Behrisch R. and Eckstein W., *Sputtering by Particle Bombardment: Experiments and Computer Calculations from Threshold to MeV Energies*, Springer Science & Business Media (2007)

[22] Wurz P., Whitby J., Rohner U., Martín-Fernández J., Lammer H. and Kolb C., “Self-consistent modelling of Mercury’s exosphere by sputtering, micrometeorite impact and photon-stimulated desorption”, *Planetary and Space Science*, **58**, 1599 (2010)

[23] Hofsäss H. and Stegmaier A., “Binary collision approximation simulations of ion solid interaction without the concept of surface binding energies”, *Nuclear Instruments and Methods in Physics Research Section B: Beam Interactions with Materials and Atoms*, **517**, 49 (2022)

[24] Potter A. and Morgan T., “Discovery of sodium in the atmosphere of Mercury”, *Science*, **229**, 651 (1985)

[25] Benkhoff J., Van Casteren J., Hayakawa H., Fujimoto M., Laakso H., Novara M., Ferri P., Middleton H.R. and Ziethe R., “BepiColombo—Comprehensive exploration of Mercury: Mission overview and science goals”, *Planetary and Space Science*, **58**, 2 (2010)

[26] McCoy T.J., Peplowski P.N., McCubbin F.M. and Weider S.Z., “The geochemical and mineralogical diversity of Mercury”, *Mercury. The View after MESSENGER. Edited by Sean C. Solomon*, 176–190 (2018)

[27] Ziegler J.F., Ziegler M.D. and Biersack J.P., “SRIM: The stopping and range of ions in matter (2010)”, *Nuclear Instruments and Methods in Physics Research Section B: Beam Interactions with Materials and Atoms*, **268**, 1818 (2010)

[28] Hofsäss H., Zhang K. and Mutzke A., “Simulation of ion beam sputtering with SDTrimSP, TRIDYN and SRIM”, *Applied Surface Science*, **310**, 134 (2014)

[29] Szabo P.S., Chiba R., Biber H., Stadlmayr R., Berger B.M., Mayer D., Mutzke A., Doppler M., Sauer M., Appenroth J., Fleig J., Foelske-Schmitz A., Hutter H., Mezger K., Lammer H., Galli A., Wurz P. and Aumayr F., “Solar wind sputtering of wollastonite as a lunar analogue material–Comparisons between experiments and simulations”, *Icarus*, **314**, 98 (2018)

[30] Szabo P.S., Biber H., Jäggi N., Brenner M., Weichselbaum D., Niggas A., Stadlmayr R., Primetzhofer D., Nenning A., Mutzke A., Sauer M., Fleig J., Foelske-Schmitz A., Mezger K., Lammer H., Galli A., Wurz P. and Aumayr F., “Dynamic potential sputtering of lunar analog material by solar wind ions”, *The Astrophysical Journal*, **891**, 100 (2020)

[31] Larson L.A., Williams J.M. and Current M.I., "Ion implantation for semiconductor doping and materials modification", *Reviews Of Accelerator Science And Technology: Volume 4: Accelerator Applications in Industry and the Environment*, 11–40 (2011)

[32] Causey R.A., "Hydrogen isotope retention and recycling in fusion reactor plasma-facing components", *Journal of Nuclear Materials*, **300**, 91 (2002)

[33] Urbassek H.M., *Sputtering Theory*, volume 52, The Royal Danish Academy of Sciences and Letters (2006)

[34] Sigmund P., "Theory of sputtering. I. Sputtering yield of amorphous and polycrystalline targets", *Physical Review*, **184**, 383 (1969)

[35] Nordlund K., Djurabekova F. and Hobler G., "Large fraction of crystal directions leads to ion channeling", *Physical Review B*, **94**, 214109 (2016)

[36] Fluit J., Rol P. and Kistemaker J., "Angular-Dependent Sputtering of Copper Single Crystals", *Journal of Applied Physics*, **34**, 690 (1963)

[37] Schlueter K., Nordlund K., Hobler G., Balden M., Granberg F., Flinck O., Da Silva T. and Neu R., "Absence of a crystal direction regime in which sputtering corresponds to amorphous material", *Physical review letters*, **125**, 225502 (2020)

[38] Sigmund P., "Recollections of fifty years with sputtering", *Thin Solid Films*, **520**, 6031 (2012)

[39] Küstner M., Eckstein W., Dose V. and Roth J., "The influence of surface roughness on the angular dependence of the sputter yield", *Nuclear Instruments and Methods in Physics Research Section B: Beam Interactions with Materials and Atoms*, **145**, 320 (1998)

[40] Küstner M., Eckstein W., Hechtl E. and Roth J., "Angular dependence of the sputtering yield of rough beryllium surfaces", *Journal of Nuclear Materials*, **265**, 22 (1999)

[41] Cupak C., Szabo P., Biber H., Stadlmayr R., Grave C., Fellinger M., Brötzner J., Wilhelm R., Möller W., Mutzke A., Moro M. and Aumayr F., "Sputter yields of rough surfaces: Importance of the mean surface inclination angle from nano-to microscopic rough regimes", *Applied Surface Science*, **570**, 151204 (2021)

[42] Szabo P.S., Cupak C., Biber H., Jäggi N., Galli A., Wurz P. and Aumayr F., "Analytical model for the sputtering of rough surfaces", *Surfaces and Interfaces*, **30**, 101924 (2022)

[43] Baldwin M. and Doerner R., "Formation of helium induced nanostructure 'fuzz'on various tungsten grades", *Journal of Nuclear Materials*, **404**, 165 (2010)

[44] Stadlmayr R., Szabo P., Mayer D., Cupak C., Dittmar T., Bischoff L., Möller S., Rasiński M., Wilhelm R., Möller W. and Aumayr F., "Sputtering of nanostructured tungsten and comparison to modelling with TRI3DYN", *Journal of Nuclear Materials*, **532**, 152019 (2020)

[45] Sporn M., Libiseller G., Neidhart T., Schmid M., Aumayr F., Winter H., Varga P., Grether M., Niemann D. and Stolterfoht N., "Potential sputtering of clean SiO 2 by slow highly charged ions", *Physical review letters*, **79**, 945 (1997)

[46] Schwestka J., Inani H., Tripathi M., Niggas A., McEvoy N., Libisch F., Aumayr F., Kotakoski J. and Wilhelm R.A., "Atomic-Scale Carving of Nanopores into a van der Waals Heterostructure with Slow Highly Charged Ions", *ACS nano*, **14**, 10536 (2020)

[47] Niggas A., Creutzburg S., Schwestka J., Wöckinger B., Gupta T., Grande P.L., Eder D., Marques J.P., Bayer B.C., Aumayr F. *et al.*, "Peeling graphite layer by layer reveals the charge exchange dynamics of ions inside a solid", *Communications Physics*, **4**, 1 (2021)

[48] Aumayr F. and Winter H., "Potential sputtering", *Philosophical Transactions of the Royal Society of London. Series A: Mathematical, Physical and Engineering Sciences*, **362**, 77 (2004)

[49] Labanda J., Barnett S. and Hultman L., "Sputter cleaning and smoothening of GaAs (001) using glancing-angle ion bombardment", *Applied physics letters*, **66**, 3114 (1995)

[50] Sigmund P., "Sputtering of single and multiple component materials", *Journal of Vacuum Science and Technology*, **17**, 396 (1980)

[51] Eckstein W., "Oscillations of sputtering yield", *Nuclear Instruments and Methods in Physics Research Section B: Beam Interactions with Materials and Atoms*, **171**, 435 (2000)

[52] Hayderer G., Cernusca S., Schmid M., Varga P., Winter H., Aumayr F., Niemann D., Hoffmann V., Stolterfoht N. and Lemell C., “Kinetically assisted potential sputtering of insulators by highly charged ions”, *Physical Review Letters*, **86**, 3530 (2001)

[53] Pelaz L., Marqués L.A. and Barbolla J., “Ion-beam-induced amorphization and recrystallization in silicon”, *Journal of applied physics*, **96**, 5947 (2004)

[54] Hirata A., Tokura H. and Yoshikawa M., “Smoothing of chemically vapour deposited diamond films by ion beam irradiation”, *Thin Solid Films*, **212**, 43 (1992)

[55] Ziberi B., Frost F., Höche T. and Rauschenbach B., “Ripple pattern formation on silicon surfaces by low-energy ion-beam erosion: Experiment and theory”, *Physical Review B*, **72**, 235310 (2005)

[56] Wagner M., Mayer M., von Toussaint U. and Mutzke A., “Simulation of the evolution of rough surfaces by sputtering using the binary collision approximation”, *Radiation Effects and Defects in Solids*, **177**, 1019 (2022)

[57] Stadlmayr R., Szabo P., Berger B., Cupak C., Chiba R., Blöch D., Mayer D., Stechauner B., Sauer M., Foelske-Schmitz A., Oberkofler M., Schwarz-Selinger T., Mutzke A. and Aumayr F., “Fluence dependent changes of surface morphology and sputtering yield of iron: comparison of experiments with SDTrimSP-2D”, *Nuclear Instruments and Methods in Physics Research Section B: Beam Interactions with Materials and Atoms*, **430**, 42 (2018)

[58] Kroese D.P. and Rubinstein R.Y., “Monte carlo methods”, *Wiley Interdisciplinary Reviews: Computational Statistics*, **4**, 48 (2012)

[59] Robinson M.T. and Torrens I.M., “Computer simulation of atomic-displacement cascades in solids in the binary-collision approximation”, *Physical Review B*, **9**, 5008 (1974)

[60] Eckstein W., “The Binary Collision Model”, in *Computer Simulation of Ion-Solid Interactions*, 4–32, Springer (1991)

[61] Yamamoto S., “Fundamental physics of vacuum electron sources”, *Reports on Progress in Physics*, **69**, 181 (2005)

[62] Kelly R., “The surface binding energy in slow collisional sputtering”, *Nuclear Instruments and Methods in Physics Research Section B: Beam Interactions with Materials and Atoms*, **18**, 388 (1986)

[63] Ziegler J.F. and Biersack J.P., "The stopping and range of ions in matter", in *Treatise on heavy-ion science*, 93–129, Springer (1985)

[64] Shulga V., "Note on the artefacts in SRIM simulation of sputtering", *Applied Surface Science*, **439**, 456 (2018)

[65] Mutzke A., Schneider R., Eckstein W., Dohmen R., Schmid K., Toussaint U.v. and Badelow G., "SDTrimSP Version 6.00", *IPP Report 2019-02* (2019)

[66] Mutzke A., Schneider R. and Bandelow G., "SDTrimSP-2D: Simulation of Particles Bombarding on a Two Dimensional Target-Version 2.0", *IPP Report 12/11* (2013)

[67] Möller W., "TRI3DYN–Collisional computer simulation of the dynamic evolution of 3-dimensional nanostructures under ion irradiation", *Nuclear Instruments and Methods in Physics Research Section B: Beam Interactions with Materials and Atoms*, **322**, 23 (2014)

[68] Von Toussaint U., Mutzke A. and Manhard A., "Sputtering of rough surfaces: a 3D simulation study", *Physica Scripta*, **2017**, 014056 (2017)

[69] Speight R.E. and Cooper M.A., "A survey of the 2010 quartz crystal microbalance literature", *Journal of Molecular Recognition*, **25**, 451 (2012)

[70] Sauerbrey G., "Verwendung von Schwingquarzen zur Wägung dünner Schichten und zur MikrowÃ€gung", *Zeitschrift für Physik*, **155**, 206 (1959)

[71] Hayderer G., Schmid M., Varga P., Winter H.P., Aumayr F., Wirtz L., Lemell C., Burgdörfer J., Hägg L. and Reinhold C.O., "Threshold for Potential Sputtering of LiF", *Physical Review Letters*, **83**, 3948 (1999)

[72] Golczewski A., Dobes K., Wachter G., Schmid M. and Aumayr F., "A quartz-crystal-microbalance technique to investigate ion-induced erosion of fusion relevant surfaces", *Nuclear Instruments and Methods in Physics Research Section B: Beam Interactions with Materials and Atoms*, **267**, 695 (2009)

[73] Stadlmayr R., Szabo P.S., Biber H., Koslowski H.R., Kadletz E., Cupak C., Wilhelm R.A., Schmid M., Linsmeier C. and Aumayr F., "A high temperature dual-mode quartz crystal microbalance technique for erosion and thermal desorption spectroscopy measurements", *Review of Scientific Instruments*, **91**, 125104 (2020)

[74] Berger B.M., Stadlmayr R., Blöch D., Gruber E., Sugiyama K., Schwarz-Selinger T. and Aumayr F., "Erosion of Fe-W model system under normal and oblige D ion irradiation", *Nuclear Materials and Energy*, **12**, 468 (2017)

[75] Hayderer G., Schmid M., Varga P., Winter H. and Aumayr F., “A highly sensitive quartz-crystal microbalance for sputtering investigations in slow ion–surface collisions”, *Review of Scientific Instruments*, **70**, 3696 (1999)

[76] Biber H., Szabo P.S., Jäggi N., Wallner M., Stadlmayr R., Moro M.V., Nenning A., Mutzke A., Mezger K., Lammer H., Primetzhofer D., Fleig J., Galli A., Wurz P. and Aumayr F., “Solar wind Helium ion interaction with Mg and Fe rich pyroxene as Mercury surface analogue”, *Nuclear Instruments and Methods in Physics Research Section B: Beam Interactions with Materials and Atoms*, **480**, 10 (2020)

[77] Savitzky A. and Golay M.J., “Smoothing and differentiation of data by simplified least squares procedures”, *Analytical chemistry*, **36**, 1627 (1964)

[78] Schmid M., Rath D. and Diebold U., “Why and How Savitzky–Golay Filters Should Be Replaced”, *ACS measurement science Au*, **2**, 185 (2022)

[79] Neubig B. and Briese W., *Das grosse Quarz-Kochbuch: Quarze, Quarzoszillatoren, Quarz-und Oberflächenwellenfilter (SAW), Messtechnik; mit 23 Tabellen*, Franzis Feldkirchen, Austria (1997)

[80] Hijazi H., Bannister M.E., Meyer III H., Rouleau C.M. and Meyer F.W., “Kinetic and potential sputtering of an anorthite-like glassy thin film”, *Journal of Geophysical Research: Planets*, **122**, 1597 (2017)

[81] Coe R.S. and Paterson M.S., “The α–β inversion in quartz: a coherent phase transition under nonhydrostatic stress”, *Journal of Geophysical Research*, **74**, 4921 (1969)

[82] Jäggi N., Galli A., Wurz P., Biber H., Szabo P.S., Brötzner J., Aumayr F., Tollan P.M.E. and Mezger K., “Creation of Lunar and Hermean analogue mineral powder samples for solar wind irradiation experiments and mid-infrared spectra analysis”, *Icarus*, **365**, 114492 (2021)

[83] Biber H., Brötzner J., Jäggi N., Szabo P.S., Pichler J., Cupak C., Voith C., Cserveny B., Nenning A., Mutzke A., Moro M.V., Primetzhofer D., Mezger K., Galli A., Wurz P. and Aumayr F., “Sputtering Behavior of Rough, Polycrystalline Mercury Analogs”, *The Planetary Science Journal*, **3**, 271 (2022)

[84] Berger B.M., Szabo P.S., Stadlmayr R. and Aumayr F., “Sputtering measurements using a quartz crystal microbalance as a catcher”, *Nuclear Instruments and Methods in Physics Research Section B: Beam Interactions with Materials and Atoms*, **406**, 533 (2017)

[85] Cupak C., "Influence of Roughness on Sputter Yields of Tungsten-Coatings relevant for Nuclear Fusion Devices", Masters thesis, TU Wien (2019)

[86] Szabo P.S., "Experimental and Simulated Sputtering of Gold, Iron and Wollastonite with a Catcher-QCM Setup", Masters thesis, TU Wien (2015)

[87] Feder R., Bundesmann C., Neumann H. and Rauschenbach B., "Ion beam sputtering of germanium–Energy and angular distribution of sputtered and scattered particles", *Nuclear Instruments and Methods in Physics Research Section B: Beam Interactions with Materials and Atoms*, **334**, 88 (2014)

[88] Woodruff D.P., *Modern techniques of surface science*, Cambridge university press (2016)

[89] Anderl R., Causey R., Davis J., Doerner R., Federici G., Haasz A., Longhurst G., Wampler W. and Wilson K., "Hydrogen isotope retention in beryllium for tokamak plasma-facing applications", *Journal of nuclear materials*, **273**, 1 (1999)

[90] Reinelt M., Allouche A., Oberkofler M. and Linsmeier C., "Retention mechanisms and binding states of deuterium implanted into beryllium", *New Journal of Physics*, **11**, 043023 (2009)

[91] Galutschek E., Trassl R., Salzborn E., Aumayr F. and Winter H., "Compact 14.5 GHz all-permanent magnet ECRIS for experiments with slow multicharged ions", *Journal of Physics: Conference Series*, **58**, 395 (2007)

[92] Brötzner J., "An Optimised Catcher-QCM Setup to Study the Sputtering of Lunar and Hermean Surface Regolith Analogues", Masters thesis, TU Wien (2022)

[93] Berger B., "Laboratory work on plasma-wall-interaction processes relevant for fusion experiments", Ph.D. thesis, TU Wien ((2017)), unpublished

[94] Stadlmayr R., "Erosion of fusion relevant materials-experiments and modelling", Ph.D. thesis, Wien (2020)

[95] Harland D.M., *Exploring the moon: the Apollo Expeditions*, Springer Science & Business Media (1999)

[96] Lunar and Institute P., "Apollo 16 Lunar Samples", `https://www.lpi.usra.edu/lunar/missions/apollo/apollo_16/samples/` (2022), [Online; accessed 15-September-2022]

[97] Groenen R., Smit J., Orsel K., Vailionis A., Bastiaens B., Huijben M., Boller K., Rijnders G. and Koster G., “Research Update: Stoichiometry controlled oxide thin film growth by pulsed laser deposition”, *APL materials*, **3**, 070701 (2015)

[98] Chu W., Mayer J. and Nicolet M., *Backscattering Spectrometry*, Academic Press (1978)

[99] Amsel G., “CUTBA (cleaning up the tower of Babel of acronyms) in IBA”, *Nuclear Instruments and Methods in Physics Research Section B: Beam Interactions with Materials and Atoms*, **118**, 52 (1996)

[100] Yasuda K., “Time-Of-Flight ERDA for Depth Profiling of Light Elements”, *Quantum Beam Science*, **4**, 40 (2020)

[101] Moro M.V., Holeňák R., Medina L.Z., Jansson U. and Primetzhofer D., “Accurate high-resolution depth profiling of magnetron sputtered transition metal alloy films containing light species: A multi-method approach”, *Thin Solid Films*, **686**, 137416 (2019)

[102] Bansal B., Church S., Gast P., Hubbard N., Rhodes J. and Wiesmann H., “The chemical composition of soil from the Apollo 16 and Luna 20 sites”, *Earth and Planetary Science Letters*, **17**, 29 (1972)

[103] Taylor S., Gorton M., Muir P., Nance W., Rudowski R. and Ware N., “Composition of the Descartes region, lunar highlands”, *Geochimica et Cosmochimica Acta*, **37**, 2665 (1973)

[104] Korotev R., “Compositional trends in Apollo 16 soils”, in *Lunar and Planetary Science Conference*, volume 12, 565–567 (1981)

[105] Mandelbrot B., “How long is the coast of Britain? Statistical self-similarity and fractional dimension”, *science*, **156**, 636 (1967)

[106] Gołek F., Mazur P., Ryszka Z. and Zuber S., “AFM image artifacts”, *Applied surface science*, **304**, 11 (2014)

[107] Shen J., Zhang D., Zhang F.H. and Gan Y., “AFM tip-sample convolution effects for cylinder protrusions”, *Applied Surface Science*, **422**, 482 (2017)

[108] Urbassek H.M., “Molecular-dynamics simulation of sputtering”, *Nuclear Instruments and Methods in Physics Research Section B: Beam Interactions with Materials and Atoms*, **122**, 427 (1997)

[109] Eckstein W., *Computer Simulation of Ion-Solid Interactions*, Springer Science & Business Media (2013)

[110] Kornich G., Betz G., Zaporojtchenko V., Bazhin A. and Faupel F., “Molecular dynamics simulations of low energy ion sputtering of copper nanodimensional clusters on graphite substrates”, *Nuclear Instruments and Methods in Physics Research Section B: Beam Interactions with Materials and Atoms*, **227**, 261 (2005)

[111] Lopez-Cazalilla A., Cupak C., Fellinger M., Granberg F., Szabo P.S., Mutzke A., Nordlund K., Aumayr F. and González-Arrabal R., “Comparative study regarding the sputtering yield of nanocolumnar tungsten surfaces under Ar+ irradiation”, *Physical Review Materials*, **6**, 075402 (2022)

[112] Biersack J. and Eckstein W., “Sputtering studies with the Monte Carlo program TRIM. SP”, *Applied Physics A*, **34**, 73 (1984)

[113] Möller W., Eckstein W. and Biersack J.P., “Tridyn - Binary Collision Simulation of Atomic-Collisions and Dynamic Composition Changes in Solids”, *Computer Physics Communications*, **51**, 355 (1988)

[114] Arredondo R., Oberkofler M., Schwarz-Selinger T., von Toussaint U., Burwitz V., Mutzke A., Vassallo E. and Pedroni M., “Angle-dependent sputter yield measurements of keV D ions on W and Fe and comparison with SDTrimSP and SDTrimSP-3D”, *Nuclear Materials and Energy*, **18**, 72 (2019)

[115] Szabo P., Poppe A., Biber H., Mutzke A., Pichler J., Jäggi N., Galli A., Wurz P. and Aumayr F., “Deducing Lunar Regolith Porosity From Energetic Neutral Atom Emission”, *Geophysical Research Letters*, **49**, e2022GL101232 (2022)

[116] Lord H., “Hydrogen and helium ion implantation into olivine and enstatite: Retention coefficients, saturation concentrations, and temperature-release profiles”, *Journal of Geophysical Research*, **73**, 5271 (1968)

[117] Futagami T., Ozima M. and Nakamura Y., “Helium ion implantation into minerals”, *Earth and Planetary Science Letters*, **101**, 63 (1990)

[118] Hartle R., Curtis S. and Thomas G., “Mercury’s helium exosphere”, *Journal of Geophysical Research*, **80**, 3689 (1975)

[119] Anthony J.W., Bideaux R.A., Bladh K.W. and Nichols M.C., “Handbook of mineralogy, mineralogical society of America, Chantilly, VA 20151-1110, USA”, (2001)

[120] Eckstein W. and Preuss R., “New fit formulae for the sputtering yield”, *Journal of Nuclear Materials*, **320**, 209 (2003)

[121] Szabo P.S., Weichselbaum D., Biber H., Cupak C., Mutzke A., Wilhelm R. and Aumayr F., “Graphical user interface for SDTrimSP to simulate sputtering, ion implantation and the dynamic effects of ion irradiation”, *Nuclear Instruments and Methods in Physics Research Section B: Beam Interactions with Materials and Atoms*, **522**, 47 (2022)

[122] Yamamura Y., “Computer studies of reemission and depth profiles for helium on molybdenum”, *Nuclear Instruments and Methods in Physics Research Section B: Beam Interactions with Materials and Atoms*, **28**, 17 (1987)

[123] Mazey D., Eyre B., Evans J., Erents S. and McCracken G., “A transmission electron microscopy study of molybdenum irradiated with helium ions”, *Journal of Nuclear Materials*, **64**, 145 (1977)

[124] Sasajima N., Matsui T., Furuno S., Hojou K. and Otsu H., “Damage accumulation in Al2O3 during H2+ or He+ ion irradiation”, *Nuclear Instruments and Methods In Physics Research Section B: Beam Interactions With Materials and Atoms*, **148**, 745 (1999)

[125] Carrez P., Demyk K., Cordier P., Gengembre L., Grimblot J., D’HENDECOURT L., Jones A.P. and Leroux H., “Low-energy helium ion irradiation-induced amorphization and chemical changes in olivine: Insights for silicate dust evolution in the interstellar medium”, *Meteoritics & Planetary Science*, **37**, 1599 (2002)

[126] Vasavada A.R., Paige D.A. and Wood S.E., “Near-surface temperatures on Mercury and the Moon and the stability of polar ice deposits”, *Icarus*, **141**, 179 (1999)

[127] Curtis S. and Hartle R., “Mercury’s helium exosphere after Mariner 10’s third encounter”, *Journal of Geophysical Research: Space Physics*, **83**, 1551 (1978)

[128] Domingue D.L., Chapman C.R., Killen R.M., Zurbuchen T.H., Gilbert J.A., Sarantos M., Benna M., Slavin J.A., Schriver D. and Travnicek P.M., “Mercury’s weather-beaten surface: Understanding Mercury in the context of lunar and asteroidal space weathering studies”, *Space Science Reviews*, **181**, 121 (2014)

[129] Loeffler M., Dukes C. and Baragiola R., “Irradiation of olivine by 4 keV He+: Simulation of space weathering by the solar wind”, *Journal of Geophysical Research: Planets*, **114** (2009)

[130] Demyk K., Carrez P., Leroux H., Cordier P., Jones A., Borg J., Quirico E., Raynal P. and d’Hendecourt L., “Structural and chemical alteration of crystalline olivine under low energy He+ irradiation”, *Astronomy & Astrophysics*, **368**, L38 (2001)

[131] Bradley J., Dukes C., Baragiola R., McFadden L., Johnson R. and Brownlee D., “Radiation processing and the origins of interplanetary dust”, in *Lunar and Planetary Science Conference*, volume 27 (1996)

[132] Deer W.A., Howie R.A. and Zussman J., “Rock-forming minerals: single-chain silicates, Volume 2A”, Geological Society of London (1997)

[133] Wurz P., Rohner U., Whitby J.A., Kolb C., Lammer H., Dobnikar P. and Martín-Fernández J., “The lunar exosphere: The sputtering contribution”, *Icarus*, **191**, 486 (2007)

[134] Wehner G., Kenknight C. and Rosenberg D., “Sputtering rates under solar-wind bombardment”, *Planetary and Space Science*, **11**, 885 (1963)

[135] Carrier III W.D., Olhoeft G.R. and Mendell W., “Physical properties of the lunar surface”, *Lunar sourcebook*, 475–594 (1991)

[136] Cassidy T. and Johnson R., “Monte Carlo model of sputtering and other ejection processes within a regolith”, *Icarus*, **176**, 499 (2005)

[137] Rodriguez-Nieva J., Bringa E.M., Cassidy T., Johnson R., Caro A., Fama M., Loeffler M., Baragiola R. and Farkas D., “Sputtering from a porous material by penetrating ions”, *The Astrophysical Journal Letters*, **743**, L5 (2011)

List of Figures

Danksagung

In den folgenden Zeilen möchte ich mich bei den Menschen bedanken, die mich auf meinem Weg zu diesem Abschluss begleitet und unterstützt; beziehungsweise ihn überhaupt erst ermöglicht haben.

Beginnen möchte ich bei meinem baldigen Doktorvater, Prof. Friedrich Aumayr. Lieber Fritz, ohne dich wäre meine Dissertation so sicherlich nicht möglich gewesen. Nicht nur aufgrund deiner Betreuung, sondern auch weil du den nötigen Rahmen dafür geschaffen hast. Du hattest immer Verständnis dafür, wenn es mal etwas schwieriger war alles unter einen Hut zu bringen. Außerdem hattest du immer ein offenes Ohr für Probleme und hast dich dann gleich mit ihnen beschäftigt, obwohl du mit deinen vielen Verpflichtungen selbst kaum Zeit dafür hattest. Außerdem muss ich wiederholt deine Art die Gruppe zu leiten positiv hervorheben. Diese sorgt nicht nur für ein humorvolles Klima, sondern erlaubt einen Ausgleich zur eigentlichen Arbeit IN der Arbeit. Dadurch bin ich selbst in Zeiten die von Rückschlägen geprägt waren immer gerne auf die Uni gefahren. Danke für all die Erfahrungen die ich in deiner Obhut sammeln durfte und die schöne Zeit in deiner AG!

Weiters möchte ich mich bei den Mitgliedern der Arbeitsgruppe Atom und Plasmaphysik für die schöne gemeinsame Zeit bedanken und ein paar Worte an einige (teils ehemalige) Mitglieder im Speziellen richten:

Paul, du hast die Gruppe zwar schon deutlich vor mir verlassen, hast meine Zeit dort aber geprägt wie niemand sonst. Deine Hingabe und Entschlossenheit, wenn du mal eine Idee hattest, diese dann tatsächlich umzusetzen, hat mich immer inspiriert. Die Diskussionen mit dir haben mir große Freude bereitet – und umso mehr, wenn dann daraus ein fertiger Umbau, eine neue Messung oder gar eine Publikation gekeimt ist. Und die beste Zeit für solche Gespräche war irgendwie immer fünf Minuten bevor ich gehen sollte; gedauert haben sie dann naturgemäß etwas länger :)

Schmu, du warst einen noch kürzeren Teil meiner Dissertation in der AG, dein Geist ist dort aber nach wie vor in Form kleiner Streiche anwesend. Abseits davon kann ich mich noch sehr gut erinnern, wie wir uns oft fachlich nicht immer einig waren, aber beide einander zugehört haben und dann meistens gemeinsam eine Lösung gefunden haben, die sicherlich deutlich besser war, als alleine sein Süppchen zu kochen. Und das rumnerdeln mit dir hat immer besondere Freude bereitet, auch wenn dein Laptop neben uns manchmal fast abgehoben wäre.

Janine, wir haben zwar nicht direkt gemeinsam gearbeitet, aber dein Witz und deine Fähigkeit selbst schwierige Situationen mit Humor zu nehmen haben meine Zeit in der AG sehr positiv geprägt.

Georg, du warst zwar physisch weniger präsent, hast das ganze aber an den Tagen in denen du da warst mehr als kompensiert. Auch wenn nicht alles bei allen hängen bleibt, („Was? Eine Knockbox mit Vakuum?“, „Veratasium? Nein den Typ kenn ich nicht“) bist nicht nur du, sondern sind auch deine Beiträge ein riesiger Gewinn für die Gruppe.

Und wer würde den Plasmaphysik-Teil der Gruppe besser ergänzen als LidiJA! Dein Humor und deine angenehm entspannte Art haben immer für gute Laune gesorgt. Ich könnte mir niemand besseren als best lunch buddy vorstellen um für die ganze Mittagspause über die Architektur spannender Gebäude diskutieren zu dürfen. Und wenn du das nächste mal wegen einem Lockdown nicht auf ein Konzert kannst, werde ich das auch ernst nehmen, bestimmt!

Christian, das grübeln an Problemstellungen im Labor oder an der zugrundeliegenden Physik war immer inspirierend und es war toll, mit dir gemeinsam an Projekten arbeiten zu können. Und auch abseits vom Arbeitsalltag hatte ich immer große Freude beim gemeinsamen Philosophieren im Büro oder beim abendlichen Basteln. Apropos Basteln – Anna: Du warst immer mit Rat und Tat zur Stelle, wenn ich mal unsicher war oder nicht weiter wusste. Danke, dass ich jederzeit mit meinen Problemen zu dir kommen konnte. Auch deine Rückmeldung beim Erstellen von Grafiken oder Texten hat immer zu einem deutlich besseren Ergebnis geführt und hoffentlich auch meinen Blick für Details geschärft. Selbst in der Gruppe würde wohl vieles nicht so gut laufen wie es zur Zeit der Fall ist, und sie kann sich glücklich schätzen, dich langfristig als Unterstützung gewonnen zu haben. Auch dir Daniel möchte ich meinen Dank aussprechen. Unsere gemeinsame Zeit zu dritt im Büro werde ich nie vergessen. Sei es beim Nachbereiten von TfM oder beim Eis holen, wir hatten viel Spaß zusammen :)

Johannes, du warst seit du zur AG gestoßen bist ein wertvoller Begleiter und ich hab es sehr zu schätzen gewusst, dass wir den positiven Zugang zum Arbeiten geteilt haben. Am schönsten war das meist herzliche Lachen über die Steine, die uns scheinbar plötzlich im Weg gelegen sind. Ich bin mir sicher, bei dir sind sowohl das Experiment als auch die Labor IT in ausgezeichneten Händen.

Posterkönigin Martina, du warst und bist immer für einen Schmäh zu haben. Du wirst gemeinsam mit Johannes sicher für gute Stimmung im Sputter- Eck des Labors sorgen und sicherlich den ein oder anderen Streich parat haben.

Gabriel, du warst mir vor allem am AFM eine große Hilfe und ohne deine Expertise wären die Aufnahmen wie sie in der Arbeit sind vermutlich nicht zu Stande gekommen. Matthias, auch wenn wir anfänglich unsere Differenzen hatten, warst du stets hilfsbereit und hattest immer eine helfende Hand parat, was ich sehr zu schätzen gewusst habe.

Richard, zu dir konnte ich immer mit Problemen aus dem Leben eines experimentellen Physikers kommen und dabei viel von dir lernen. Auch das gemeinsame

Lachen über die Hindernisse und Probleme im Alltag hat mich viele Dinge leichter sehen und nehmen lassen!

Martin, mit dir hat man immer lustige und spannende Diskussionen führen – und Pumpen reparieren ;-) – können. Deine Hilfe bei Bestellungen und organisatorischen Angelegenheiten hat mir sehr viel Zeit und Mühe erspart – danke dafür!

Ille, du hast immer einen Blick über den Tellerrand hinaus ermöglicht und spannende Geschichten parat gehabt. Danke, dass du meine Zeit in der AG bereichert hast!

Als letztes ehemaliges Mitglied der AG möchte ich meinen Dank noch an Rimpei richten. Ich habe während der Zeit im Labor oftmals an dich und unsere gemeinsamen Versuche – inklusive viel Scheitern und lachen – denken müssen. Mein Einstieg in die Gruppe an deiner Seite wird mir stets in Erinnerung bleiben.

Und auch außerhalb der AG gibt es einige Menschen, denen ich danken möchte. Allen voran der treibenden Kraft hinter unseren Meetings mit der Universität in Bern, Noah. Wir haben immer die Zeit für ausführliche, gegenseitige Rückmeldung gefunden, was mir sicherlich in beide Richtungen gut getan hat. Auf unseren gemeinsamen Konferenzen konnten wir sicher viel voneinander lernen und miteinander lachen. Natürlich möchte ich auch André und Peter aus Bern danken. Ihr habt oft einen etwas anderen Anblick ermöglicht und unsere Diskussionen haben uns sicher gemeinsam weiter gebracht.

Einen ganz wichtigen Beitrag zu meiner Arbeit hat auch Andreas vom IPP in Greifswald. Ohne deine Hilfe beim Verständnis sowie die rasche Implementierung neuer Möglichkeiten in den Code wären viele Teile dieser Arbeit nicht möglich gewesen. Mit dir über Lösungsansätze nachdenken hatte oftmals etwas von einem Rätsel, das mich meist nicht los gelassen hat, bis du auf einmal mit einer Idee und der passenden neuen Version gekommen bist.

Weiters möchte ich mich noch bei Herbert und Rainer aus unserer Werkstätte bedanken. Nicht nur, dass man seine Teile immer schnell bekommen hat – noch wichtiger waren zum einen eure Ratschläge um Designs zu verbessern und zum anderen eure Bereitschaft selbst an Freitag Nachmittagen doch noch schnell ein Teil zu machen, was plötzlich dringend vor dem Wochenende geändert werden musste.

Ganz besonderer Dank gilt natürlich meiner Familie. Auf die Unterstützung meiner Eltern konnte ich stets zählen und allein zu wissen, dass ihr im Zweifelsfall immer für mich da gewesen wärt war unersetzlich. Vielen Dank! Gleiches gilt für meine Schwester Romana, die mich während meiner Wien Aufenthalte in den letzten Monaten bei sich aufgenommen hat. Anna, es war nicht immer ganz leicht, eine gute Balance zwischen dem Fortschritt meiner Dissertation und Zeit zu Hause zu finden, aber ich danke dir von Herzen für dein Verständnis, welches du oft aufbringen musstest und die Unterstützung die ich stets von dir bekommen habe. Vor allem könnte ich mir keinen schöneren Ausgleich vorstellen, als unsere Zeit zu viert. Ferdinand und Josefa, ihr habt mein Leben verändert wie sonst niemand und ihr seid mir stets eine zusätzliche Stütze und Motivation in meinem Tun.